

# Dynamical Mean-Field Theory for Manganites

YI-FENG YANG

MAX-PLANCK-INSTITUT FÜR FESTKÖRPERFORSCHUNG  
STUTT GART, 2007



# Dynamical Mean-Field Theory for Manganites

Von der Fakultät Mathematik und Physik der Universität Stuttgart  
zur Erlangung der Würde eines Doktors der Naturwissenschaften  
(Dr. rer. nat.) genehmigte Abhandlung

vorgelegt von

YI-FENG YANG

aus Henan (China)

Hauptberichter:	Priv.-Doz. Dr. K. Held
Mitberichter:	Prof. Dr. A. Muramatsu
Tag der Einreichung:	15.11.2006
Tag der mündlichen Prüfung:	15.02.2007

MAX-PLANCK-INSTITUT FÜR FESTKÖRPERFORSCHUNG  
STUTT GART, 2007



For my parents



## Abstract

In this thesis, we perform dynamical mean-field theory (DMFT) calculations for perovskite manganites such as  $\text{La}_{1-x}\text{Sr}_x\text{(Ca)}_x\text{MnO}_3$ . These materials have been intensively investigated due to an extraordinary property: colossal magnetoresistance (CMR). The complicated phase diagrams of perovskite manganites reflect the internal complexity resulting from the interplay between charge, spin, orbital and lattice degrees of freedom. In doped manganites, optical experiments show unusual dynamic properties such as a pseudo-gap behavior. Whereas the low temperature ferromagnetic metallic phase has been generally attributed to the "double exchange" mechanism, the high temperature paramagnetic insulating phase is not yet fully understood. Even in the parent compound  $\text{LaMnO}_3$ , there has been a long debate whether the Coulomb interaction or the Jahn-Teller coupling plays a more important role.

Theoretically, DMFT provides arguably the most reliable tool to treat these local correlations. The basic idea of DMFT is to map a lattice problem onto a self-consistent impurity problem in the limit of infinite dimensions. In finite dimensions, DMFT has been proved to be a good approximation as long as spatial fluctuations are small. The impurity problem can be solved by using the quantum Monte Carlo technique, as well as many other different approaches.

The thesis includes two main parts. First, in combination with band structure calculations, we use DMFT to study the pressure-induced metal-insulator transition in  $\text{LaMnO}_3$ . This allows us to conclude the indispensable role of both the Coulomb interaction and the Jahn-Teller coupling, in contrast to previous claims. A realistic microscopic model is then proposed to incorporate both interactions and the Hund's rule coupling. For doped manganites, the model leads to the lattice polaron picture and gives rise to the midgap states observed in experiments. The combination of the polaron states and the midgap states explains the pseudo-gap behavior observed in doped manganites. The numerical results are in good agreement with the optical data. The metal-insulator transition and the CMR effect observed in doped manganites are understood as a result of the magnetic ordering below  $T_c$ . The work, however, still shows some quantitative discrepancies with experiments. These are attributed to contributions such as the the O  $2p$  and Mn  $3d$  hybridization which are not included in the low-energy effective model used for manganites.

# Contents

<b>1</b>	<b>Introduction</b>	<b>9</b>
<b>2</b>	<b>Model</b>	<b>15</b>
2.1	Double exchange . . . . .	15
2.2	Jahn-Teller coupling . . . . .	19
2.3	Coulomb interaction . . . . .	24
2.4	Realistic microscopic model . . . . .	25
<b>3</b>	<b>Dynamical mean-field theory</b>	<b>33</b>
3.1	Dynamical mean-field theory . . . . .	33
3.1.1	Holstein model . . . . .	36
3.1.2	Hubbard model . . . . .	41
3.1.3	Realistic microscopic model . . . . .	43
3.2	Maximum entropy method . . . . .	45
3.3	Static spin susceptibility . . . . .	47
3.4	Optical conductivity . . . . .	50
3.5	LDA+DMFT approach . . . . .	54
<b>4</b>	<b>Pressure-induced metal-insulator transition</b>	<b>59</b>
4.1	Experiment . . . . .	59
4.2	LDA+DMFT investigations . . . . .	63
4.2.1	Band structures . . . . .	64
4.2.2	Electronic properties . . . . .	66
4.3	DMFT model calculations . . . . .	70
4.3.1	Lattice distortion . . . . .	71
4.3.2	Insulating ground state . . . . .	74
4.3.3	Structural transition . . . . .	76
<b>5</b>	<b>Doped manganites</b>	<b>81</b>
5.1	Experiments . . . . .	82
5.2	DMFT model calculations . . . . .	86
5.2.1	Lattice distortion . . . . .	86
5.2.2	Spectral density . . . . .	91
5.2.3	Optical conductivity . . . . .	93



5.2.4 Curie temperature . . . . .	99
5.3 Estimates of parameters . . . . .	101
<b>6 Conclusions and outlook</b>	<b>107</b>
<b>Bibliography</b>	<b>109</b>
<b>Publications</b>	<b>126</b>
<b>Acknowledgments</b>	<b>127</b>
<b>Deutsche Zusammenfassung</b>	<b>128</b>
<b>Curriculum Vitae</b>	<b>134</b>



# 1 Introduction

Perovskite manganites have attracted intensive interest during the last decades due to their extraordinary property of colossal magnetoresistance (CMR) [Millis 1998, Dagotto et al. 2001, Salamon & Jaime 2001]. The general chemical formula of these materials is  $T_{1-x}D_x\text{MnO}_3$ , where T is a trivalent rare earth ion (T = La, Pr, Nd, ...) and D is a divalent alkali ion (D = Ca, Sr, ...). Fig. 1.1 shows the typical perovskite structure with six oxygen atoms sitting around each manganese atom forming an octahedron. Theoretically, the system is often modelled by a cubic lattice of the manganese 3d orbitals, since all other orbitals are far away from the Fermi energy. The fivefold 3d orbitals are split by the crystal field into two higher energy  $e_g$  orbitals ( $d_{3z^2-r^2}$  and  $d_{x^2-y^2}$ ) and three lower energy  $t_{2g}$  orbitals ( $d_{xy}$ ,  $d_{yz}$ , and  $d_{zx}$ ). The half-occupied  $t_{2g}$  orbitals are localized and have a total spin  $|\mathbf{S}| = 3/2$  due to Hund's rules. The two  $e_g$  orbitals are partially occupied with  $1 - x$  electrons per manganese ion.

The perovskite manganites have a very complicated phase diagram (see Fig. 1.2 for

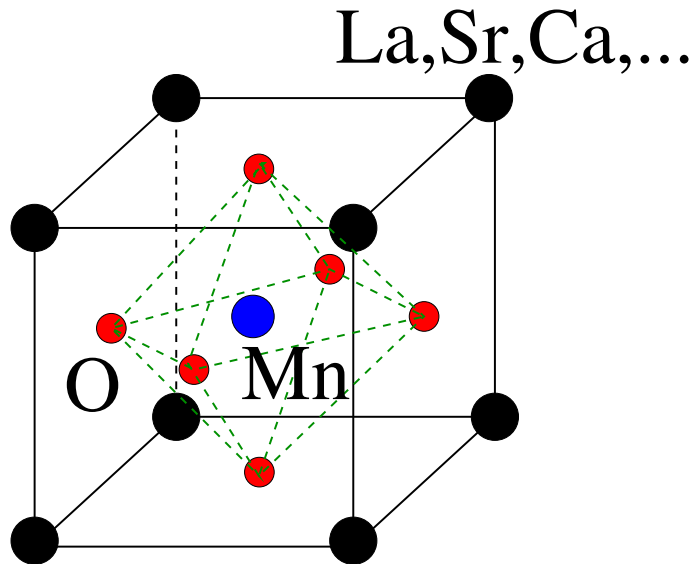


Figure 1.1: Sketch of the cubic perovskite unit cell for manganites. The position of the La atoms can be shifted and the  $\text{MnO}_6$  octahedron can be deformed by the  $\text{GdFeO}_3$  and Jahn-Teller distortions.

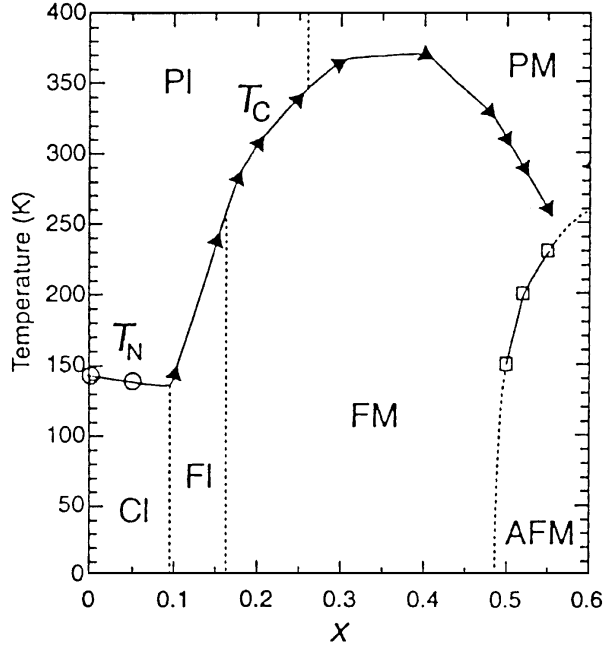


Figure 1.2: Phase diagram of  $\text{La}_{1-x}\text{Sr}_x\text{MnO}_3$  as a function of temperature  $T$  and doping  $x$ . PI — paramagnetic insulator; PM — paramagnetic metal; CI — spin canted insulator; FI — ferromagnetic insulator; FM — ferromagnetic metal; AFM — antiferromagnetic metal;  $T_C$  — Curie temperature;  $T_N$  — Néel temperature. Figure taken from Ref. [Dagotto et al. 2001].

$\text{La}_{1-x}\text{Sr}_x\text{MnO}_3$ ). Jonker and van Santen first reported the existence of ferromagnetism in mixed crystals of  $\text{LaMnO}_3\text{-CaMnO}_3$ ,  $\text{LaMnO}_3\text{-SrMnO}_3$ , and  $\text{LaMnO}_3\text{-BaMnO}_3$  [Jonker & Santen 1950, Santen & Jonker 1950]. Antiferromagnetic and ferromagnetic phases were later characterized for  $\text{La}_{1-x}\text{Ca}_x\text{MnO}_3$ , together with a nontrivial arrangement of charge at particular hole densities in the antiferromagnetic phase [Wollan & Koehler 1955].

The "colossal" magnetoresistance (CMR) effect, which triggered the present interest in manganites, can be described by the magnetoresistance ratios  $\eta = \Delta R/R(H) = (R(0) - R(H))/R(H)$  or  $\eta' = \Delta R/R(0) = (R(0) - R(H))/R(0)$ , where  $R(0)$  and  $R(H)$  are the resistance without and with a magnetic field  $H$ , respectively. The correlation between magnetism and conductivity was known since the work of Jonker and van Santen [Jonker & Santen 1950, Santen & Jonker 1950]. Its implication was, however, only explored in 1993, when a large magnetoresistance ( $\eta' = 50\%$ ) was observed in thin films under magnetic field [Chahara et al. 1993, von Helmolt et al. 1993]. In a  $\text{La}_{0.67}\text{Ca}_{0.33}\text{MnO}_x$  film,  $\eta$  was found to be as large as 127,000%, for which the term colossal magnetoresistance was first coined [Jin et al. 1994]. A magnetoresis-

---

tance ratio as high as  $\eta = 10^6\%$  was also reported in thin films of  $\text{Nd}_{0.7}\text{Sr}_{0.3}\text{MnO}_\delta$  [Xiong et al. 1995]. Unlike giant magnetoresistance found in the ferromagnetic/non-magnetic multilayers, CMR is a bulk property which originates from the magnetic ordering in the material.

Soon after CMR was discovered, various phase diagrams as a function of temperature and magnetic field or doping concentration were established [Tokura et al. 1994, Urushibara et al. 1995, Kuwahara et al. 1995, Tomioka et al. 1995a, Tomioka et al. 1995b, Tomioka et al. 1996, Tomioka et al. 1997, Moritomo et al. 1997, Mukhin et al. 1998]. Some of these phase diagrams can be found in the review articles [Tokura et al. 1996, Tokura & Tomioka 1999, Salamon & Jaime 2001, Dagotto et al. 2001]. The pressure-induced insulator-to-metal transition was also studied for the parent compound  $\text{LaMnO}_3$  [Loa et al. 2001]. A charge/orbital-ordered phase has been observed in a large number of perovskite ( $\text{T}_{1-x}\text{D}_x\text{MnO}_3$ ) and layered ( $\text{T}_{1-x}\text{D}_{1+x}\text{MnO}_4$ ) manganites and its dependence on the effective bandwidth and the quenched disorder has also been analyzed [Tomioka & Tokura 2004, Mathieu et al. 2006]. Moreover, optical experiments show unusual dynamic properties in the paramagnetic insulating phase of doped manganites. The latter reflect in a spectral function  $A(\omega)$  with a very low spectral weight at the Fermi level  $E_F$  irrespectively of  $x$ , as indicated by photoemission and X-ray absorption experiments [Bocquet et al. 1992, Chainani et al. 1993, Saitoh et al. 1997, Park et al. 1996]. Similarly the optical conductivity  $\sigma(\omega)$  shows a very low spectral weight up to an energy scale of  $\sim 1$  eV [Okimoto et al. 1995, Quijada et al. 1998, Jung et al. 1998, Takenaka et al. 1999]. Also the ferromagnetic metallic phase is an atypical (bad) metal [Okimoto et al. 1995].

A physical understanding of these properties is difficult. The complicated phase diagram reflects the internal complexity resulting from the interplay between charge, spin, orbital and lattice degrees of freedom [Millis 1998, Tokura 2003]. The current theoretical investigations focus on the orbital-ordered phase in the parent compound  $\text{LaMnO}_3$  [Yin et al. 2006], the metal-insulator transition in doped manganites [Dagotto et al. 2001], as well as the charge/orbital-ordered phase in the half-doped manganites [Popović & Satpathy 2002].

The earliest theory of ferromagnetism in doped manganites is the so-called "double exchange" (DE) mechanism [Zener 1951a, Zener 1951b]. Based on this mechanism, also the antiferromagnetic phase at  $x=0$  and the charge-ordered phase at  $x=0.5$  found in manganites were predicted [Goodenough 1955]. A spin-canted state was suggested later [de Gennes 1960]. This mechanism finally led to the well-known Kondo lattice model [Kubo & Ohata 1972], in which the localized  $t_{2g}$  electrons are described as classical spins of length  $|\mathbf{S}| = 3/2$  and coupled to the itinerant  $e_g$  electrons according to Hund's rules. The requirement to optimize the kinetic energy

of the itinerant electrons favors a spin polarized ground state.

The double exchange mechanism explains successfully the correlation between magnetism and conductivity in doped manganites, but disagrees with experiments in many aspects. The importance of the Jahn-Teller phonons was then proposed [Millis et al. 1995] and their effect was studied intensively together with the Hund's coupling for  $e_g$  electrons [Röder et al. 1996, Millis et al. 1996a, Millis et al. 1996b, Millis et al. 1996c]. Although the new model fails to produce a large magnetoresistance at finite doping, it can give rise to an insulating-like behavior for large electron-phonon coupling when electrons are trapped as lattice polarons [Millis et al. 1996a].

To explain the CMR and the paramagnetic insulating-like phase, many other mechanisms were then proposed, in particular, the localization of charge carriers through orbital polarons [Kilian & Khaliullin 1998, Horsch et al. 1999], Anderson localization arising from disordered  $t_{2g}$ -spins [Varma 1996], and phase separation into nano-domains showing percolation effects [Yunoki et al. 1998, Mayr et al. 2001]. Among them, the on-site Coulomb interaction, which is well-known to be responsible for the Mott-Hubbard insulator at integer fillings, was also studied in an extended Kondo lattice model [Held & Vollhardt 2000]. It is believed to enhance the electron localization.

Despite all these efforts, hitherto no quantitative, microscopic calculation satisfactorily explains all the known experimental facts, especially the paramagnetic insulating phase which exists in a wide range of dopings  $x$ . Even in the parent compound  $\text{LaMnO}_3$ , it has been an issue of long debate whether the Jahn-Teller distortion or the Coulomb repulsion is responsible for the insulating ground state at ambient conditions. Theories give rather different answers [Banach & Temmerman 2004, Zenia et al. 2005, Yamasaki et al. 2006], while the high pressure experiment seems to indicate the importance of the Coulomb interaction [Loa et al. 2001].

A huge numerical effort is also an obstacle towards a satisfactory understanding of the physics of manganites. Both the (local) electron-electron and electron-phonon interactions, as well as the Hund's coupling between the itinerant  $e_g$  electrons and the localized  $t_{2g}$  spins, have to be taken into account. In this respect, the dynamical mean-field theory (DMFT) with the quantum Monte Carlo (QMC) solver provides presently one of the most reliable tools to treat the local electronic correlations [Georges et al. 1996]. Density functional theory within the local density approximation (LDA) [Hohenberg & Kohn 1964, Kohn & Sham 1964, Kohn & Sham 1965, Sham & Kohn 1966, Jones & Gunnarsson 1989] may also be important for realistic investigations of the electronic structures of manganites [Anisimov et al. 1997, Lichtenstein & Katsnelson 1998, Katsnelson & Lichtenstein 2000, Held 2003, Held 2005].

In this thesis, we first use the LDA+DMFT approach to investigate the pressure-

---

induced insulator-to-metal transition in  $\text{LaMnO}_3$  and clarify the role of the Coulomb repulsion and the Jahn-Teller coupling in manganites. A realistic microscopic model is then proposed and studied for doped manganites by using the DMFT (QMC) method. Our main conclusions are

- The Coulomb repulsion and the Jahn-Teller coupling are both indispensable in understanding the electronic properties of  $\text{LaMnO}_3$ . Neither of them alone can make the system an insulator at ambient conditions. It is only with the Coulomb repulsion that the splitting of the  $e_g$  orbitals created by the Jahn-Teller distortion is strongly enhanced, giving rise to the insulating behavior of  $\text{LaMnO}_3$ . Moreover, the pressure-induced insulator-to-metal transition is not of Mott-Hubbard type, but results from the overlap of the split  $e_g$  orbitals due to the reduced crystal field splitting and the increased effective bandwidth at high pressures. The lattice distortion is reduced but not completely suppressed at the transition point, in contrast to previous claims.
- The high temperature paramagnetic insulating phase and the low temperature ferromagnetic metallic phase in doped manganites can be obtained from a realistic microscopic model including both the Coulomb repulsion and the Jahn-Teller coupling, as well as the Hund's coupling between the itinerant  $e_g$  electrons and the localized  $t_{2g}$  spins. For large Jahn-Teller coupling, the strongly correlated  $e_g$  electrons are trapped as lattice polarons. The model also gives rise to the midgap states observed in experiments. The combination of the polaron states and the midgap states results in the pseudo-gap behavior in doped manganites. The pseudo-gap is found to be enhanced by the strong Coulomb repulsion.

Our work clarifies the role of the Coulomb interaction and the Jahn-Teller coupling in both undoped and doped manganites. The two interactions are found to mutually support each other. The direct comparison between numerical calculations and experimental observations also shows some discrepancies which we attribute to contributions not included in the low-energy effective model generally used for manganites. Further investigations are still required for a better understanding of manganites.

The thesis is organized as follows:

- In Chapter 2 several models are discussed concerning the effects of the double exchange, the Jahn-Teller coupling and the Coulomb interaction in manganites. Their combination leads to the realistic microscopic model used in our

work. We then explain how the values of some of the important parameters can be estimated from experiments.

- In Chapter 3 we introduce the DMFT (QMC) technique and show by examples how it can be implemented in practice for coupled boson-fermion systems. The formula for the spin susceptibility and the optical conductivity will be derived in the limit of infinite dimensions. We also explain briefly the idea of the LDA and LDA+DMFT approaches.
- In Chapter 4 we describe in detail the high pressure experiment and present our LDA+DMFT results for the pressure-induced insulator-to-metal transition in the parent compound  $\text{LaMnO}_3$ . We show the origin of the insulating ground state and the nature of the pressure-induced transition. DMFT calculations for the realistic microscopic model are also performed to investigate the the electronic properties and the structural (orbital-ordered) transition from dynamic to static Jahn-Teller distortion in  $\text{LaMnO}_3$ . Parts of this chapter are published in

A. Yamasaki, M. Feldbacher, Y.-F. Yang, O. K. Andersen, and K. Held, *Pressure-induced metal-insulator transition in  $\text{LaMnO}_3$  is not of Mott-Hubbard type*, Phys. Rev. Lett. **96**, 166401 (2006).

- In Chapter 5 DMFT calculations for the realistic microscopic model are carried out for doped manganites. After a detailed analysis of various optical experiments, numerical results are presented and found to be in good agreement. The basic physics behind manganites is discussed. We then introduce the breathing phonon into the model and parameters such as the Coulomb interaction and the Jahn-Teller coupling are estimated by comparing our numerical results with optical data in both undoped and doped manganites. Parts of this chapter are contained in the preprint

Y.-F. Yang and K. Held, *Localization of strongly correlated electrons as Jahn-Teller polarons in manganites*, cond-mat/0603553.

- We conclude in Chapter 6 with a summary and an outlook of problems for further investigations.



## 2 Model

In this chapter, we introduce several models to study the effects of the double exchange, the Jahn-Teller coupling and the local Coulomb interaction in manganites. As we will see, the double exchange mechanism provides the basis for our understanding of ferromagnetism in doped manganites, while the Jahn-Teller coupling leads to the electron localization which may explain the pseudo-gap behavior observed in doped manganites. Also, the local Coulomb interaction plays an important role in determining the nature of the insulating ground state and the pressure-induced metal-insulator transition in  $\text{LaMnO}_3$ . It is therefore necessary to combine all of them together in order to achieve a better understanding of the physics of manganites. A realistic microscopic model is then proposed and some of the parameters are estimated from experiments.

### 2.1 Double exchange

In manganites, the Mn  $t_{2g}$  spins are strongly coupled to the spin of the itinerant  $e_g$  electrons. According to the so-called "double exchange" mechanism [Zener 1951a, Zener 1951b], this coupling leads to an effective indirect ferromagnetic interaction between adjacent  $t_{2g}$  spins. This indirect ferromagnetic interaction competes with the antiferromagnetic superexchange interaction between the  $t_{2g}$  spins, giving rise to the antiferromagnetic phase at  $x = 1$  and the low temperature ferromagnetic phase observed in doped manganites.

The double exchange mechanism can be explained by considering a system of two Mn ions separated by an  $\text{O}^{2-}$  ion. For a single  $e_g$  electron, there exist two possible charge states:

$$\begin{aligned}\psi_1 & : \quad \text{Mn}^{3+} \text{O}^{2-} \text{Mn}^{4+}, \\ \psi_2 & : \quad \text{Mn}^{4+} \text{O}^{2-} \text{Mn}^{3+},\end{aligned}$$

which are degenerate in energy. They are, however, not eigenstates of the system since the  $e_g$  electron can transfer from the  $\text{Mn}^{3+}$  ion to the adjacent  $\text{Mn}^{4+}$  ion through the intermediate  $\text{O}^{2-}$  ion, as is visualized in Fig. 2.1. This transfer process is called a "double exchange" [Zener 1951b]. The "double exchange" process introduces an effective hopping of the  $e_g$  electrons between the nearest-neighbor Mn

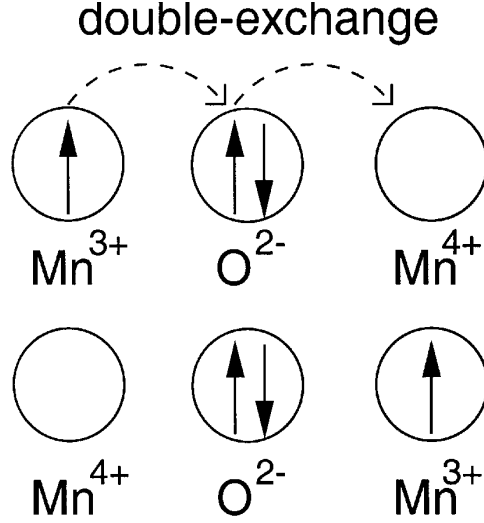


Figure 2.1: Double exchange process with one electron hopping from the intermediate  $\text{O}^{2-}$  ion to the right  $\text{Mn}^{4+}$  ion and simultaneously one electron from the left  $\text{Mn}^{3+}$  ion to the  $\text{O}^{2-}$  ion. Figure taken from Ref. [Dagotto et al. 2001].

ions, so that the ground state is a combination of the two charge states and the energy gain is approximately proportional to the effective hopping. Note that the manganese  $t_{2g}$  spins are usually treated as classical spins of length  $|\mathbf{S}| = 3/2$ . This allows us to introduce a tilting angle  $0 \leq \theta \leq \pi$  between adjacent spins. The effective hopping of the  $e_g$  conduction electrons is then renormalized by a factor of  $\cos(\theta/2)$  [Anderson & Hasegawa 1955]. Obviously, the two  $t_{2g}$  spins should point to the same direction in order to have a largest effective hopping and the ground state is a spin polarized state. The above arguments can be extended to a lattice model, where the requirement to optimize the kinetic energy favors the ferromagnetic phase. In doped manganites, this double exchange mechanism, together with the Hund's rule coupling, is generally believed to be responsible for the low temperature ferromagnetic phase [Jonker & Santen 1950, Santen & Jonker 1950]. Moreover, spin-canted states with  $0 < \theta < \pi$  were also predicted in some antiferromagnetic lattices based on similar arguments [de Gennes 1960].

In reality, the  $\text{O}^{2-}$  ions are often not considered and the system is modeled by a cubic lattice of manganese ions with the nearest neighbor hopping  $t_{\mu\nu}^{(ij)}$  of the  $e_g$  electrons and the local Hund's coupling between the  $e_g$  and  $t_{2g}$  spins. This is the well-known Kondo lattice model [Kubo & Ohata 1972]:

$$H_{KLM} = - \sum_{\langle ij \rangle; \mu\nu\sigma} t_{\mu\nu}^{(ij)} (c_{i\mu\sigma}^\dagger c_{j\nu\sigma} + c_{j\nu\sigma}^\dagger c_{i\mu\sigma}) - 2J \sum_{i;\mu} \mathbf{s}_{i\mu} \cdot \mathbf{S}_i, \quad (2.1)$$

where  $\{c_{i\mu\sigma}^\dagger, c_{i\mu\sigma}\}$  are the fermionic creation and annihilation operators for electrons at site  $i$  within  $e_g$ -orbital  $\mu$  with spin  $\sigma$  and  $\mathbf{s}_{i\mu}$  is the corresponding spin operator:

$$\mathbf{s}_{i\mu} = \sum_{\sigma_1\sigma_2} c_{i\mu\sigma_1}^\dagger \frac{\boldsymbol{\tau}_{\sigma_1\sigma_2}}{2} c_{i\mu\sigma_2}. \quad (2.2)$$

The Pauli matrices  $\boldsymbol{\tau}$  are defined as

$$\tau^x = \begin{pmatrix} 0 & 1 \\ 1 & 0 \end{pmatrix}, \quad \tau^y = \begin{pmatrix} 0 & -i \\ i & 0 \end{pmatrix}, \quad \tau^z = \begin{pmatrix} 1 & 0 \\ 0 & -1 \end{pmatrix}.$$

In the Hamiltonian (2.1), we neglect the antiferromagnetic superexchange between adjacent  $t_{2g}$  spins which becomes important close to  $x = 1$ . The local  $t_{2g}$  spins  $\mathbf{S}_i$  are assumed to be classical. This assumption is reasonable since  $|\mathbf{S}_i| = 3/2$  is large.

The Hund's coupling  $J$  plays a crucial role for the ferromagnetism in doped manganites. If  $J = 0$ , the spin susceptibility of the free  $e_g$  electrons and the isolated  $t_{2g}$  spins can be calculated exactly and there is no magnetic transition.

If  $J$  is much smaller than the bandwidth  $W$  of the  $e_g$  orbitals, it can be treated as a perturbation and gives rise to the Ruderman-Kittel-Kasuya-Yosida (RKKY) interaction between the  $t_{2g}$  spins.

If  $J \gg W$ , the electrons are strongly correlated. The model can be solved by the dynamical mean-field theory [Furukawa 1994, Millis et al. 1995, Furukawa 1998] or the many-body coherent potential approximation (CPA) [Edwards et al. 1999, Edwards 2002]. The two methods agree in the limit of  $|\mathbf{S}| \rightarrow \infty$  and  $J \rightarrow \infty$  [Green & Edwards 1999].

As an example, Fig. 2.2 shows the Curie temperature  $T_c$  of the one-band Kondo lattice model versus the average occupation number  $n = 1 - x$  for various  $|\mathbf{S}|$ , calculated with  $J = \infty$  using the elliptic bare density of states [Green & Edwards 1999]. The results were obtained by the many-body coherent potential approximation [Green & Edwards 1999]. The behavior of the Curie temperature is nonmonotonic with respect to the occupation number and has a maximum at intermediate  $n$  in agreement with experiments (see Fig. 1.2). For band occupations  $n = 0$  and  $n = 1$ , the spin susceptibility exhibits the correct Curie law and ferromagnetism is completely suppressed since in both cases the number of the itinerant carriers (electron at  $n = 0$  and hole at  $n = 1$ ) is zero. For the two-band Kondo lattice model (2.1), the Curie temperature has a maximum at  $n = 1$  ( $x = 0$ ) [Held & Vollhardt 2000], in contradiction with the experimental fact shown in Fig. 1.2.

For perovskite manganites with a hypothetical cubic structure, the bandwidth is about 3.6 eV [Yamasaki et al. 2006] so that the Curie temperatures are much larger than the experimental values. Moreover, the resistivity was also calculated and

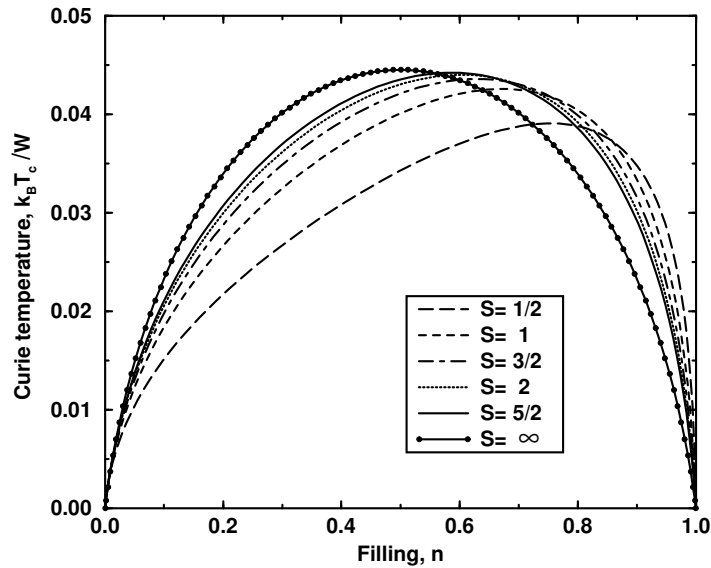


Figure 2.2: The Curie temperature  $T_c/W$  of the one-band Kondo lattice model versus the average occupation number  $n$  for various  $t_{2g}$  spins, calculated with  $J = \infty$  using the elliptic bare density of states. Note in this figure  $W$  denotes the half bandwidth. The results were obtained by the many-body coherent potential approximation. Figure taken from Ref. [Green & Edwards 1999].

found to be much smaller than observed [Edwards 2002], indicating that more scattering mechanisms are necessary and the spin disorder alone cannot account for the various properties of doped manganites. In Ref. [Millis et al. 1995], the importance of the Jahn-Teller effect in manganites was proposed to account for the experimental results.

We should note that a Monte Carlo study of a one-band Kondo lattice model led to a scenario of the phase separation between hole undoped antiferromagnetic and hole-rich ferromagnetic regions at small dopings [Yunoki et al. 1998]. The Curie temperature was obtained with a magnitude in agreement with experimental values. Based on this electronic phase separation scenario, a percolative mechanism was proposed to describe the resistivity of manganites [Mayr et al. 2001], which seems to explain the metal-insulator transition and the CMR effect in doped manganites. However, it is clear that the double exchange mechanism alone cannot explain (even qualitatively) many other experimental facts such as the pressure-induced insulator-to-metal transition in  $\text{LaMnO}_3$  (see chapter 4) and the unusual optical spectra observed in doped manganites (see chapter 5). All these indicate the importance of the Jahn-Teller coupling to the  $e_g$  electrons.

## 2.2 Jahn-Teller coupling

In perovskite manganites, the vibration of the La ions against the  $\text{MnO}_6$  octahedra and that of the oxygen ions give rise to the static and dynamic distortion of the lattice. These vibrational modes couple to the Mn  $e_g$  electrons and have strong effects on the electronic properties of the materials. Fig. 2.3 sketches some of these

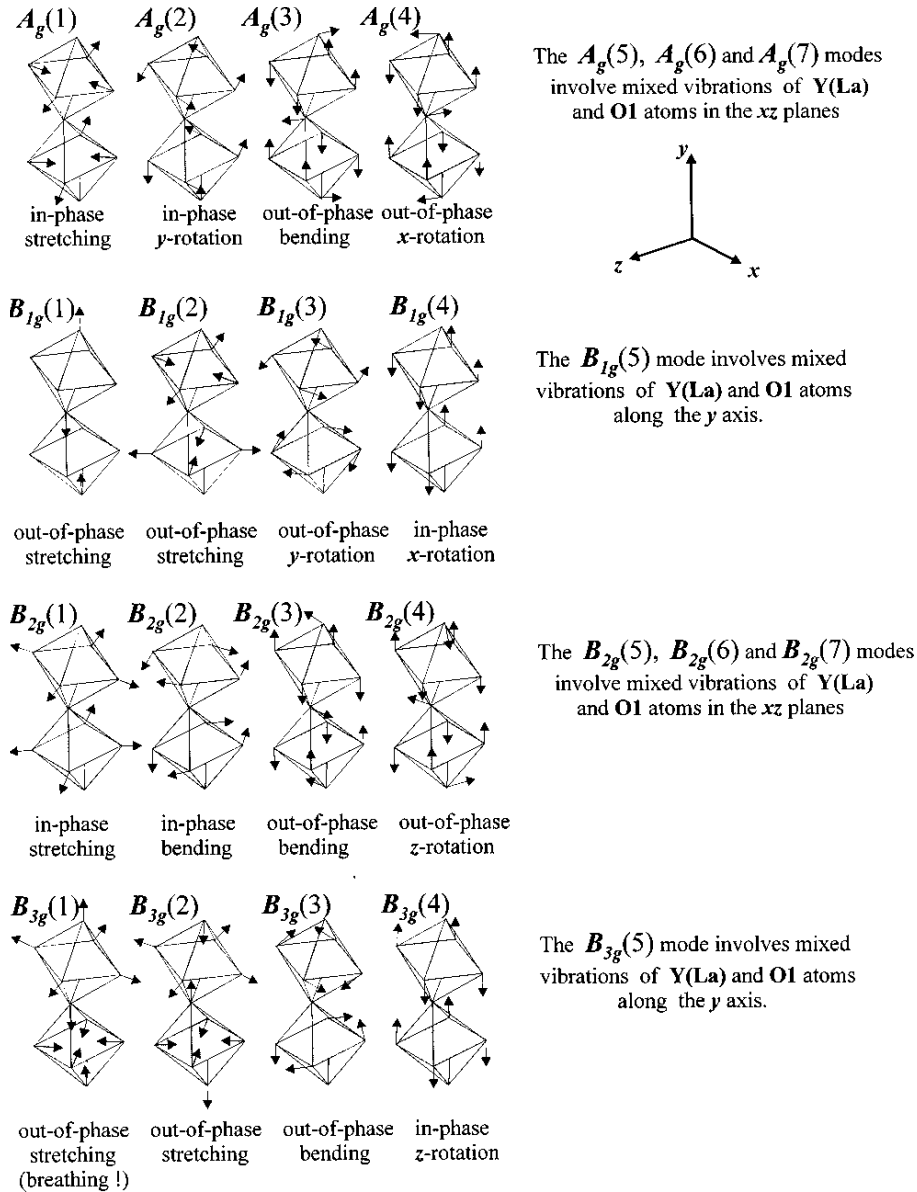


Figure 2.3: Raman-active phonon modes for orthorhombic  $\text{LaMnO}_3$  grouped by their symmetries  $A_g$ ,  $B_{1g}$ ,  $B_{2g}$  and  $B_{3g}$ . Figure taken from Ref. [Iliev et al. 1998]

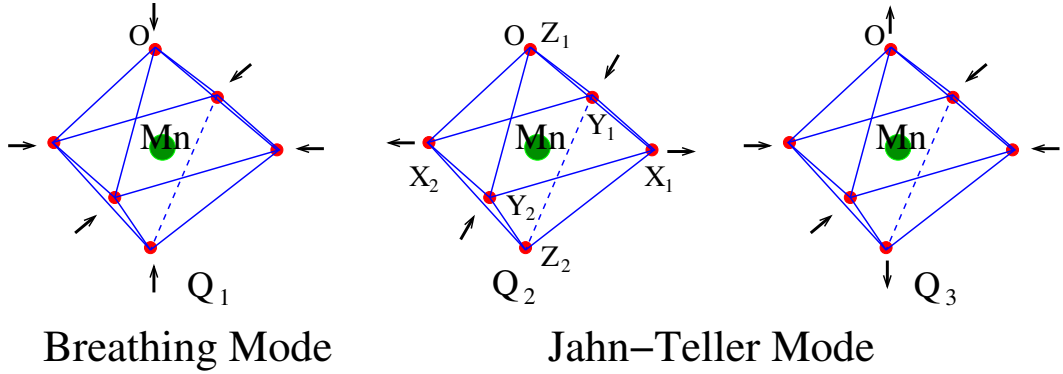


Figure 2.4: Vibration of the oxygen octahedra around manganese ion for the breathing mode  $Q_1$  and the two Jahn-Teller modes  $Q_2$  and  $Q_3$ .

modes grouped according to their symmetry ( $A_g$ ,  $B_{1g}$ ,  $B_{2g}$ ,  $B_{3g}$ ). Among the 24 Raman-active modes discussed in Ref. [Iliev et al. 1998] there are 16 modes (4 for each symmetry type) not involving vibration of the La ions. These modes correspond to the stretching, bending and rotation of the O-Mn-O bonds in the  $\text{MnO}_6$  octahedra. Due to the cooperative effect, the oxygen atoms of the neighboring octahedra may vibrate in-phase or out-of-phase.

In perovskite manganites, the most important lattice effect is the Jahn-Teller distortion of the  $\text{MnO}_6$  octahedra characterized by

$$\begin{aligned} Q_2 &= \frac{1}{\sqrt{2}}(X_1 - X_2 - Y_1 + Y_2), \\ Q_3 &= \frac{1}{\sqrt{6}}(2Z_1 - 2Z_2 - X_1 + X_2 - Y_1 + Y_2), \end{aligned} \quad (2.3)$$

where  $X_i$ ,  $Y_i$ , and  $Z_i$  are the displacements of the oxygen ions at the positive ( $i = 1$ ) and negative ( $i = 2$ ) axes from the equilibrium positions along the x-, y-, and z-directions, respectively (see Fig. 2.4).

As stated by the Jahn-Teller theorem [Jahn & Teller 1937], the cubic structure with degenerate  $e_g$  orbitals is unstable. The lattice (or the  $\text{MnO}_6$  octahedra) will be distorted and the double degeneracy of the  $e_g$  orbitals will be lifted by the distortion. According to Kanamori [Kanamori 1960], this interaction between  $e_g$  electrons and the Jahn-Teller modes can be put in the form

$$H_{ep} = -g \sum_{i;\mu\nu\sigma} c_{i\mu\sigma}^\dagger (Q_{2i}\tau^x + Q_{3i}\tau^z)_{\mu\nu} c_{i\nu\sigma}. \quad (2.4)$$

The total Hamiltonian is then

$$H = H_{KLM} + H_{ep} + \sum_{i;a=2}^3 \frac{\Omega^2}{2} Q_{ai}^2. \quad (2.5)$$

Here  $g$  is the Jahn-Teller coupling,  $\Omega$  is the frequency of the Jahn-Teller phonons, and  $Q_{ai}$  is the bosonic operator for the  $a$ -th Jahn-Teller mode at site  $i$ . In most publications, the phonons are assumed to be classical and local, and the cooperative effect of the neighboring  $\text{MnO}_6$  octahedra is neglected.

One may also include in the Hamiltonian (2.5) the breathing mode

$$Q_1 = \frac{1}{\sqrt{3}}(X_1 - X_2 + Y_1 - Y_2 + Z_1 - Z_2), \quad (2.6)$$

which couples to the electron density in the form

$$-g \sum_{i;\mu\sigma} Q_{1i} c_{i\mu\sigma}^\dagger c_{i\mu\sigma}. \quad (2.7)$$

In manganites, the breathing mode has a slightly larger frequency than the Jahn-Teller modes and is therefore often neglected. But it may well be important. We will discuss this issue later in section 5.3.

To understand the effect of the Jahn-Teller coupling, we first consider a single-site model for the two  $e_g$  orbitals. The Hamiltonian reads

$$H = -g \sum_{\mu\nu} c_\mu^\dagger (Q_2 \tau^x + Q_3 \tau^z)_{\mu\nu} c_\nu + \frac{1}{2} \sum_{a=2}^3 \Omega^2 Q_a^2. \quad (2.8)$$

The electrons are assumed to be spinless here since the Hund's coupling is large.

For single occupancy, the ground state can be expressed as

$$|\Psi\rangle = \left( \cos\left(\frac{\phi'}{2}\right) c_1^\dagger + \sin\left(\frac{\phi'}{2}\right) c_2^\dagger \right) |0\rangle. \quad (2.9)$$

Introducing new variables  $Q$  ( $\geq 0$ ) and  $\phi$  ( $-\pi \leq \phi < \pi$ ) so that

$$Q_2 = Q \sin(\phi), \quad Q_3 = Q \cos(\phi), \quad (2.10)$$

we obtain the ground state energy

$$E_{GS} = E_l + E_g, \quad (2.11)$$

where

$$E_l = \frac{1}{2} \Omega^2 Q^2 \quad (2.12)$$

is the lattice distortion energy and

$$E_g = \langle \Psi | H_g | \Psi \rangle = -gQ \cos(\phi - \phi') \quad (2.13)$$

is the electron-phonon interaction energy. Here  $H_g$  denotes the interaction part of the Hamiltonian (2.8).

Applying the variational conditions

$$\frac{\partial E}{\partial Q} = \frac{\partial E}{\partial \phi} = \frac{\partial E}{\partial \phi'} = 0, \quad (2.14)$$

we find

$$\phi = \phi', \quad Q = \frac{g}{\Omega^2}. \quad (2.15)$$

The ground state is then

$$\cos(\phi/2)|3z^2 - r^2\rangle + \sin(\phi/2)|x^2 - y^2\rangle, \quad (2.16)$$

if the original orbitals in Eq. (2.8) are  $|3z^2 - r^2\rangle$  and  $|x^2 - y^2\rangle$ . This gives the ground state energy

$$E_{GS} = -\frac{g^2}{2\Omega^2}, \quad (2.17)$$

which includes the lattice distortion energy  $E_l = -E_{GS}$  and the electron-phonon interaction energy  $E_g = 2E_{GS}$ . The energy  $g^2/2\Omega^2$  is also called the static Jahn-Teller energy ( $E_{JT}$ ). The excited state is orthogonal to the ground state and can be simply written as

$$-\sin(\phi/2)|3z^2 - r^2\rangle + \cos(\phi/2)|x^2 - y^2\rangle, \quad (2.18)$$

with a much higher energy  $E_{ex} = 3E_{JT}$ . The two  $e_g$  orbitals are split by the Jahn-Teller coupling.

Since the ground state energy is independent of  $\phi$ , the lattice distortion in the single-site model can have different orientations in the  $(Q_2, Q_3)$  plane. In real materials, the "orbital mixing angle"  $\phi$  will be fixed by other contributions such as the anharmonic terms of the potential energy and higher order couplings [Kanamori 1960, Popovic & Satpathy 2000]. More details will be discussed in section 4.3.1.

Similar physics occurs in the lattice model (2.5). In the undoped system, the splitting of the  $e_g$  orbitals can lead to an insulating ground state if the Jahn-Teller coupling is strong enough. In doped systems, the conduction electrons can be trapped by large lattice distortions and form small lattice polarons, which may be responsible for the high temperature insulating behavior in doped manganites. The theory of small polarons was first developed in [Holstein 1959a, Holstein 1959b] and later



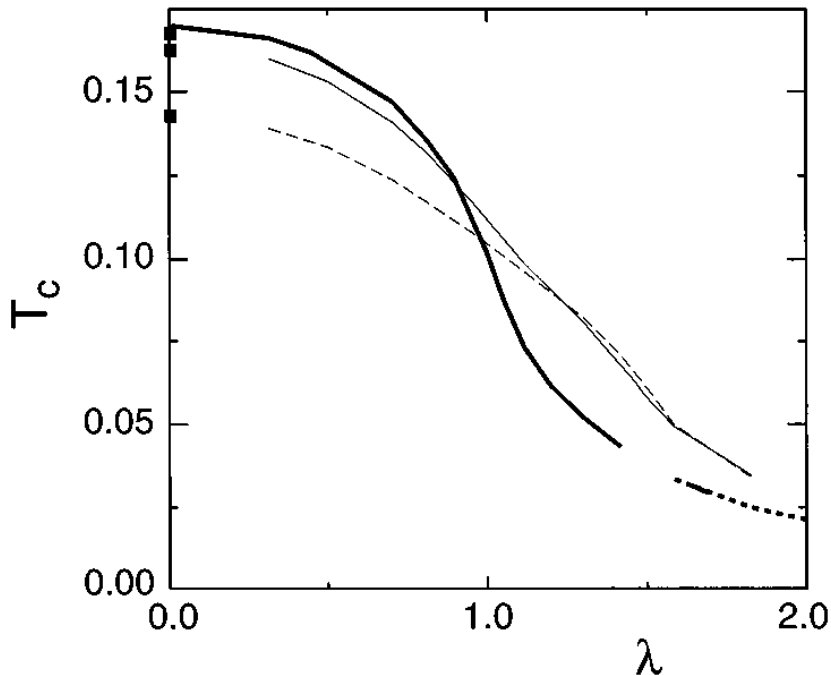


Figure 2.5: Curie temperature  $T_c$  (in units of  $W/4$ ) as a function of the electron-phonon coupling  $\lambda \equiv g^2/\Omega^2 t$  for different occupation numbers  $n=1$  (heavy solid line),  $0.75$  (light solid line), and  $0.5$  (light dashed line). The results were obtained for a two-band Kondo lattice model with Jahn-Teller phonons. Figure taken from Ref. [Millis et al. 1996c].

studied in [Sumi 1972, Sumi 1974, Ciuchi et al. 1997]. In doped manganites, the importance of the Jahn-Teller phonons was first realized in [Millis et al. 1995] and then intensively studied in the past decades [Röder et al. 1996, Millis et al. 1996a, Millis et al. 1996b, Millis et al. 1996c, Zang et al. 1996, Majumdar et al. 1999, Hotta et al. 2001, Ohsawa & Inoue 2002, Aliaga et al. 2003].

The polaron effect may account for some of the discrepancies between the experimental facts and the theoretical results of the Kondo lattice model. As an example, Fig. 2.5 shows the Curie temperature as a function of the Jahn-Teller coupling obtained for a two-band Kondo lattice model with Jahn-Teller phonons [Millis et al. 1996c]. We see that the Curie temperature is suppressed at larger coupling since the electrons are more localized by the Jahn-Teller distortion. The inclusion of the Jahn-Teller coupling thus yields a better agreement with experiments. However, the finite Curie temperature at  $n = 1$  contradicts with the antiferromagnetic spin ordering ( $T_N = 140$  K) found in  $\text{LaMnO}_3$  (see Fig. 1.2). This contradiction can only be resolved if the Coulomb interaction is taken into account.

### 2.3 Coulomb interaction

In the Kondo lattice model (2.1) the local Coulomb interaction has been neglected. For Mn ions, this is only valid when the average occupation number per site is much smaller than one so that electrons have little chance of double occupancy. If the Coulomb interaction is included, we get an extended Kondo lattice model (on the cubic lattice)

$$H = H_{KLM} + U \sum_{i;\mu} \sum_i n_{i\mu\uparrow} n_{i\mu\downarrow} + \sum_{i;\sigma\bar{\sigma}} (V - \delta_{\sigma\bar{\sigma}} F) n_{i1\sigma} n_{i2\bar{\sigma}}, \quad (2.19)$$

where  $U$  and  $V$  are the intra- and inter-orbital Coulomb interactions, respectively.  $F$  is the  $e_g$ - $e_g$  exchange interaction. Due to the cubic symmetry, we have  $V = U - 2F$ . The spin flip terms are usually neglected since they create the so-called sign problem in QMC simulations.

Without Hund's coupling  $J$ , Hamiltonian (2.19) is the Hubbard model for  $e_g$  electrons. In general, the Hubbard model has been intensively studied within DMFT, mainly with respect to the Mott physics [Imada et al. 1998]. Let us take the one-band Hubbard model as an example. Fig. 2.6 sketches the typical phase diagram of the (one-band) Hubbard model. The system is always metallic away from half

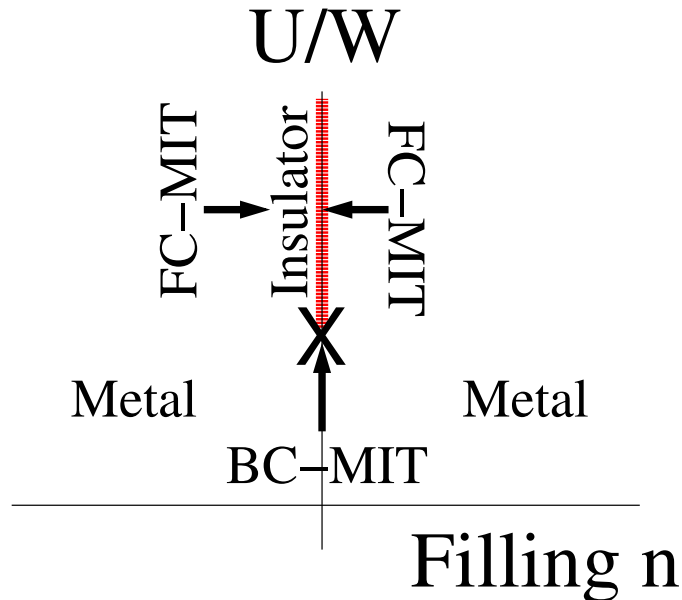


Figure 2.6: Typical phase diagram of the Hubbard model (see also [Imada et al. 1998]). Two routes for the metal-insulator transition are shown: BC-MIT (bandwidth-control metal-insulator transition) and FC-MIT (filling-control metal-insulator transition).

filling. At half filling ( $n = 1$ ), it becomes a Mott insulator if the ratio  $U/W$  is larger than a critical value.

In the insulating phase ( $n = 1$ ), the strong on-site Coulomb interaction leads to antiferromagnetic spin ordering at low temperature. This can be easily seen for  $U \rightarrow \infty$  when the perturbation in terms of  $t/U$  yields the so-called  $t - J$  model with the antiferromagnetic superexchange interaction  $J \propto t^2/U$  [Imada et al. 1998]. In the metallic phase, the effective bandwidth  $W^*$  of the quasiparticles is strongly renormalized by the Coulomb interaction so that  $W^*$  is much smaller than the bandwidth  $W$  of the free electrons.

The bandwidth-control metal-insulator transition can be achieved by applying an external pressure which changes the bandwidth of the conduction electrons. The pressure-induced (bandwidth-control) metal-insulator transition is observed typically for  $V_2O_3$  [Bao et al. 1993, Carter et al. 1993] and  $RNiO_3$  ( $R=Pr$  and  $Nd$ ) [Obradors et al. 1993]. For perovskite compounds ( $ABO_3$ ),  $W$  can also be controlled by modification of the ionic radius of the A site. This ionic radius affects the angle of the A-O-A bonds and therefore the effective bandwidth  $W$ . In chapter 4, we will discuss the pressure-induced metal-insulator transition in  $LaMnO_3$  [Loa et al. 2001].

Some of these effects of the Coulomb interaction are expected to hold also for the extended two-band Kondo lattice model (2.19). For doped systems, the reduction of the quasiparticle bandwidth is expected to enhance the localization of the conduction electrons by lattice distortion and spin disorder which are now governed by the ratios  $E_{JT}/W^*$  and  $J/W^*$ , respectively. The extended model has been studied by DMFT [Held & Vollhardt 2000]. Fig. 2.7 shows the Curie temperature as a function of doping  $x = 1 - n$ . Different from that for the original two-band Kondo lattice model (2.1), the extended model yields a maximal  $T_c$  at around  $x = 0.5$  ( $n = 0.5$ ). Close to  $n = 0$  ( $x = 1$ ), the Coulomb interaction is not effective and  $T_c$  remains almost unmodified. Close to  $n = 1$  ( $x = 0$ ), the Coulomb repulsion prevents double occupancy so that electrons are almost localized and  $T_c$  is therefore strongly suppressed. The Coulomb interaction is thus necessary to explain the doping dependence of the Curie temperature in doped manganites. Moreover, the extended model also leads to an antiferromagnetic spin ordering at  $n = 1$  ( $x = 0$ ), in agreement with the experimental fact in  $LaMnO_3$ .

## 2.4 Realistic microscopic model

To summarize our discussions, the double exchange mechanism (or the Hund's coupling to the itinerant  $e_g$  electrons) plays a crucial role for the ferromagnetism in doped manganites [Zener 1951b], but are unable to explain all the complicated fea-

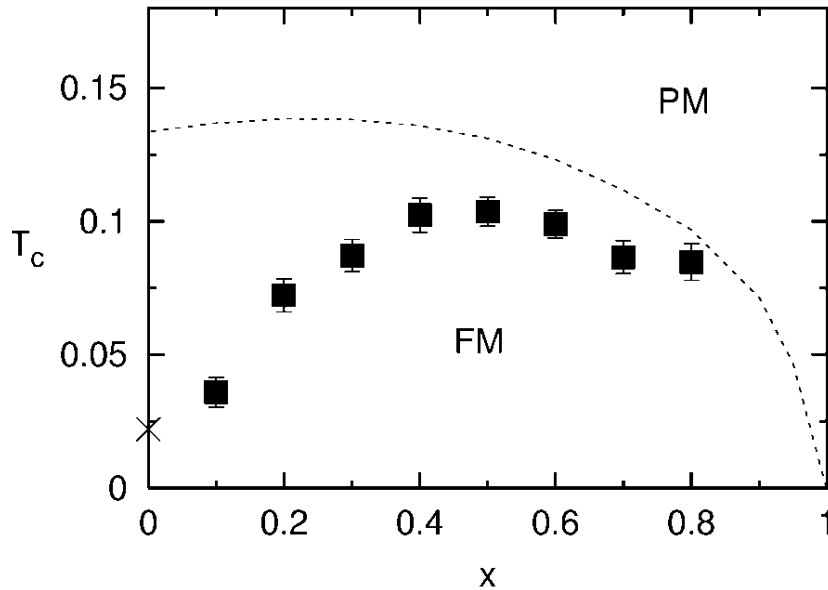


Figure 2.7: Curie temperature  $T_C$  as a function of doping  $x$  for the model Hamiltonian (2.19) obtained by DMFT. The Coulomb interactions are  $U = 8$  eV,  $V = 6$  eV and  $F = 1$  eV.  $T_C$  for pure double exchange model is also shown (dashed line) for comparison. Figure taken from Ref. [Held & Vollhardt 2000].

tures observed in experiments. The importance of the Jahn-Teller coupling was then proposed and shown to be responsible for the high temperature insulating behavior [Millis et al. 1995]. In addition, the Coulomb interaction might also be necessary for describing  $\text{LaMnO}_3$  and important in doped manganites. These considerations lead to a realistic microscopic model

$$\begin{aligned}
H = & - \sum_{\langle\langle ij \rangle\rangle; \mu\nu\sigma} t_{\mu\nu}^{ij} c_{i\mu\sigma}^\dagger c_{j\nu\sigma} - 2J \sum_{i;\mu} \mathbf{s}_{i\mu} \cdot \mathbf{S}_i \\
& + U \sum_{i;\mu} n_{i\mu\uparrow} n_{i\mu\downarrow} + \sum_{i;\sigma\bar{\sigma}} (V - \delta_{\sigma\bar{\sigma}} F) n_{i1\sigma} n_{i2\bar{\sigma}} \\
& - g \sum_{i;\mu\nu\sigma} c_{i\mu\sigma}^\dagger (Q_{2i} \tau^x + Q_{3i} \tau^z)_{\mu\nu} c_{i\nu\sigma} + \sum_{i;a} \left( \frac{P_{ai}^2}{2} + \frac{\Omega^2}{2} Q_{ai}^2 \right). \quad (2.20)
\end{aligned}$$

Here,  $c_{i\mu\sigma}^\dagger$  and  $c_{i\mu\sigma}$  are creation and annihilation operators for electrons on site  $i$  within  $e_g$  orbital  $\mu$  and spin  $\sigma$ ;  $\mathbf{s}_{i\mu}$  denotes the  $e_g$ -spin (defined as Eq. (2.2)),  $\mathbf{S}_i$  is the  $t_{2g}$ -spin, and  $Q_{ai}$  ( $P_{ai}$ ) the coordinate (momentum) of the two quantum Jahn-Teller modes.

Similar models have been proposed before but only studied in some limiting cases [Rozenberg 1998, Motome & Imada 1999a, Motome & Imada 1999b, Ferrari et al. 2001].

The strong on-site Coulomb interaction and the local Jahn-Teller phonons can be treated numerically by DMFT but the computations are very time-consuming [Blankenbecler et al. 1981, Georges et al. 1996]. Moreover, the values of the parameters such as the Coulomb interaction  $U$  and the Jahn-Teller coupling  $g$  are not yet fixed. Different estimates can be found in the literature [Bocquet et al. 1992, Satpathy et al. 1996a, Satpathy et al. 1996b, Millis et al. 1996c, Zampieri et al. 1998, Perebeinos & Allen 2000, Popovic & Satpathy 2000].

Nevertheless, to have an idea about their magnitudes before the numerical investigations, we show in this section how the values of some of the most relevant parameters can be estimated from experiments. First, we will write down a realistic tight-binding model for free  $e_g$  electrons on the cubic lattice [Slater & Koster 1954]. The phonon frequency will be directly obtained from the Raman spectroscopy data [Iliev et al. 1998] and the Coulomb interaction  $U$  will be estimated from the photoemission and x-ray absorption spectroscopy [Park et al. 1996]. In section 5.3, these results will be compared to an independent estimate based on DMFT calculations and optical data in both undoped and doped manganites.

**Hopping integral** The tight-binding Hamiltonian for the free  $e_g$  electrons on the cubic lattice of manganese ions can be expressed as

$$H_0 = - \sum_{\mathbf{ia}\mu\nu\sigma} t_{\mu\nu}^{\mathbf{a}} c_{\mathbf{i},\mu\sigma}^\dagger c_{\mathbf{i}+\mathbf{a},\nu\sigma}, \quad (2.21)$$

where  $\mathbf{a}$  denotes the vector connecting nearest-neighbor sites and  $t_{\mu\nu}^{\mathbf{a}}$  is the hopping integral between their  $\mu$ - and  $\nu$ -orbital along the  $\mathbf{a}$ -direction.

Based on the double exchange mechanism,  $t_{\mu\nu}^{\mathbf{a}}$  is a combination of the hopping integral from Mn ion to oxygen ion and vice versa,

$$\begin{aligned} -t_{\mu\nu}^x &= E_{x,\mu}(1, 0, 0) \times E_{x,\nu}(-1, 0, 0), \\ -t_{\mu\nu}^y &= E_{y,\mu}(0, 1, 0) \times E_{y,\nu}(0, -1, 0), \\ -t_{\mu\nu}^z &= E_{z,\mu}(0, 0, 1) \times E_{z,\nu}(0, 0, -1), \end{aligned} \quad (2.22)$$

where  $E_{\mathbf{a},\mu}(l, m, n)$  is the overlap integral between manganese  $\mu$ - and oxygen  $p_{\mathbf{a}}$ -orbital along  $(l, m, n)$  direction. Following Slater and Koster [Slater & Koster 1954],  $E_{\mathbf{a},\mu}(l, m, n)$  are listed in Fig. 2.8. We obtain

$$t^x = t_0 \begin{pmatrix} \frac{3}{4} & -\frac{\sqrt{3}}{4} \\ -\frac{\sqrt{3}}{4} & \frac{1}{4} \end{pmatrix}, \quad t^y = t_0 \begin{pmatrix} \frac{3}{4} & \frac{\sqrt{3}}{4} \\ \frac{\sqrt{3}}{4} & \frac{1}{4} \end{pmatrix}, \quad t^z = t_0 \begin{pmatrix} 0 & 0 \\ 0 & 1 \end{pmatrix}, \quad (2.23)$$

where  $t_0$  is a constant. Eq. (2.23) is written with respect to  $d_{3z^2-r^2}$  and  $d_{x^2-y^2}$  orbitals and provides a realistic tight-binding model for manganites. The Fourier

$E_{s,s}$	$(ss\sigma)$
$E_{s,x}$	$l(s\rho\sigma)$
$E_{x,x}$	$l^2(\rho\rho\sigma) + (1-l^2)(\rho\rho\pi)$
$E_{x,y}$	$lm(\rho\rho\sigma) - lm(\rho\rho\pi)$
$E_{x,z}$	$ln(\rho\rho\sigma) - ln(\rho\rho\pi)$
$E_{s,xy}$	$\sqrt{3}lm(sd\sigma)$
$E_{s,x^2-y^2}$	$\frac{1}{2}\sqrt{3}(l^2-m^2)(sd\sigma)$
$E_{s,3z^2-r^2}$	$[n^2 - \frac{1}{2}(l^2+m^2)](sd\sigma)$
$E_{x,xy}$	$\sqrt{3}l^2m(\rho d\sigma) + m(1-2l^2)(\rho d\pi)$
$E_{x,yz}$	$\sqrt{3}lmn(\rho d\sigma) - 2lmn(\rho d\pi)$
$E_{x,zz}$	$\sqrt{3}l^2n(\rho d\sigma) + n(1-2l^2)(\rho d\pi)$
$E_{x,x^2-y^2}$	$\frac{1}{2}\sqrt{3}l(l^2-m^2)(\rho d\sigma) + l(1-l^2+m^2)(\rho d\pi)$
$E_{y,x^2-y^2}$	$\frac{1}{2}\sqrt{3}m(l^2-m^2)(\rho d\sigma) - m(1+l^2-m^2)(\rho d\pi)$
$E_{z,x^2-y^2}$	$\frac{1}{2}\sqrt{3}n(l^2-m^2)(\rho d\sigma) - n(l^2-m^2)(\rho d\pi)$
$E_{x,3z^2-r^2}$	$l[n^2 - \frac{1}{2}(l^2+m^2)](\rho d\sigma) - \sqrt{3}ln^2(\rho d\pi)$
$E_{y,3z^2-r^2}$	$m[n^2 - \frac{1}{2}(l^2+m^2)](\rho d\sigma) - \sqrt{3}mn^2(\rho d\pi)$
$E_{z,3z^2-r^2}$	$n[n^2 - \frac{1}{2}(l^2+m^2)](\rho d\sigma) + \sqrt{3}n(l^2+m^2)(\rho d\pi)$
$E_{x,y,xy}$	$3l^2m^2(dd\sigma) + (l^2+m^2-4l^2m^2)(dd\pi) + (n^2+l^2m^2)(dd\delta)$
$E_{x,y,yz}$	$3lm^2n(dd\sigma) + ln(1-4m^2)(dd\pi) + ln(m^2-1)(dd\delta)$
$E_{x,y,zz}$	$3l^2mn(dd\sigma) + mn(1-4l^2)(dd\pi) + mn(l^2-1)(dd\delta)$
$E_{x,y,x^2-y^2}$	$\frac{3}{2}lm(l^2-m^2)(dd\sigma) + 2lm(m^2-l^2)(dd\pi) + \frac{3}{2}lm(l^2-m^2)(dd\delta)$
$E_{y,z,x^2-y^2}$	$\frac{3}{2}mn(l^2-m^2)(dd\sigma) - mn[1+2(l^2-m^2)](dd\pi) + mn[1+\frac{1}{2}(l^2-m^2)](dd\delta)$
$E_{z,z,x^2-y^2}$	$\frac{3}{2}nl(l^2-m^2)(dd\sigma) + nl[1-2(l^2-m^2)](dd\pi) - nl[1-\frac{1}{2}(l^2-m^2)](dd\delta)$
$E_{x,y,3z^2-r^2}$	$\sqrt{3}lm[n^2 - \frac{1}{2}(l^2+m^2)](dd\sigma) - 2\sqrt{3}lmn^2(dd\pi) + \frac{1}{2}\sqrt{3}lm(1+n^2)(dd\delta)$
$E_{y,z,3z^2-r^2}$	$\sqrt{3}mn[n^2 - \frac{1}{2}(l^2+m^2)](dd\sigma) + \sqrt{3}mn(l^2+m^2-n^2)(dd\pi) - \frac{1}{2}\sqrt{3}mn(l^2+m^2)(dd\delta)$
$E_{z,z,3z^2-r^2}$	$\sqrt{3}ln[n^2 - \frac{1}{2}(l^2+m^2)](dd\sigma) + \sqrt{3}ln(l^2+m^2-n^2)(dd\pi) - \frac{1}{2}\sqrt{3}ln(l^2+m^2)(dd\delta)$
$E_{x^2-y^2,x^2-y^2}$	$\frac{2}{3}(l^2-m^2)^2(dd\sigma) + [l^2+m^2-(l^2-m^2)^2](dd\pi) + [n^2+\frac{1}{3}(l^2-m^2)^2](dd\delta)$
$E_{x^2-y^2,3z^2-r^2}$	$\frac{1}{2}\sqrt{3}(l^2-m^2)[n^2 - \frac{1}{2}(l^2+m^2)](dd\sigma) + \sqrt{3}n^2(m^2-l^2)(dd\pi) + \frac{1}{4}\sqrt{3}(1+n^2)(l^2-m^2)(dd\delta)$
$E_{3z^2-r^2,3z^2-r^2}$	$[n^2 - \frac{1}{2}(l^2+m^2)]^2(dd\sigma) + 3n^2(l^2+m^2)(dd\pi) + \frac{3}{4}(l^2+m^2)^2(dd\delta)$

Figure 2.8: Overlap integral  $E_{\mu\nu}(l, m, n)$  between  $\mu$ - and  $\nu$ -orbitals of two ions along  $(l, m, n)$  direction. Figure taken from Ref. [Slater & Koster 1954].

transform

$$c_{\mathbf{k}\mu\sigma} = \frac{1}{N} \sum_{i=1}^N e^{i\mathbf{r}_i \cdot \mathbf{k}} c_{i\mu\sigma} \quad (2.24)$$

yields the dispersion

$$\epsilon_{\mathbf{k}}^{\mu\nu} = -2 \sum_{\mathbf{a}=x,y,z} t_{\mu\nu}^{\mathbf{a}} \cos(\mathbf{k}_a), \quad (2.25)$$

with a bandwidth  $W = 6t_0$ . A recent LDA calculation gives  $W \approx 3.6$  eV for cubic LaMnO<sub>3</sub> and  $W \approx 3.0$  eV for orthorhombic LaMnO<sub>3</sub> at ambient pressure [Yamasaki et al. 2006]. Other different estimates can be found in the review article [Dagotto et al. 2001].

**Phonon frequency** Following Ref. [Iliev et al. 1998], Fig. 2.9 shows the Raman spectra of orthorhombic LaMnO<sub>3</sub>. The peaks correspond to the Raman-active modes

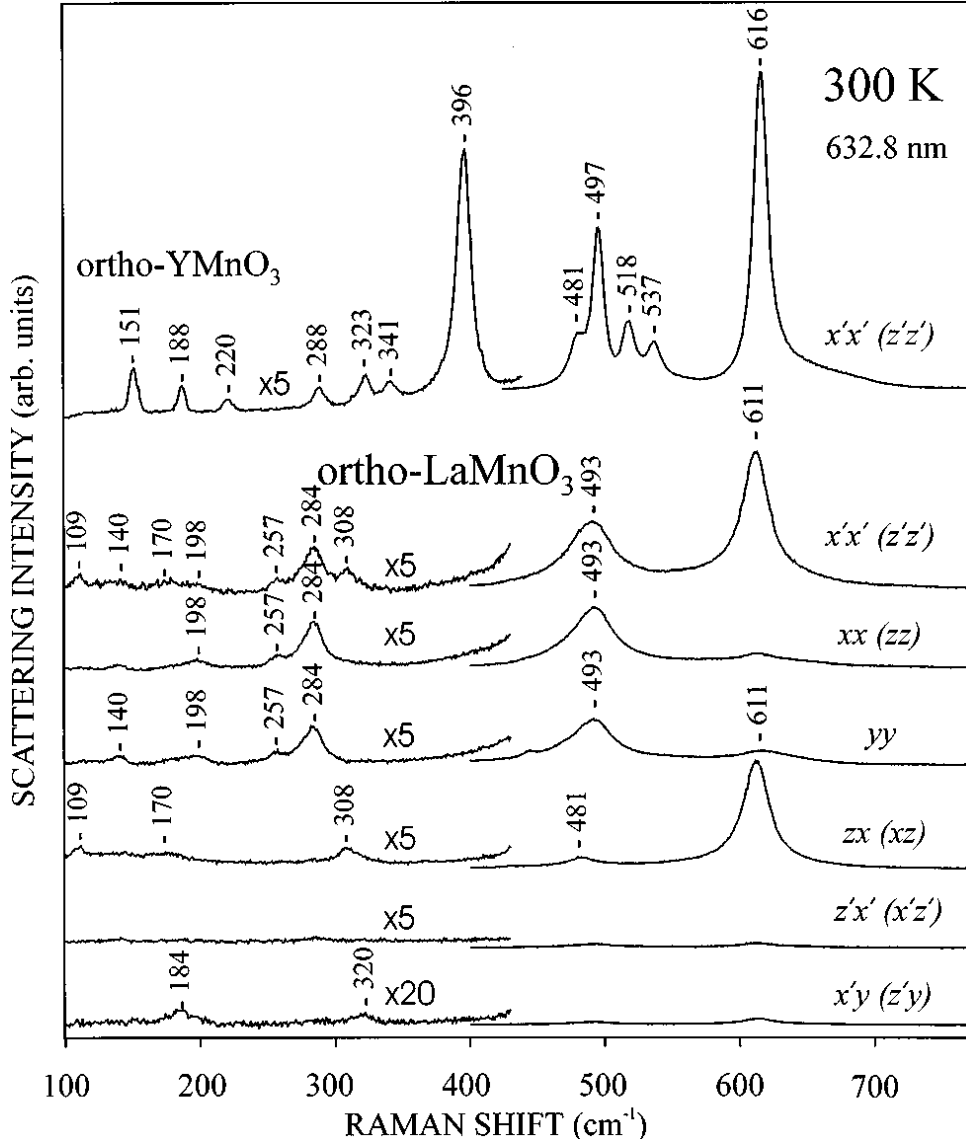


Figure 2.9: Polarized Raman spectra of orthorhombic  $\text{LaMnO}_3$  in various scattering configuration  $xx, yy$  and so on. The  $zz$  spectrum of  $\text{YMnO}_3$  is also shown for comparison. The left half of the spectra are multiplied by the factor indicated there. Figure taken from Ref. [Iliev et al. 1998]

sketched in Fig. 2.3. They can be identified by comparing to the lattice dynamical calculations shown in Fig. 2.10. We see that the experimental and numerical results are consistent. Comparing Fig. 2.3 and Fig. 2.4, we estimate that the frequency of the Jahn-Teller modes is  $500 - 600 \text{ cm}^{-1}$  or approximately  $\Omega_{JT} = 0.07 \text{ eV}$ , and the frequency of the breathing mode ( $Q_1$ ) is  $600 - 700 \text{ cm}^{-1}$  or approximately  $\Omega_{br} =$

Mode	YMnO <sub>3</sub> exp.	YMnO <sub>3</sub> LDC	LaMnO <sub>3</sub> exp.	LaMnO <sub>3</sub> LDC	Assign ment
$A_g$	<b>151</b>	<b>104</b>	<b>140</b>	<b>81</b>	$R(x)$
$A_g$	<b>188</b>	<b>147</b>	<b>198</b>	<b>162</b>	$R(z)$
$A_g$	<b>288</b>	<b>223</b>	<b>257</b>	<b>246</b>	$A_g(2)$
$A_g$	<b>323</b>	<b>304</b>		<b>263</b>	$O1(x)$
$A_g$	<b>396</b>	<b>407</b>	<b>284</b>	<b>326</b>	$A_g(4)$
$A_g$	<b>497</b>	<b>466</b>	<b>493</b>	<b>480</b>	$A_g(3)$
$A_g$	<b>518</b>	<b>524</b>		<b>582</b>	$A_g(1)$
$B_{1g}$	<b>205</b>	<b>181</b>	<b>184</b>	<b>182</b>	$R(y)$
$B_{1g}$	<b>284</b>	<b>288</b>		<b>254</b>	$B_{1g}(3)$
$B_{1g}$	<b>383</b>	<b>342</b>		<b>347</b>	$B_{1g}(4)$
$B_{1g}$		<b>413</b>		<b>575</b>	$B_{1g}(2)$
$B_{1g}$		<b>593</b>		<b>693</b>	$B_{1g}(1)$
$B_{2g}$	<b>151</b>	<b>137</b>	<b>109</b>	<b>123</b>	$R(z)$
$B_{2g}$	<b>220</b>	<b>162</b>	<b>170</b>	<b>150</b>	$R(x)$
$B_{2g}$	<b>317</b>	<b>285</b>		<b>218</b>	$B_{2g}(4)$
$B_{2g}$	<b>341</b>	<b>393</b>	<b>308</b>	<b>369</b>	$O1(z)$
$B_{2g}$	<b>481</b>	<b>470</b>	<b>481</b>	<b>464</b>	$B_{2g}(3)$
$B_{2g}$	<b>537</b>	<b>583</b>		<b>509</b>	$B_{2g}(2)$
$B_{2g}$	<b>616</b>	<b>617</b>	<b>611</b>	<b>669</b>	$B_{2g}(1)$
$B_{3g}$	<b>178</b>	<b>145</b>		<b>158</b>	$R(y)$
$B_{3g}$	<b>336</b>	<b>363</b>	<b>320</b>	<b>343</b>	$B_{3g}(4)$
$B_{3g}$		<b>390</b>		<b>462</b>	$B_{3g}(3)$
$B_{3g}$		<b>476</b>		<b>603</b>	$B_{3g}(2)$
$B_{3g}$		<b>610</b>		<b>692</b>	$B_{3g}(1)$

Figure 2.10: Comparison of the experimental and numerical (lattice dynamical calculation) results of the Raman frequencies (unit  $\text{cm}^{-1}$ ) for  $\text{LaMnO}_3$  and  $\text{YMnO}_3$  with  $Pnma$  structure. Table taken from Ref. [Iliev et al. 1998]

0.08 eV. These results are supported by optical experiments which show a sharp peak located at around 0.07 eV in the optical reflectivity spectra [Okimoto et al. 1995, Jung et al. 1998, Takenaka et al. 1999, Tobe et al. 2004]. For simplicity, we take  $\Omega = 0.07$  eV for all the three modes in this work.



**Coulomb interaction** The Coulomb interaction can either be calculated by the constrained LDA method or estimated by experiments. In the constrained LDA method [Dederichs et al. 1984, Gunnarsson et al. 1989, Anisimov & Gunnarsson 1991, Solovyev & Dederichs 1994], the interacting  $d$ - or  $f$ -electrons of one site are kinetically decoupled from the rest of the system. By changing the number  $n_d$  of the interacting electrons on this site, the ground state energy can be calculated by LDA. Using the fitting function

$$E(n_d) = E_0 + \frac{1}{2}\bar{U}n_d(n_d - 1) + (\epsilon_d^{LDA} + \Delta\epsilon_d)n_d, \quad (2.26)$$

we can obtain the average Coulomb interaction  $\bar{U}$  and the interaction modification of the LDA energy  $\Delta\epsilon_d$  which can be absorbed into the LDA Hamiltonian. In the case of  $\text{LaMnO}_3$  with two  $e_g$  orbitals, the average Coulomb interaction is

$$\bar{U} = \frac{U + U - 2F + U - 3F}{3} = U - \frac{5}{3}F. \quad (2.27)$$

In Ref. [Satpathy et al. 1996a], the on-site Coulomb interaction is estimated to be  $8 - 10$  eV and  $J, F \approx 0.9$  eV for  $\text{LaMnO}_3$  and  $\text{CaMnO}_3$ . Taking into account the screening effects, the effective Coulomb interaction can be much smaller. In Ref. [Yamasaki et al. 2006], LDA calculations for the ferromagnetic phase produce a similar result of  $J \approx 0.9$  eV.

The Coulomb interaction can also be estimated by experiments. However, to the best of our knowledge, there is no generally accepted estimate of the Coulomb interaction  $U$  for manganites. As an example, we show here how the Coulomb interaction can be estimated from high resolution photoemission spectroscopy (PES) and x-ray absorption spectroscopy (XAS) [Park et al. 1996]. The basic idea is to measure the binding energy of the localized electrons by photoemission and the lowest excitation energy by oxygen  $1s$  x-ray absorption spectroscopy. For charge-transfer insulator and Mott-Hubbard insulator, the separation between the binding and excitation energies corresponds to the smaller one of the charge transfer energy  $\Delta_{ct}$  and the Coulomb energy  $\bar{U}$  [Zaanen et al. 1985].

Fig. 2.11 plots the one electron removal ( $N \rightarrow N - 1$ , PES) and addition ( $N \rightarrow N + 1$ , XAS) spectra of  $\text{LaMnO}_3$  and  $\text{CaMnO}_3$ . The three states with  $N - 1$ ,  $N$  and  $N + 1$  electrons are identified as  $t_{2g}^2(^3T_1)$ ,  $t_{2g}^3(^4A_2)$  and  $t_{2g}^3e_g^1(^5E)$  for  $\text{CaMnO}_3$  ( $Mn^{4+}$ ) and  $t_{2g}^3(^4A_2)$ ,  $t_{2g}^3e_g^1(^5E)$  and  $t_{2g}^3e_g^2(^6A_1)$  for  $\text{LaMnO}_3$  ( $Mn^{3+}$ ). The symbol in the bracket indicates the symmetry of the state. In Fig. 2.11, the states  $N \pm 1$  are denoted by vertical lines. The energy difference between these two states can be read directly, giving  $E_{CF}^{4+} = 3.2 \pm 0.4$  eV for  $\text{CaMnO}_3$  and  $E_{CF}^{3+} = 3.4 \pm 0.4$  eV for  $\text{LaMnO}_3$ . On the other hand, the charge transfer energy  $\Delta_{ct}$  was estimated to be

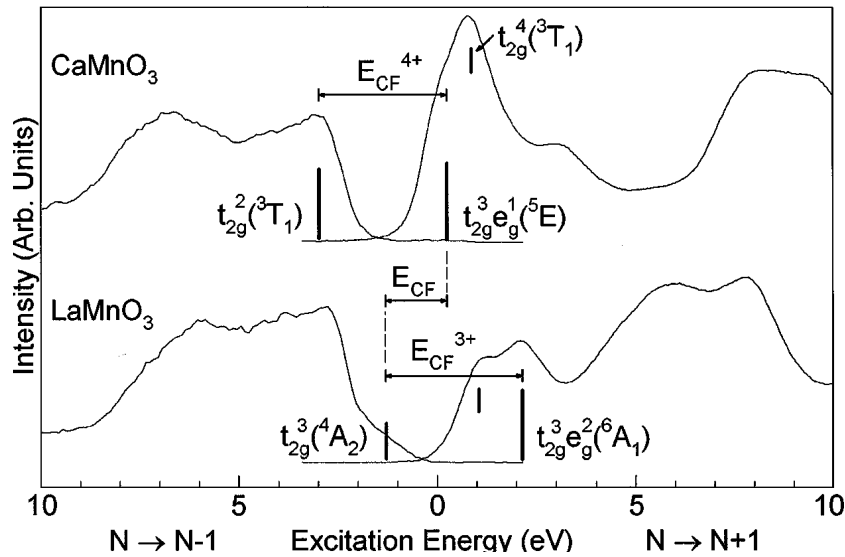


Figure 2.11: Photoemission spectra ( $N \rightarrow N - 1$ ) and  $O 1s$  x-ray absorption spectra ( $N \rightarrow N + 1$ ) for  $\text{CaMnO}_3$  and  $\text{LaMnO}_3$ . The  $O 1s$  spectra are shifted to agree with its inverse photoemission spectrum for  $\text{LaMnO}_3$ . The 1 eV shoulder in the XAS spectra of  $\text{LaMnO}_3$  is not intrinsic but due to excess oxygen which introduces extra  $\text{Mn}^{4+}$  as Ca dopant does. Figure taken from Ref. [Park et al. 1996].

W	U	J (F)	$\Omega$	$\Delta_{cf}$
3.0 – 3.6 eV	3 – 4 eV	$\approx 0.9$ eV	0.07 – 0.08 eV	1 – 2 eV

Table 2.1: Parameters estimated for  $\text{LaMnO}_3$ . W: bandwidth; U: intra-orbital Coulomb interaction; F: exchange interaction; J: Hund’s coupling;  $\Omega$ : phonon frequency;  $\Delta_{cf}$ : crystal field splitting for orthorhombic  $\text{LaMnO}_3$ .

$3.0 \pm 0.5$  eV for  $\text{CaMnO}_3$  and  $4.5 \pm 0.5$  eV for  $\text{LaMnO}_3$  [Park et al. 1996]. Thus the energy separation in Fig. 2.11 gives the average Coulomb interaction  $\bar{U} \approx 3.5$  eV for  $\text{LaMnO}_3$ . If a crystal field splitting 1 – 2 eV is subtracted [Yamasaki et al. 2006], the Coulomb interaction  $U$  is estimated to be 3 – 4 eV, which is also supported by spectral ellipsometry for  $\text{LaMnO}_3$  [Kovaleva et al. 2004].

To summarize, we have estimated the parameters of the realistic model (2.20) from experiments. The results are collected in Table 2.1. Very different estimates can be found in the literature (see, e.g., [Dagotto et al. 2001]). An independent estimate of these parameters will be presented in section 5.3 by fitting DMFT results to optical data in both undoped and doped manganites.

## 3 Dynamical mean-field theory

In this chapter, we discuss the dynamical mean-field theory (DMFT) which represents the presently most reliable method for the local dynamics of a quantum many-body system. In section 3.1, we take the Holstein model and the one-band Hubbard model as examples to show how DMFT with quantum Monte Carlo (QMC) simulations as an impurity solver can be implemented in practice for coupled boson-fermion systems. The QMC simulations produce Green's function in imaginary time. Real frequency results, e.g, the spectral density, are obtained by using the maximum entropy method which is introduced in section 3.2. For direct comparisons with experiments, we also derive the formula for the optical conductivity (section 3.3) and the spin susceptibility (section 3.4) within DMFT. In section 3.5, a brief introduction is given to the LDA and LDA+DMFT approaches which will be used in the next chapter to study the pressure-induced metal-insulator transition in  $\text{LaMnO}_3$ .

### 3.1 Dynamical mean-field theory

The basic idea of DMFT is to approximate a lattice problem by a single-site problem. The site is assumed to be coupled to an effective bath resembling the rest of the lattice. In this way, a huge number of degrees of freedom are reduced into the effective bath and the problem is simplified dramatically [Georges et al. 1996]. The most successful application of DMFT is the study of the Mott transition in the half-filled Hubbard model [Rozenberg et al. 1992, Georges & Krauth 1992, Georges & Krauth 1993, Pruschke et al. 1993a, Pruschke et al. 1993b, Zhang et al. 1993, Caffarel&Krauth 1994, Laloux et al. 1994, Rozenberg et al. 1994a, Rozenberg et al. 1994b, Moeller et al. 1995].

The mathematical reason of DMFT is the simplification of the lattice problem in the limit of infinite dimensions ( $d \rightarrow \infty$ ), which was first realized by Metzner and Vollhardt in 1989 [Metzner & Vollhardt 1989]. After proper scaling of the hopping integral to keep the kinetic energy per site finite,

$$t_{ij} \rightarrow \frac{t_{ij}}{\sqrt{d}^{|i-j|}}, \quad (3.1)$$

the self-energy  $\Sigma(\mathbf{r}_i, \mathbf{r}_j; i\omega_n)$  in infinite dimensions can be proved by perturbation theory to have only local elements [Müller-Hartmann 1989a, Müller-Hartmann 1989c,

Müller-Hartmann 1989b]

$$\Sigma(\mathbf{r}_i, \mathbf{r}_j; i\omega_n) \stackrel{d \rightarrow \infty}{\equiv} \Sigma(i\omega_n)\delta_{ij}, \quad (3.2)$$

where  $\omega_n$  is the Matsubara frequency and  $\mathbf{r}_i$  the position of the  $i$ -th lattice site. Also the Luttinger-Ward functional  $\Phi[G(i\omega_n)]$  depends only on the local Green's function  $G(i\omega_n) \equiv G(\mathbf{r}_i, \mathbf{r}_i; i\omega_n)$  so that

$$\Sigma(i\omega_n) = \frac{\delta\Phi[G(i\omega_n)]}{\delta G(i\omega_n)}, \quad (3.3)$$

together with the Dyson equation

$$G(i\omega_n) = \frac{1}{\mathcal{V}} \sum_{\mathbf{k}} \frac{1}{i\omega_n + \mu - \epsilon_{\mathbf{k}} - \Sigma(i\omega_n)}, \quad (3.4)$$

implies a self-consistent solution for the local quantities of the original lattice problem [Georges et al. 1996]. Here  $\mu$  is the chemical potential and  $\epsilon_{\mathbf{k}}$  the dispersion of the lattice model,

It was later realized that the above method is equivalent to approximate the lattice model by an Anderson impurity coupled to an effective bath [Ohkawa 1991a, Ohkawa 1991b, Georges & Krauth 1992]. In infinite dimensions, DMFT is exact. In finite dimensions, it still provides a good approximation as long as spatial fluctuations are small. The self-consistent functional equations can in general be derived by the cavity method [Georges et al. 1996], in which one separates a local site from the rest of the system, the hopping terms from this selected site to the rest of the system are treated as an external source, and all the other degrees of freedom are then integrated out to give the local effective action. The self-consistent functional equations for  $G(i\omega_n)$  and  $\Sigma(i\omega_n)$  have been derived for the periodic Anderson model [Kuramoto & Watanabe 1987], the Falicov-Kimball model [Brandt & Mielsch 1989, Brandt & Mielsch 1990, Brandt & Mielsch 1991] and the Hubbard model [Janiš 1991, Ohkawa 1991a, Ohkawa 1991b, Georges & Kotliar 1992, Jarrell 1992].

To see how DMFT works, we take the one-band Hubbard model as an example. The Hamiltonian reads

$$H = - \sum_{\langle ij \rangle \sigma} t_{ij} (c_{i\sigma}^\dagger c_{j\sigma} + c_{j\sigma}^\dagger c_{i\sigma}) + U \sum_i n_{i\uparrow} n_{i\downarrow}. \quad (3.5)$$

In DMFT, the local Green's function on a single site is given by the functional equation

$$G(\tau) = -\frac{1}{\mathcal{Z}} \int [\mathcal{D}c^\dagger \mathcal{D}c] c_\sigma(\tau) c_\sigma^\dagger(0) e^{-S}, \quad (3.6)$$

where the partition function is defined as

$$\mathcal{Z} = \int [\mathcal{D}c^\dagger \mathcal{D}c] e^{-S}. \quad (3.7)$$

The rest of the system has been integrated out, giving the effective action

$$S = - \int_0^\beta d\tau \int_0^\beta d\tau' \sum_\sigma c_\sigma^\dagger(\tau) \mathcal{G}_0^{-1}(\tau - \tau') c_\sigma(\tau') + U \int_0^\beta d\tau n_\uparrow(\tau) n_\downarrow(\tau). \quad (3.8)$$

Here  $\beta = 1/T$  is the inverse temperature and  $\mathcal{G}_0^{-1}(\tau - \tau')$  plays the role of the Weiss effective field in the mean-field theory. It can be shown that [Georges et al. 1996]

$$\mathcal{G}_0^{-1}(i\omega_n) = G^{-1}(i\omega_n) + \Sigma(i\omega_n), \quad (3.9)$$

where

$$\begin{aligned} \mathcal{G}_0(i\omega_n) &= \int_0^\beta d\tau e^{i\omega_n \tau} \mathcal{G}_0(\tau), \\ G(i\omega_n) &= \int_0^\beta d\tau e^{i\omega_n \tau} G(\tau). \end{aligned} \quad (3.10)$$

Since the local Green's function  $G(i\omega_n)$  is also related to the local self-energy  $\Sigma(i\omega_n)$  by the Dyson equation, Eqs. (3.4), (3.6) and (3.9) form a self-consistent set of equations for the one-band Hubbard model (3.5). The solution can be obtained numerically. We can first take an arbitrary input  $\Sigma(i\omega_n)$ .  $\mathcal{G}_0(i\omega_n)$  is then calculated from Eqs. (3.4) and (3.9). If the impurity model (3.8) can be solved, we get  $G(i\omega_n)$  which, together with  $\mathcal{G}_0(i\omega_n)$ , yields a new  $\Sigma(i\omega_n)$  from Eq. (3.9). For clarity, the whole DMFT procedure is shown in Fig. 3.1. The iteration continues until a self-consistent solution  $(\Sigma, G)$  is reached.

Thus the main task of DMFT is to solve the impurity model (3.8). In the past decades, many methods developed originally for the Anderson impurity problem [Hewson 1993] have been implemented as impurity solvers of DMFT. The perturbation approach [Yamada 1975, Yosida & Yamada 1975] was turned into the iterated perturbation theory (IPT) [Georges & Krauth 1992]. The quantum Monte Carlo algorithm by Hirsch and Fye [Hirsch & Fye 1986] was generally applied [Jarrell 1992, Rozenberg et al. 1992, Georges & Krauth 1992], as well as the exact diagonalization technique (ED) [Caffarel & Krauth 1994, Si et al. 1994], the numerical renormalization group theory (NRG) [Sakai & Kuramoto 1994], the non-crossing approximation (NCA) [Pruschke et al. 1993a], the equation of motion approach (EOM) [Gros 1994], etc.

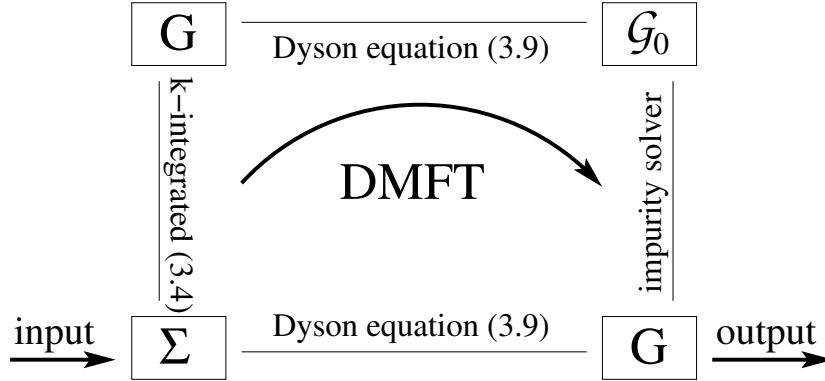


Figure 3.1: *DMFT self-consistent loop.* Given an arbitrary input  $\Sigma$ , the on-site Green's function  $G$  and the Weiss effective field  $\mathcal{G}_0$  are calculated from Eqs. (3.4) and (3.9). The effective impurity model can be solved in many different ways, producing the local interacting Green's function  $G$ . A new  $\Sigma$  then follows from Eq. (3.9). The loop is iterated until a converged set  $(\Sigma, G)$  is reached.

Each method has its own advantages and disadvantages. IPT, NCA, and EOM are simple but limited because of their inherent approximations, while QMC and NRG are exact methods but both require a huge computational effort. NRG allows for calculations at very low temperature but the computational effort increases exponentially with the number of the local degrees of freedom. Thus for multi-orbital systems, one usually uses QMC as the impurity solver since its numerical effort only grows quadratically with the number of the local degrees of freedom. However, the computational time of (finite temperature) QMC increases strongly (cubically) with decreasing temperature so that we can only work at relative high temperatures.

The basic idea of QMC is to generate a set of field configurations such that the functional integral can be replaced by the averaging over these configurations, for each of which the physical quantities such as the Green's function can be solved exactly. For the detail of the method, we refer to the review article [Foulkes et al. 2001]. In the following, we take the Holstein model and one-band Hubbard model as examples to show how QMC can be used to treat local electron-phonon and electron-electron interactions in coupled boson-fermion systems, respectively.

### 3.1.1 Holstein model

In this section, we show how QMC can be implemented for coupled boson-fermion systems without electron-electron interactions [Blankenbecler et al. 1981]. We take

the one-band Holstein model as an example. The Hamiltonian reads

$$H = - \sum_{\langle ij \rangle_\sigma} t_{ij} (c_{i\sigma}^\dagger c_{j\sigma} + c_{j\sigma}^\dagger c_{i\sigma}) - g \sum_i n_i \phi_i + \frac{1}{2} \sum_i (\pi_i^2 + \omega^2 \phi_i^2), \quad (3.11)$$

where  $\phi_i$  is the local Holstein phonon at site  $i$  and  $\pi_i$  is the conjugate momentum of  $\phi_i$ . In DMFT, the effective action of the associated impurity model is written as

$$S = - \int_0^\beta d\tau \int_0^\beta d\tau' \sum_\sigma c_\sigma^\dagger(\tau) (\mathcal{G}_0^\sigma)^{-1}(\tau - \tau') c_\sigma(\tau') - g \int_0^\beta d\tau n(\tau) \phi_\tau + \frac{1}{2} \int_0^\beta d\tau ((\phi'_\tau)^2 + \omega^2 \phi_\tau^2), \quad (3.12)$$

where  $\phi_\tau \equiv \phi(\tau)$  and  $\phi'_\tau \equiv d\phi(\tau)/d\tau$ . We have

$$\begin{aligned} G(\tau) &= -\frac{1}{\mathcal{Z}} \int [\mathcal{D}c^\dagger \mathcal{D}c \mathcal{D}\phi] c_\sigma(\tau) c_\sigma^\dagger(0) e^{-S}, \\ \mathcal{Z} &= \int [\mathcal{D}c^\dagger \mathcal{D}c \mathcal{D}\phi] e^{-S}. \end{aligned} \quad (3.13)$$

Here  $\mathcal{D}\cdot$  denotes the path integral over the Grassmann variables  $\{c_\sigma^\dagger, c_\sigma\}$  or the phonon field  $\phi(\tau)$ . Discretizing the inverse temperature  $\beta$  into  $L$  time slices  $\tau_l = (l-1)\Delta\tau$ , ( $l = 1, \dots, L+1$ ) of size  $\Delta\tau = \beta/L$ , we can define

$$G_{mn}^\sigma(\{\phi_l\}) = -\frac{1}{\mathcal{Z}_{\{\phi_l\}}} \int [\mathcal{D}c^\dagger \mathcal{D}c] c_{m\sigma} c_{n\sigma}^\dagger e^{-S_{\{\phi_l\}}}, \quad (3.14)$$

where  $c_{m\sigma} = c_\sigma(\tau_m)$  and

$$\begin{aligned} \mathcal{Z}_{\{\phi_l\}} &= \int [\mathcal{D}c^\dagger \mathcal{D}c] e^{-S_{\{\phi_l\}}}, \\ S_{\{\phi_l\}} &= - \sum_{\sigma; l, m=1}^L c_{l\sigma}^\dagger (\mathcal{G}_0^\sigma)^{-1}_{lm} c_{m\sigma} - g \Delta\tau \sum_{l=1}^L n_l \phi_l + K(\{\phi_l\}), \\ K(\{\phi_l\}) &= \frac{\Delta\tau}{2} \sum_{l=1}^L \left[ \left( \frac{\phi_{l+1} - \phi_l}{\Delta\tau} \right)^2 + \omega^2 \phi_l^2 \right], \end{aligned} \quad (3.15)$$

with periodic condition  $\phi_{L+1} = \phi_1$ . The kinetic energy of the phonon fields is sometimes written as [Blankenbecler et al. 1981]

$$K(\{\phi_l\}) = \frac{\Delta\tau}{2} \sum_{l=1}^L [(P_+^2 + P_-^2) \phi_l^2 - 2P_+ P_- \phi_l \phi_{l+1}], \quad (3.16)$$

with

$$P_+ = \frac{e^{\Delta\Omega/2}}{\sqrt{2\Delta\tau}}, \quad P_- = \frac{e^{-\Delta\Omega/2}}{\sqrt{2\Delta\tau}}. \quad (3.17)$$

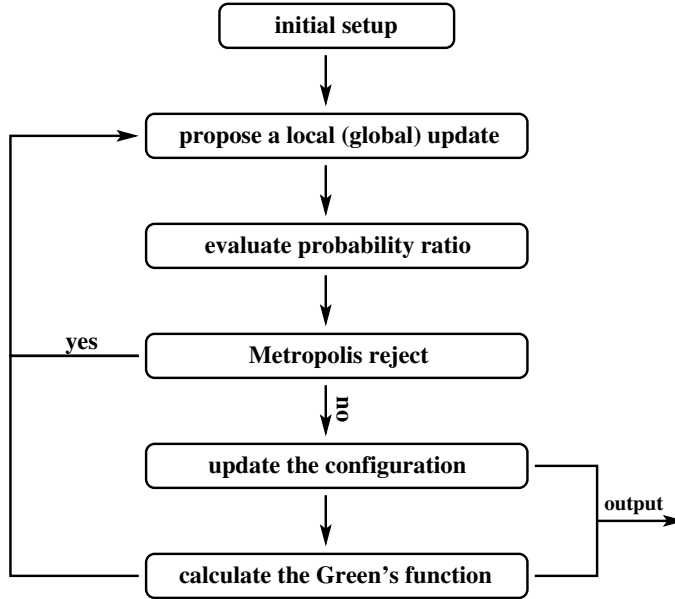


Figure 3.2: QMC updating procedure. Details can be found in the text. A global update is usually proposed after several local updates. To use the output set for the expectation value of the physical quantities, one has to take care of the correlations between sampled configurations.

Eq. (3.16) reduces to Eq. (3.15) in the limit  $\Omega\Delta\tau \ll 1$ . It has the advantage that the boson correlation functions at finite  $\Delta\tau$  reduce to the continuum ones for  $g = 0$  [Blankenbecler et al. 1981].

The on-site Green's function  $G_{mn}^\sigma$  is then given by

$$G_{mn}^\sigma = \sum_{\{\phi_l\}} \frac{\mathcal{Z}_{\{\phi_l\}}}{\mathcal{Z}} G_{mn}^\sigma(\{\phi_l\}), \quad (3.18)$$

where  $\mathcal{Z}_{\{\phi_l\}}/\mathcal{Z}$  measures the probability of the configuration  $\{\phi_l\}$ . The path integral over  $\phi(\tau)$  is replaced by the sum over the discretized field configurations  $\{\phi_l\}$  which can be evaluated numerically by QMC.

The whole QMC procedure is presented in Fig. 3.2. We start from an initial configuration, e.g.,  $\{\phi_l = 0\}$  and pick up randomly a time slice  $\tau_m$ . Then a random number  $x$  is drawn from the uniform distribution on the interval  $[0, 1]$ . We consider a change at  $\tau_m$  from  $\phi_m$  to  $\phi'_m = \phi_m + (x - 1/2)\delta\phi$ .  $\delta\phi$  is a fixed number and controls the range of the proposed change. Depending on the parameters, it should be carefully tuned. If  $\delta\phi$  is too small, it would take a long time to cover all the important configurations; whereas if  $\delta\phi$  is too large, the configuration space would not be well sampled.



To generate a proper sampling, we need to know the probability ratio of the new and old configurations,

$$R \equiv \frac{\mathcal{Z}_{\{\phi'_l\}}}{\mathcal{Z}_{\{\phi_l\}}}. \quad (3.19)$$

The Metropolis algorithm will guarantee that the configurations are sampled according to their contributions to the partition function [Metropolis et al. 1953]. The algorithm states: the new configuration  $\{\phi'_l\}$  will be rejected if  $R \leq y$  and accepted if  $R > y$ . Here  $y$  is a random number from the interval  $[0, 1]$ . If the proposed change is rejected, we pick up again a random time slice and repeat the above process. If accepted,  $\{\phi'_l\}$  will be stored and replace  $\{\phi_l\}$  for the updating procedure.

To calculate  $R$ , note that  $S_{\{\phi_l\}}$  has a quadratic form. The fermionic degrees of freedom in Eq. (3.14) can hence be integrated out, giving

$$\mathcal{Z}_{\{\phi_l\}} = \prod_{\sigma} \det(\mathbf{g}^{\sigma}). \quad (3.20)$$

The probability ratio is then

$$R = e^{-K(\{\phi'_l\})+K(\{\phi_l\})} \prod_{\sigma} \det((\bar{\mathbf{g}}^{\sigma})^{-1} \mathbf{g}^{\sigma}), \quad (3.21)$$

where we have defined

$$\begin{aligned} \mathbf{g}_{mn}^{\sigma} &= -G_{mn}^{\sigma}(\{\phi_l\}), \\ \bar{\mathbf{g}}_{mn}^{\sigma} &= -G_{mn}^{\sigma}(\{\phi'_l\}). \end{aligned} \quad (3.22)$$

Eq. (3.21) can be simplified by using the updating equation [Hirsch & Fye 1986]

$$\bar{\mathbf{g}}^{\sigma} = \mathbf{g}^{\sigma} + (\mathbf{g}^{\sigma} - \mathcal{I}) \Delta^{\sigma} \bar{\mathbf{g}}^{\sigma}, \quad (3.23)$$

where  $\mathcal{I}$  is a  $L \times L$  unit matrix and

$$\begin{aligned} \Delta_{mn}^{\sigma} &= \left( e^{\bar{V}^{\sigma}} e^{-V^{\sigma}} - 1 \right)_{mn}, \\ V_{lm}^{\sigma} &= -g \Delta \tau \phi_l \delta_{lm}, \\ \bar{V}_{lm}^{\sigma} &= -g \Delta \tau \phi'_l \delta_{lm}. \end{aligned} \quad (3.24)$$

We have

$$R = e^{-K(\{\phi'_l\})+K(\{\phi_l\})} \prod_{\sigma} \det(\mathcal{I} + (\mathcal{I} - \mathbf{g}^{\sigma}) \Delta^{\sigma}), \quad (3.25)$$

which can be evaluated directly from  $\Delta^{\sigma}$  following the proposed change and the local Green's function  $\mathbf{g}^{\sigma}$  of the original configuration  $\{\phi_l\}$ . This saves some computational efforts since we do not need to evaluate the local Green's function for each proposed change even if the proposal is finally rejected.

For each local update at  $\tau_l$ ,  $\Delta^\sigma$  has only one nonzero element

$$\Delta_{mn}^\sigma = \Delta_0 \delta_{mn} \delta_{ml} = (e^{-g\Delta\tau(\phi'_l - \phi_l)} - 1) \delta_{mn} \delta_{ml}. \quad (3.26)$$

The updating equation can be simplified as

$$\bar{\mathbf{g}}_{mn}^\sigma = \mathbf{g}_{mn}^\sigma + \frac{(\mathbf{g}_{ml}^\sigma - \delta_{ml}) \Delta_0 \mathbf{g}_{ln}^\sigma}{1 + (1 - \mathbf{g}_{ll}^\sigma) \Delta_0}. \quad (3.27)$$

The probability ratio is now

$$R = e^{-K(\{\phi'_l\}) + K(\{\phi_l\})} \prod_{\sigma} (1 + (1 - \mathbf{g}_{ll}^\sigma) \Delta_0), \quad (3.28)$$

The evaluation of Eq. (3.27) costs most of the computational time, so the total computational time is proportional to  $L^3$  with a factor of  $L^2$  for Eq. (3.27) and a factor of  $L$  for a sweep of all the  $L$  time slices.

Moreover, a global update

$$\phi_l \longrightarrow \phi'_l = \phi_l + x \Delta \phi \quad l = 1, \dots, L \quad (3.29)$$

is performed after several local updates in order to improve the efficiency of the program. This global update can be treated as a sequential combination of the  $L$  local updates from  $\tau_1 = 0$  to  $\tau_L = \beta - \Delta\tau$ . At each  $\tau_l$  the Green's function  $\mathbf{g}_l^\sigma$  of the configuration  $\{\phi'_1, \dots, \phi'_l, \phi_{k+1}, \dots\}$  and the corresponding probability ratio  $R^l$  are calculated. The total probability ratio of the whole process is given by the product  $R = \prod_{l=1}^L R^l$ . The Metropolis algorithm is then applied to decide whether the global change is accepted. If accepted, the final configuration  $\{\phi'_l\}$  and the corresponding Green's function  $\mathbf{g}_L^\sigma$  will be stored for further updating procedures.

The above QMC simulations generate a "random walk" in the configuration space [Foulkes et al. 2001]. To avoid correlations between configurations in the set, we only collect one sample every several sweeps. A warm-up run is also performed in the beginning of the QMC simulations to get rid of the influence of the initial setup. The updating procedure continues until a set  $\mathcal{E}$  of a sufficient number of configurations is obtained. The expectation value of each physical quantity is then given by the averaging

$$\langle A \rangle = \frac{\sum_{\{\phi_l\} \in \mathcal{E}} A(\{\phi_l\})}{\sum_{\{\phi_l\} \in \mathcal{E}} 1}. \quad (3.30)$$

Especially important for our purposes is the on-site Green's function

$$G_{mn}^\sigma = \frac{\sum_{\{\phi_l\} \in \mathcal{E}} G_{mn}^\sigma(\{\phi_l\})}{\sum_{\{\phi_l\} \in \mathcal{E}} 1}. \quad (3.31)$$

Once we have the on-site Green's function, it can be used in the DMFT iterations until a convergent solution  $(\Sigma, G)$  is achieved.

The systematic error of the QMC calculations is about  $O(\Delta\tau^2)$ . To obtain good results,  $\Delta\tau$  should be as small as possible. It cannot be too small, however, since the computational time increases as  $\Delta\tau^{-3}$  for fixed  $\beta$ . One should do the extrapolation  $\Delta\tau \rightarrow 0$ , but in practice one often uses a small  $\Delta\tau$ . In this work we take  $\Delta\tau = 0.2$  so that we can reach the room temperature at about  $\beta = 30 - 40$ .

### 3.1.2 Hubbard model

For the one-band Hubbard model (3.8), the effective action in discretized form can be written as

$$S = - \sum_{\sigma; l, m=1}^L c_{l\sigma}^\dagger (\mathcal{G}_0^\sigma)^{-1} c_{m\sigma} + U\Delta\tau \sum_{l=1}^L n_{l\uparrow} n_{l\downarrow}, \quad (3.32)$$

where  $c_{m\sigma} = c_\sigma(\tau_m)$ . The partition function and the on-site Green's function are then

$$\begin{aligned} G_{mn}^\sigma &= -\frac{1}{\mathcal{Z}} \int [\mathcal{D}c^\dagger \mathcal{D}c] c_{m\sigma} c_{n\sigma}^\dagger e^{-S}, \\ \mathcal{Z} &= \int [\mathcal{D}c^\dagger \mathcal{D}c] e^{-S}, \end{aligned} \quad (3.33)$$

where  $[\mathcal{D}c^\dagger \mathcal{D}c]$  denotes the path integral over the Grassmann variables.

Because of the Coulomb interaction  $Un_\uparrow n_\downarrow$ , the path integral in Eq. (3.33) cannot be evaluated exactly. Neither can QMC sample the fermionic Grassmann variables  $\{c, c^\dagger\}$  in contrast to the bosonic phonon fields in the Holstein model. To proceed, we introduce the so-called (discrete) Hubbard-Stratonovich transformation [Hirsch 1983, Hirsch & Fye 1986],

$$e^{-U\Delta\tau n_\uparrow n_\downarrow + U\Delta\tau/2(n_\uparrow + n_\downarrow)} = \frac{1}{2} \sum_{s=\pm 1} e^{\lambda s(n_\uparrow - n_\downarrow)}, \quad (3.34)$$

with  $\lambda = \text{arccosh}(e^{U\Delta\tau/2})$ . The Coulomb interaction term can be decoupled so that

$$S_{\{s_l\}} = - \sum_{\sigma; l, m=1}^L c_{l\sigma}^\dagger (\mathcal{G}_0^\sigma)^{-1} c_{m\sigma} - \lambda \sum_{l=1}^L s_l (n_{l\uparrow} - n_{l\downarrow}), \quad (3.35)$$

where  $s_l = \pm 1$  is the Ising-like auxiliary field at  $\tau_l$ . The additional term  $U\Delta\tau(n_\uparrow + n_\downarrow)/2$  from the decomposition has been absorbed into the definition of  $\mathcal{G}_0^\sigma$  for sim-

plicity. We have

$$\begin{aligned} \mathcal{Z} &= \sum_{\{s_l\}} \mathcal{Z}_{\{s_l\}}, \\ G_{mn}^\sigma &= \sum_{\{s_l\}} \frac{\mathcal{Z}_{\{s_l\}}}{\mathcal{Z}} G_{mn}^\sigma(\{s_l\}), \end{aligned} \quad (3.36)$$

where

$$\begin{aligned} \mathcal{Z}_{\{s_l\}} &= \int [\mathcal{D}c^\dagger \mathcal{D}c] e^{-S_{\{s_l\}}}, \\ G_{mn}^\sigma(\{s_l\}) &= -\frac{1}{\mathcal{Z}_{\{s_l\}}} \int [\mathcal{D}c^\dagger \mathcal{D}c] c_{m\sigma} c_{n\sigma}^\dagger e^{-S_{\{s_l\}}}. \end{aligned} \quad (3.37)$$

Now  $\mathcal{Z}_{\{s_l\}}$  can be calculated exactly and the full partition function can be obtained by summing over all the auxiliary fields  $\{s_l\}$ , which can be done by QMC simulations as shown in Fig. 3.2. Again for each local update at  $\tau_l$ , we have the updating equation

$$\bar{\mathbf{g}}_{mn}^\sigma = \mathbf{g}_{mn}^\sigma + \frac{(\mathbf{g}_{ml}^\sigma - \delta_{ml}) \Delta_0 \mathbf{g}_{ln}^\sigma}{1 + (1 - \mathbf{g}_{ll}^\sigma) \Delta_0}, \quad (3.38)$$

with

$$\begin{aligned} V_{lm}^\sigma &= -\lambda s_l \sigma \delta_{lm}, \\ \Delta_0^\sigma &= e^{-\lambda(s'_l - s_l)\sigma} - 1, \end{aligned} \quad (3.39)$$

where  $s'_l$  ( $s_l$ ) is the auxiliary field in the new (old) configuration. The probability ratio is given by

$$R = \prod_{\sigma} (1 + (1 - \mathbf{g}_{ll}^\sigma) \Delta_0). \quad (3.40)$$

Numerically, we start from a random configuration  $\{s_l^0\}$ . The Green's function of this configuration can be calculated from the Weiss effective field  $\mathcal{G}_0^\sigma$  (corresponding to  $\{s_l = 0\}$ ) by using the updating equation (3.38) sequentially from  $\tau_1$  to  $\tau_L$ . For local updates, we pick up randomly a time slice  $\tau_l$  and try  $s_l \rightarrow -s_l$ . The probability ratio is given by Eq. (3.40). We then apply the Metropolis algorithm to this local update. As before, the whole QMC procedure follows the same steps as shown in Fig. 3.2. Global updates are not considered for the Ising-like auxiliary fields.

### 3.1.3 Realistic microscopic model

We can extend the above discussions to the realistic microscopic model (2.20). The partition function and the on-site Green's function are

$$\begin{aligned} G_{mn}^{\mu\nu;\sigma} &= -\frac{1}{\mathcal{Z}} \int [\mathcal{D}\mathbf{S}\mathcal{D}c^\dagger\mathcal{D}c\mathcal{D}Q_2\mathcal{D}Q_3] c_{m\mu\sigma} c_{n\nu\sigma}^\dagger e^{-S}, \\ \mathcal{Z} &= \int [\mathcal{D}\mathbf{S}\mathcal{D}c^\dagger\mathcal{D}c\mathcal{D}Q_2\mathcal{D}Q_3] e^{-S}, \end{aligned} \quad (3.41)$$

which contain the path integral over both fermionic and bosonic degrees of freedom, as well as the integral over the  $t_{2g}$  spin  $\mathbf{S}$  which is assumed to be classical and independent of the imaginary time variable  $\tau$ . Due to spin-rotational symmetry, the integral over the orientation of  $\mathbf{S}$  can be replaced by the sum over two opposite orientations  $\mathbf{S}^z = \pm|\mathbf{S}|$  [Held 1999], giving

$$\begin{aligned} G_{mn}^{\mu\nu;\sigma} &= -\frac{1}{2} \sum_{\mathbf{S}^z=\pm|\mathbf{S}|} \frac{1}{\mathcal{Z}'} \int [\mathcal{D}c^\dagger\mathcal{D}c\mathcal{D}Q_2\mathcal{D}Q_3] c_{\mu m\sigma} c_{\nu n\sigma}^\dagger e^{-S}, \\ \mathcal{Z}' &= \frac{1}{2} \sum_{\mathbf{S}^z=\pm|\mathbf{S}|} \int [\mathcal{D}c^\dagger\mathcal{D}c\mathcal{D}Q_2\mathcal{D}Q_3] e^{-S} \\ &= \int_{\mathbf{S}^z=|\mathbf{S}| \text{ or } -|\mathbf{S}|} [\mathcal{D}c^\dagger\mathcal{D}c\mathcal{D}Q_2\mathcal{D}Q_3] e^{-S} = \frac{\mathcal{Z}}{4\pi}, \end{aligned} \quad (3.42)$$

so we only need to take care of the path integral of the fermionic and bosonic degrees of freedom. For the paramagnetic phase, we do the calculations for a single  $t_{2g}$  spin orientation such as  $\mathbf{S}^z = +|\mathbf{S}|$  and then average over spin indices. For the ferromagnetic phase, we assume full spin polarization.

By using the Hubbard-Stratonovich transformation, we have to introduce six Ising-like auxiliary fields in order to decouple the intra- and inter-orbital Coulomb interactions in Eq. (2.20). These discrete fields will be sampled together with the two Jahn-Teller fields. We define (set  $\mathbf{S}^z = +|\mathbf{S}|$ )

$$\begin{aligned} \mathcal{Z}_{\{s^l; Q^l\}} &= \int [\mathcal{D}c^\dagger\mathcal{D}c] e^{-S_{\{s^l; Q^l\}}}, \\ G_{mn}^{\mu\nu;\sigma}(\{s^l; Q^l\}) &= -\frac{1}{\mathcal{Z}_{\{s^l; Q^l\}}} \int [\mathcal{D}c^\dagger\mathcal{D}c] c_{m\sigma} c_{n\sigma}^\dagger e^{-S_{\{s^l; Q^l\}}}, \end{aligned} \quad (3.43)$$

so that

$$\begin{aligned} \mathcal{Z} &= \sum_{\{s^l; Q^l\}} \mathcal{Z}_{\{s^l; Q^l\}}, \\ G_{mn}^{\mu\nu;\sigma} &= \sum_{\{s^l; Q^l\}} \frac{\mathcal{Z}_{\{s^l; Q^l\}}}{\mathcal{Z}} G_{mn}^{\mu\nu;\sigma}(\{s^l; Q^l\}), \end{aligned} \quad (3.44)$$

in which  $\{s^l; Q^l\}$  denotes the field configuration.

The effective action in the above equations can be easily written as

$$S(\{s^l; Q^l\}) = S_0 + K_Q + S_J + S_Q + S_U, \quad (3.45)$$

with

$$\begin{aligned} S_0 &= - \sum_{lm; \mu\nu\sigma} c_{l\mu\sigma}^\dagger (\mathcal{G}_0^\sigma)^{-1}_{lm; \mu\nu} c_{m\nu\sigma}, \\ K_Q &= \frac{\Delta\tau}{2} \sum_{l;a} \left[ \left( \frac{Q_a^{l+1} - Q_a^l}{\Delta\tau} \right)^2 + \Omega^2 (Q^l)^2 \right], \\ S_J &= -J|\mathbf{S}|\Delta\tau \sum_{l;\mu} (n_{l\mu\uparrow} - n_{l\mu\downarrow}) \\ S_Q &= -g\Delta\tau \sum_{l; \mu\nu\sigma} c_{l\mu\sigma}^\dagger (Q_2^l \tau^x + Q_3^l \tau^z)_{\mu\nu} c_{l\nu\sigma}, \\ S_U &= - \sum_l [\lambda_U s_U^l (n_{l1\uparrow} - n_{l1\downarrow}) + \lambda_U \tilde{s}_U^l (n_{l2\uparrow} - n_{l2\downarrow})] \\ &\quad - \sum_{l;\sigma} [\lambda_V s_V^{l\sigma} (n_{l1\sigma} - n_{l2\bar{\sigma}}) + \lambda_{V-F} s_{V-F}^{l\sigma} (n_{l1\sigma} - n_{l2\sigma})]. \end{aligned} \quad (3.46)$$

Here  $Q_a^l \equiv Q_a(\tau_l)$ ,  $c_{m\nu\sigma} \equiv c_{\nu\sigma}(\tau_m)$ , and  $\lambda_x = \text{arccosh}(e^{x\Delta\tau/2})$ .  $\{s_U^l, (\tilde{s}_U^l), s_V^{l\sigma}, s_{V-F}^{l\sigma}\}$  are the Ising-like auxiliary fields for  $\{U n_{m\uparrow} n_{m\downarrow}, V n_{1\sigma} n_{2\bar{\sigma}}, (V-F) n_{1\sigma} n_{2\sigma}\}$ , respectively.

The effective action  $S$  is spin-diagonal but has off-diagonal elements between  $e_g$  orbitals. As before, we have to introduce a  $2 \times 2$  matrix at each time slice  $\tau_l$ :

$$V^{l\sigma} = V_Q^{l\sigma} + V_s^{l\sigma}, \quad (3.47)$$

where

$$V_Q^{l\sigma} = - \begin{pmatrix} g\Delta\tau Q_3^l & g\Delta\tau Q_2^l \\ g\Delta\tau Q_2^l & -g\Delta\tau Q_3^l \end{pmatrix} \quad (3.48)$$

is from the phonon contribution  $S_Q$  and

$$V_s^{l\sigma} = - \begin{pmatrix} \lambda_U s_U^l \sigma + \lambda_V s_V^{l\sigma} + \lambda_{V-F} s_{V-F}^{l\sigma} & 0 \\ 0 & \lambda_U \tilde{s}_U^l \sigma - \lambda_V s_V^{l\bar{\sigma}} - \lambda_{V-F} s_{V-F}^{l\sigma} \end{pmatrix} \quad (3.49)$$

from the Coulomb contribution  $S_U$ . The updating equation for a local update at  $\tau_l$  is then (in matrix form)

$$\bar{\mathbf{g}}_{mn}^\sigma = \mathbf{g}_{mn}^\sigma + (\mathbf{g}_{ml}^\sigma - \delta_{ml}) \Delta_0 [1 + (1 - \mathbf{g}_{ll}^\sigma) \Delta_0]^{-1} \mathbf{g}_{ln}^\sigma, \quad (3.50)$$

with

$$\begin{aligned}
 \Delta_0^\sigma &= e^{\bar{V}^\sigma} e^{-V^\sigma} - 1, \\
 \mathbf{g}_{mn}^{\mu\nu;\sigma} &= -G_{mn}^{\mu\nu;\sigma}(\{s^{l\sigma}; Q^l\}), \\
 \bar{\mathbf{g}}_{mn}^{\mu\nu;\sigma} &= -G_{mn}^{\mu\nu;\sigma}(\{\bar{s}^{l\sigma}; \bar{Q}^l\}).
 \end{aligned} \tag{3.51}$$

This gives the probability ratio

$$R = e^{-K\bar{Q}+KQ} \prod_{\sigma} \det(1 + (1 - \mathbf{g}_{il}^\sigma)\Delta_0), \tag{3.52}$$

in which the determinant is over the orbital indices. In the QMC simulations, each proposed change includes a shift of all the boson fields and a flip of one random Ising-like auxiliary spin. A global update of the boson fields is also performed every several local updates. Once again, the whole QMC procedure follows the same steps as shown in Fig. 3.2.

## 3.2 Maximum entropy method

The Green's function obtained by DMFT (QMC) is in imaginary time. To extract real frequency informations and compare them with experiments, we need to calculate the electron spectral function  $A(\omega) = -\text{Im}G(\omega)/\pi$  which is related to the Green's function  $G(\tau)$  by

$$G(\tau) = \int_{-\infty}^{\infty} d\omega \frac{e^{-\omega\tau}}{1 + e^{-\beta\omega}} A(\omega), \tag{3.53}$$

or in discrete form

$$G(\tau_i) = \sum_{k=-N}^N \Delta\omega \frac{e^{-\tau_i\omega_k}}{1 + e^{-\beta\omega_k}} A(\omega_k), \tag{3.54}$$

where we have defined  $\omega_k = k\Delta\omega$ ,  $k = -N, \dots, N$  in the range of  $[-N\Delta\omega, N\Delta\omega]$ .  $N$  has to be large enough so that the spectral weight out of the above range is negligible. Eq. (3.54) is a linear equation. However, a direct inversion of Eq. (3.54) cannot produce good results, especially at large frequencies, because of the exponential nature of the kernel  $e^{-\omega\tau}/(1+e^{-\beta\omega})$  and the incomplete information from the discrete DMFT (QMC) data points.

In this work we use the maximum entropy method (MEM) in which  $A(\omega_k)$  is treated as unknown quantities to be subtracted from the probability distribution of the DMFT data  $\{\langle G(\tau_i) \rangle, \Delta G(\tau_i)\}$  [Jarrell & Gubernatis 1996].  $\Delta G(\tau_i)$  denotes the systematic error or statistical fluctuation of  $G(\tau_i)$ . We are going to find a

probability function  $P(A|\langle G \rangle)$  which gives the most probable  $A(\omega_k)$  consistent with the DMFT data  $\{\langle G(\tau_i) \rangle, \Delta G(\tau_i)\}$ . Here  $P(a|b)$  is the conditional probability of  $a$  given  $b$ .

In DMFT (QMC),  $\Delta G(\tau_i)$  can be obtained by additional iterations (called measurements) after a self-consistent set of  $(\Sigma, G)$  is reached. The number of sweeps in each measurement is kept relative small so that the statistical fluctuations of the QMC data can be calculated by analyzing the the numerical data of different measurements. We have

$$\Delta G(\tau_i) = \sqrt{\frac{\langle G(\tau_i)^2 \rangle - \langle G(\tau_i) \rangle^2}{M-1}}, \quad (3.55)$$

where we assume  $M$  measurements and  $\langle \cdot \rangle$  means the average of all measurements.

We assume that correlations between  $G(\tau_i)$  at different time slices can be neglected, so that the distribution of each  $G(\tau_i)$  approaches a Gaussian in the limit of large  $M$  according to the central limit theorem:

$$P(G(\tau_i)) = \frac{1}{\sqrt{2\pi\Delta G(\tau_i)}} e^{-\chi_i^2/2}, \quad (3.56)$$

where

$$\chi_i^2 = \left( \frac{\langle G(\tau_i) \rangle - G(\tau_i)}{\Delta G(\tau_i)} \right)^2. \quad (3.57)$$

For every  $A(\omega_k)$  the corresponding  $G(\tau_i)$  can be evaluated from Eq. (3.54), giving

$$P(\langle G \rangle | A) \propto e^{-\chi^2/2} \quad (3.58)$$

where  $\chi^2 = \sum_{i=1}^L \chi_i^2$ .  $P(\langle G \rangle | A)$  is called the likelihood function and represents the probability that this  $A(\omega_k)$  yields  $\langle G(\tau_i) \rangle$  within the DMFT (QMC) error  $\Delta G(\tau_i)$ . It is related to  $P(A|\langle G \rangle)$  by the Bayes' theorem

$$P(A|\langle G \rangle) = P(\langle G \rangle | A)P(A)/P(\langle G \rangle), \quad (3.59)$$

where  $P(A)$  is the prior probability of  $A(\omega_k)$  and  $P(\langle G \rangle)$  is a constant.

It can be shown that the prior probability of unnormalized  $A(\omega_k)$  is determined by the entropy [Skilling 1989]

$$S = \sum_{k=-N}^N \Delta\omega \left( A(\omega_k) - m(\omega_k) - A(\omega_k) \ln \left( \frac{A(\omega_k)}{m(\omega_k)} \right) \right), \quad (3.60)$$

where  $m(\omega_k)$  is a positive-definite function and usually taken as uniform. Defining the entropic prior

$$P(A|\alpha) \propto e^{\alpha S}, \quad (3.61)$$



we have

$$P(A) = P(A|\alpha)P(\alpha). \quad (3.62)$$

For each  $\alpha$ ,  $P(A|\alpha)$  has its maxima at  $A(\omega_k) = m(\omega_k)$ , so  $m(\omega_k)$  is called the default model. If  $\alpha$  is known, the probability of the spectral density  $A(\omega_k)$  given the DMFT data  $\{\langle G(\tau_i) \rangle, \Delta G(\tau_i)\}$  is

$$P(A|\langle G \rangle, \alpha) \propto e^{\alpha S - \chi^2/2}, \quad (3.63)$$

which can be maximized to give the optimal  $A(\omega_k)$ . The selection of  $\alpha$  (or  $P(\alpha)$ ) leads to different methods such as the classic MEM [Gull 1989], the historic MEM [Gull & Daniell 1978, Skilling & Bryan 1984], and the Bryan's method [Bryan 1990]. A brief introduction to these different methods can be found in the review article [Jarrell & Gubernatis 1996]. A maximum entropy program released by A. Sandvik is used in this work.

### 3.3 Static spin susceptibility

One of the most important quantity in doped manganites is the Curie temperature  $T_c$ . Above  $T_c$ , the static spin susceptibility  $\chi(T)$  in the paramagnetic phase has the asymptotic behavior

$$\chi(T)^{-1} \sim T - T_c, \quad T \rightarrow T_c. \quad (3.64)$$

If  $\chi(T)$  is known, the Curie temperature can be easily obtained.

Physically, the spin susceptibility measures the magnetic response of the system to the perturbation of an external magnetic field. In the linear response theory, this leads to the formula

$$\chi(\mathbf{k}, i\omega_n)_{ab} = \int_0^\beta d\tau e^{i\omega_n \tau} \sum_j e^{i\mathbf{k} \cdot \mathbf{r}_j} \langle T \mathbf{s}^z(\mathbf{r}_j, \tau) \mathbf{s}^z(\mathbf{0}, 0) \rangle, \quad (3.65)$$

where  $\mathbf{s}^z$  is the  $z$ -component of the spin operator of the conduction electrons. In the limit of infinite dimensions, the formula can be much simplified. Detailed discussions can be found in Ref. [Georges et al. 1996]. Here we follow the derivation in [Held 1999] and extend it to multi-orbital systems. The method is specially designed for calculating the static spin susceptibility in DMFT.

Note that a small magnetic field  $x$  shifts the dispersion of the conduction electrons as

$$\epsilon_{\mu\sigma\mathbf{k}}^x = \epsilon_{\mu\sigma\mathbf{k}} - x f_{\mu\sigma}^x, \quad (3.66)$$

where  $f_{\mu\sigma}^x$  ( $= \sigma$ ) is introduced for the sake of generality. This results in a small change of the electron occupation number so that we can calculate the static spin susceptibility directly by

$$\begin{aligned}\chi(T) &= \frac{1}{2} \sum_{\mu\sigma} f_{\mu\sigma}^x \frac{\partial n_{\mu\sigma}(T)}{\partial x} \\ &= \frac{1}{2} \sum_{\mu\sigma} f_{\mu\sigma}^x \frac{\partial G^{\mu\sigma}(\tau=0)}{\partial x} \\ &= \frac{1}{2\beta} \sum_{n\mu\sigma} f_{\mu\sigma}^x \frac{\partial G^{\mu\sigma}(i\omega_n)}{\partial x}.\end{aligned}\quad (3.67)$$

The external field  $x$  can be absorbed into the definition of  $\mathcal{G}_0^{\mu\sigma}$  in the impurity effective action (3.8), so that the derivative of the functional equation for the local Green's equation yields

$$\frac{\partial G^{\mu\sigma}(\tau_l)}{\partial x} = \sum_{m;\nu\sigma'} Y_{\tau_m;\nu\sigma'}^{\tau_l;\mu\sigma} \gamma_{\tau_m}^{\nu\sigma'}, \quad (3.68)$$

where

$$\begin{aligned}Y_{\tau_m;\nu\sigma'}^{\tau_l;\mu\sigma} &= \frac{1}{L} \sum_{nk} \Gamma_{\tau_k, \tau_m + \tau_k; \nu\sigma'}^{\tau_l + \tau_n, \tau_n; \mu\sigma}, \\ \Gamma_{\tau_m \tau_n; \nu\sigma'}^{\tau_l \tau_k; \mu\sigma} &= -\langle \mathcal{T} c_{l\mu\sigma} c_{k\mu\sigma}^\dagger c_{m\nu\sigma'}^\dagger c_{n\nu\sigma'} \rangle + \langle \mathcal{T} c_{l\mu\sigma} c_{k\mu\sigma}^\dagger \rangle \langle \mathcal{T} c_{m\nu\sigma'}^\dagger c_{n\nu\sigma'} \rangle\end{aligned}\quad (3.69)$$

and

$$\gamma_{\tau_l}^{\mu\sigma} = \frac{\partial (\mathcal{G}_0^{\mu\sigma})_{\tau_l, 0}^{-1}}{\partial x} \Big|_{x=0}. \quad (3.70)$$

The Weiss effective field  $\mathcal{G}_0^{\mu\sigma}$ , as well as the interacting Green's function  $G^{\mu\sigma}$  and the local self-energy  $\Sigma^{\mu\sigma}$ , have no spin and orbital off-diagonal elements because of the spin and orbital rotational symmetry. The second term in  $\Gamma_{\tau_m \tau_n; \nu\sigma'}^{\tau_l \tau_k; \mu\sigma}$  stems from the partition function and can be evaluated directly. To calculate the first term, we have to use the decomposition

$$\begin{aligned}-\langle \mathcal{T} c_{l\mu\sigma} c_{k\mu\sigma}^\dagger c_{m\nu\sigma'}^\dagger c_{n\nu\sigma'} \rangle &= \sum_{\{s^l; Q^l\}} \frac{\mathcal{Z}_{\{s^l; Q^l\}}}{\mathcal{Z}} \times \left[ G_{lk}^{\mu\mu; \sigma}(\{s_l, Q_l\}) G_{nm}^{\nu\nu; \sigma'}(\{s_l, Q_l\}) \right. \\ &\quad \left. - \delta_{\sigma\sigma'} G_{lm}^{\mu\nu; \sigma}(\{s_l, Q_l\}) G_{nk}^{\nu\mu; \sigma}(\{s_l, Q_l\}) \right],\end{aligned}\quad (3.71)$$

which is possible since we deal with independent electrons after the Hubbard-Stratonovich transformation.

The calculation of  $\gamma_n^{\mu\sigma}$  is more complicated and require the DMFT self-consistent equations. First, by using

$$G^{\mu\sigma}(i\omega_n) = \frac{1}{\mathcal{V}} \sum_{\mathbf{k}} [i\omega_n + \mu - \epsilon_{\mathbf{k}} + f_{\sigma}^x x - \Sigma^{\sigma}(i\omega_n)]_{\mu\mu}^{-1}, \quad (3.72)$$

we have

$$\frac{\partial G^{\mu\sigma}(i\omega_n)}{\partial x} \Big|_{x=0} = -\frac{1}{\mathcal{V}} \sum_{\mathbf{k};\nu} A_{\mu\nu}^{\sigma}(\mathbf{k}, i\omega_n) \left( f_{\nu\sigma}^x - \frac{\partial \Sigma^{\nu\sigma}(i\omega_n)}{\partial x} \right) A_{\nu\mu}^{\sigma}(\mathbf{k}, i\omega_n), \quad (3.73)$$

where the spectral function  $A_{\mu\nu}^{\sigma}(\mathbf{k}, i\omega_n)$  is defined as

$$A_{\mu\nu}^{\sigma}(\mathbf{k}, i\omega_n) = [i\omega_n + \mu - \epsilon_{\mathbf{k}} - \Sigma^{\sigma}(i\omega_n)]_{\mu\nu}^{-1}. \quad (3.74)$$

On the other hand, the self-energy and the local Green's function are also related by the Dyson equation (3.9) so that

$$\frac{\partial \Sigma^{\mu\sigma}(i\omega_n)}{\partial x} = \gamma^{\mu\sigma}(i\omega_n) + G^{\mu\sigma}(i\omega_n)^{-2} \frac{\partial G^{\mu\sigma}(i\omega_n)}{\partial x}, \quad (3.75)$$

where

$$\gamma^{\mu\sigma}(i\omega_n) = \frac{\partial \mathcal{G}_0^{\mu\sigma}(i\omega_n)^{-1}}{\partial x} \Big|_{x=0} = \frac{1}{\Delta\tau} \sum_l \gamma_n^{\mu\sigma} e^{i\omega_n \tau_l}. \quad (3.76)$$

Combining Eqs. (3.73) and (3.75) gives

$$\frac{\partial G^{\mu\sigma}(i\omega_n)}{\partial x} = \sum_{\nu} R_{\mu\nu}^{\sigma}(i\omega_n) (f_{\nu\sigma}^x - \gamma^{\nu\sigma}(i\omega_n)), \quad (3.77)$$

with

$$\begin{aligned} R^{\sigma}(i\omega_n) &= -\frac{D^{\sigma}(i\omega_n)T^{\sigma}(i\omega_n)}{\det D^{\sigma}(i\omega_n)}, \\ D^{\sigma}(i\omega_n) &= \begin{pmatrix} 1 - (G^{2\sigma}(i\omega_n))^{-2}T_{22}^{\sigma}(i\omega_n) & (G^{2\sigma}(i\omega_n))^{-2}T_{12}^{\sigma}(i\omega_n) \\ (G^{1\sigma}(i\omega_n))^{-2}T_{21}^{\sigma}(i\omega_n) & 1 - (G^{1\sigma}(i\omega_n))^{-2}T_{11}^{\sigma}(i\omega_n) \end{pmatrix}, \\ T^{\sigma}(i\omega_n) &= \frac{1}{\mathcal{V}} \sum_{\mathbf{k}} \begin{pmatrix} A_{11}^{\sigma}(\mathbf{k}, i\omega_n)A_{11}^{\sigma}(\mathbf{k}, i\omega_n) & A_{12}^{\sigma}(\mathbf{k}, i\omega_n)A_{21}^{\sigma}(\mathbf{k}, i\omega_n) \\ A_{21}^{\sigma}(\mathbf{k}, i\omega_n)A_{12}^{\sigma}(\mathbf{k}, i\omega_n) & A_{22}^{\sigma}(\mathbf{k}, i\omega_n)A_{22}^{\sigma}(\mathbf{k}, i\omega_n) \end{pmatrix}. \end{aligned} \quad (3.78)$$

Note that Eqs. (3.68) and (3.77) are related by the Fourier transform

$$\begin{aligned} \frac{\partial G^{\mu\sigma}(\tau)}{\partial x} &= \frac{1}{\beta} \sum_n \frac{\partial G^{\mu\sigma}(i\omega_n)}{\partial x} e^{-i\omega_n \tau}, \\ R^{\sigma}(\tau) &= \frac{1}{\beta} \sum_n R^{\sigma}(i\omega_n) e^{-i\omega_n \tau}. \end{aligned} \quad (3.79)$$

We arrive at the final result

$$\sum_{m;\nu\sigma'} \left[ Y_{\tau_m;\nu\sigma'}^{\tau_l;\mu\sigma} + \delta_{\sigma\sigma'} \frac{R_{\mu\nu}^\sigma(\tau_l - \tau_m)}{\Delta\tau} \right] \gamma_{\tau_m}^{\nu\sigma} = \sum_{\nu} R_{\mu\nu}^\sigma(\tau_l) f_{\nu\sigma}^x, \quad (3.80)$$

which is a linear equation and can be inverted to give  $\gamma_{\tau_l}^{\mu\sigma}$ . The static spin susceptibility and hence the Curie temperature follow immediately from Eqs. (3.67) and (3.68). The above method can be applied to other cases, e.g., the orbital susceptibility.

### 3.4 Optical conductivity

In the last decade, the optical properties of manganites have been studied intensively and provide very rich information for our understanding [Okimoto et al. 1995, Jung et al. 1998, Takenaka et al. 1999, Tobe et al. 2004]. In order to compare directly with experimental observations, we derive the formula for the optical conductivity in this section. An extensive investigation on this subject can be found in the thesis [Blümer 2003].

The optical conductivity measures the response of the system to an external electric field. It is defined as

$$\mathbf{j}_\alpha(\omega) = \sigma_{\alpha\beta}(\omega) \mathbf{E}_\beta, \quad (3.81)$$

Where  $\mathbf{E}_0 e^{-i\omega t}$  is the external electric field and  $\mathbf{j}(\omega) e^{-i\omega t}$  the corresponding electric current. In the linear response theory, the Kubo formula gives [Mahan 2000]

$$\sigma_{\alpha\beta}(\omega) = \frac{i\mathcal{V}}{\omega + i0^+} \langle \langle j_\alpha, j_\beta \rangle \rangle_\omega - \frac{ie^2 a^2}{\mathcal{V} \hbar^2 (\omega + i0^+)} \langle \hat{K}_\alpha^0 \rangle \delta_{\alpha\beta}, \quad (3.82)$$

where  $a, \mathcal{V}$  are the lattice parameter and the volume of the cubic unit cell, respectively.  $j_\alpha$  denotes the  $\alpha$ -component of the current operator and  $K_\alpha^0$  is the  $\alpha$ -component of the kinetic energy

$$K^0 = - \sum_{\langle ij \rangle; \mu\nu\sigma} t_{\mu\nu}^{ij} (c_{i\mu\sigma}^\dagger c_{j\nu\sigma} + c_{j\mu\sigma}^\dagger c_{i\nu\sigma}). \quad (3.83)$$

The two terms in Eq. (3.82) correspond to the paramagnetic and diamagnetic contributions, respectively. In the following, we consider only the (regular) paramagnetic term. The diamagnetic term will be canceled by the singular part of the paramagnetic contributions.

The form of the current operator on a lattice can be obtained by the gauge transformation

$$\psi(\mathbf{r}) \longrightarrow \tilde{\psi}(\mathbf{r}) = e^{\frac{ie}{\hbar} \int_{\mathbf{r}_0}^{\mathbf{r}} \mathbf{dr}' \cdot \mathbf{A}(\mathbf{r}', t)} \psi(\mathbf{r}). \quad (3.84)$$

The vector potential of the external field

$$\mathbf{A}(\mathbf{r}, t) = \mathbf{E}_0 e^{-i\omega t} / i\omega \quad (3.85)$$

is then absorbed into the hopping integral

$$t_{\mu\nu}^{ij} \longrightarrow \tilde{t}_{\mu\nu}^{ij} = t_{\mu\nu}^{ij} e^{\frac{ie}{\hbar} \int_{\mathbf{r}_j}^{\mathbf{r}_i} d\mathbf{r}' \cdot \mathbf{A}(\mathbf{r}', t)}. \quad (3.86)$$

Expanding the kinetic energy to first order in  $\mathbf{A}(\mathbf{r}, t)$  yields

$$\tilde{K}^0 = K^0 + \frac{ie}{\hbar} \sum_{\langle ij \rangle; \mu\nu\sigma} \mathbf{R}_{ij} \cdot \mathbf{A} t_{\mu\nu}^{ij} (c_{i\mu\sigma}^\dagger c_{j\nu\sigma} - c_{j\mu\sigma}^\dagger c_{i\nu\sigma}), \quad (3.87)$$

with  $\mathbf{R}_{ij} = \mathbf{r}_i - \mathbf{r}_j$ . Remembering that the vector potential couples to the current operator as  $-\mathbf{j} \cdot \mathbf{A}$ , we have

$$\begin{aligned} \mathbf{j}_\alpha &= -\frac{ie}{\hbar} \sum_{\langle ij \rangle; \mu\nu\sigma} \mathbf{R}_{ij}^\alpha t_{\mu\nu}^{ij} (c_{i\mu\sigma}^\dagger c_{j\nu\sigma} - c_{j\mu\sigma}^\dagger c_{i\nu\sigma}) \\ &= \frac{e}{\hbar\mathcal{V}} \sum_{\mathbf{k}; \mu\nu\sigma} \frac{\partial \epsilon_{\mathbf{k}}^{\mu\nu}}{\partial \mathbf{k}_\alpha} c_{\mathbf{k}\mu\sigma}^\dagger c_{\mathbf{k}\nu\sigma}, \end{aligned} \quad (3.88)$$

where we have used the Fourier transform

$$c_{\mathbf{k}\mu\sigma} = \frac{1}{N} \sum_{i=1}^N e^{i\mathbf{r}_i \cdot \mathbf{k}} c_{i\mu\sigma}. \quad (3.89)$$

The optical conductivity is then

$$\sigma_{\alpha\beta}(\omega) = \frac{ie^2}{\hbar^2 \mathcal{V}(\omega + i0^+)} \sum_{\mu_1 \mu_2 \nu_1 \nu_2} \sum_{\mathbf{k}_1 \mathbf{k}_2 \sigma_1 \sigma_2} \mathbf{v}_{\mathbf{k}_1 \alpha}^{\mu_1 \nu_1} \mathbf{v}_{\mathbf{k}_2 \beta}^{\mu_2 \nu_2} \langle \langle c_{\mathbf{k}_1 \mu_1 \sigma_1}^\dagger c_{\mathbf{k}_1 \nu_1 \sigma_1}; c_{\mathbf{k}_2 \mu_2 \sigma_2}^\dagger c_{\mathbf{k}_2 \nu_2 \sigma_2} \rangle \rangle_\omega, \quad (3.90)$$

where  $\mathbf{v}_{\mathbf{k}\alpha}^{\mu\nu} \equiv \partial \epsilon_{\mathbf{k}}^{\mu\nu} / \partial \mathbf{k}_\alpha$  and  $\langle \langle A; B \rangle \rangle_\omega$  is the Fourier transform of the correlation function  $\langle \mathcal{T}(A(t)B(0)) \rangle$ .

Fig. 3.3 shows the Feynman diagrams for the optical conductivity. In the limit of infinite dimensions, the particle-hole irreducible vertex is local and independent of  $\mathbf{k}_{1(2)}$ . So the contributions of all higher order diagrams with vertex corrections disappear after summing over  $\mathbf{k}_1$  ( $\mathbf{k}_2$ ) since the velocity  $\mathbf{v}_{\mathbf{k}\alpha}^{\mu\nu} = -\mathbf{v}_{-\mathbf{k}\alpha}^{\mu\nu}$ . The only nonzero term comes from the bubble diagram [Pruschke et al. 1993a], giving (in Matsubara frequency)

$$\sigma_{\alpha\beta}(i\xi_m) = \frac{e^2}{\hbar^2 \mathcal{V} \xi_m \beta} \sum_{\mu_1 \mu_2 \nu_1 \nu_2} \sum_{n \mathbf{k}\sigma} \mathbf{v}_{\mathbf{k}\alpha}^{\mu_1 \nu_1} \mathbf{v}_{\mathbf{k}\beta}^{\mu_2 \nu_2} G_{\mathbf{k}\sigma}^{\nu_1 \mu_2}(i\omega_n) G_{\mathbf{k}\sigma}^{\nu_2 \mu_1}(i\omega_n + i\xi_m), \quad (3.91)$$

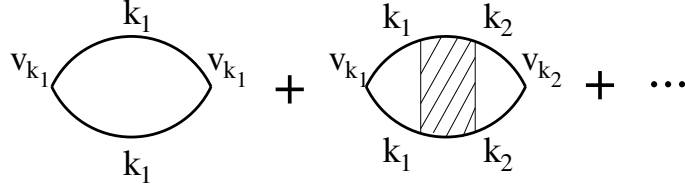


Figure 3.3: Feynman diagrams for the optical conductivity. In DMFT, all the higher order diagrams with vertex corrections disappear after summing over  $\mathbf{k}_{1(2)}$ . Only the first diagram, the bubble diagram, gives a nonzero contribution to the optical conductivity.

where  $\xi_m = 2\pi m/\beta$  is a bosonic Matsubara frequency. Using the spectral representation

$$G_{\mathbf{k}\sigma}^{\mu\nu}(i\omega_n) = \int_{-\infty}^{\infty} d\omega \frac{A_{\mathbf{k}\sigma}^{\mu\nu}(\omega)}{i\omega_n - \omega}, \quad (3.92)$$

the sum over the fermionic Matsubara frequency  $\omega_n$  can be evaluated by the contour integral technique, giving

$$\frac{1}{\hbar\beta} \sum_{n=-\infty}^{\infty} \frac{1}{(i\omega_n - \omega_1)(i\omega_n + i\xi_m - \omega_2)} = \frac{f(\omega_1) - f(\omega_2)}{\omega_1 - \omega_2 + i\xi_m}, \quad (3.93)$$

where  $f(\omega)$  is the Fermi distribution function. We obtain

$$\sigma_{\alpha\beta}(i\xi_m) = \frac{e^2}{\hbar\mathcal{V}\xi_m} \sum_{\mathbf{k}\sigma} \int \int d\omega_1 d\omega_2 \frac{f(\omega_1) - f(\omega_2)}{\omega_1 - \omega_2 + i\xi_m} \text{Tr} [\mathbf{v}_{\mathbf{k}\alpha} A_{\mathbf{k}\sigma}(\omega_1) \mathbf{v}_{\mathbf{k}\beta} A_{\mathbf{k}\sigma}(\omega_2)], \quad (3.94)$$

where  $\text{Tr}[\dots]$  denotes trace over orbitals and the formula is written in the matrix form. Back to real frequencies, we find

$$\text{Re}\sigma_{\alpha\beta}(\omega) = \frac{\pi e^2}{\hbar\mathcal{V}} \sum_{\mathbf{k}\sigma} \int d\omega_1 \frac{f(\omega_1) - f(\omega_1 + \omega)}{\omega} \text{Tr} [\mathbf{v}_{\mathbf{k}\alpha} A_{\mathbf{k}\sigma}(\omega_1) \mathbf{v}_{\mathbf{k}\beta} A_{\mathbf{k}\sigma}(\omega_1 + \omega)]. \quad (3.95)$$

To calculate the optical conductivity numerically, we need to know the spectral function  $A_{\mathbf{k}\sigma}^{\mu\nu}$  or the  $\mathbf{k}$ -dependent Green's function  $G_{\mathbf{k}\sigma}^{\mu\nu}(\omega)$ . In DMFT, the latter is approximated by

$$G_{\mathbf{k}\sigma}^{\mu\nu}(\omega) = [\omega + \mu - \epsilon_{\mathbf{k}} - \Sigma(\omega)]_{\mu\nu}^{-1}, \quad (3.96)$$

where  $\Sigma^{\mu\sigma}(\omega)$  is the real-frequency self-energy. Since the local Green's function  $G_{\sigma}^{\mu\nu}(\omega)$  can be obtained by the maximum entropy method,  $\Sigma^{\mu\sigma}(\omega)$  is then given by inversion of

$$G_{\sigma}^{\mu\nu}(\omega) = \frac{1}{\mathcal{V}} \sum_{\mathbf{k}} [\omega + \mu - \epsilon_{\mathbf{k}} - \Sigma(\omega)]_{\mu\nu}^{-1}. \quad (3.97)$$

For the realistic model (2.23), this can only be done numerically.

**Sum rule** Now we turn to the so-called  $f$ -sum rule (for a detailed discussion, see [Blümer 2003]). The Green's function  $G_{\mathbf{k}\sigma}^{\mu\nu}(\omega)$  satisfies the Kramers-Kronig relation

$$\text{Re}G_{\mathbf{k}\sigma}(\omega) = \frac{\mathcal{P}}{\pi} \int_{-\infty}^{+\infty} d\omega' \frac{\text{Im}G_{\mathbf{k}\sigma}(\omega')}{\omega' - \omega}. \quad (3.98)$$

Thus

$$\begin{aligned} & \int_0^{+\infty} d\omega' \int_{-\infty}^{+\infty} d\omega \frac{f(\omega) - f(\omega + \omega')}{\omega'} \text{Tr}[\mathbf{v}_{\mathbf{k}\alpha} \text{Im}G_{\mathbf{k}\sigma}(\omega) \mathbf{v}_{\mathbf{k}\alpha} \text{Im}G_{\mathbf{k}\sigma}(\omega + \omega')] \\ &= \frac{1}{2} \int_{-\infty}^{+\infty} d\omega \int_{-\infty}^{+\infty} d\omega' \frac{f(\omega) - f(\omega')}{\omega' - \omega} \text{Tr}[\mathbf{v}_{\mathbf{k}\alpha} \text{Im}G_{\mathbf{k}\sigma}(\omega) \mathbf{v}_{\mathbf{k}\alpha} \text{Im}G_{\mathbf{k}\sigma}(\omega')] \\ &= \int_{-\infty}^{+\infty} d\omega f(\omega) \text{Tr}[\mathbf{v}_{\mathbf{k}\alpha} \text{Im}G_{\mathbf{k}\sigma}(\omega) \mathbf{v}_{\mathbf{k}\alpha} \int_{-\infty}^{+\infty} d\omega' \frac{\text{Im}G_{\mathbf{k}\sigma}(\omega')}{\omega' - \omega}] \\ &= \pi \int_{-\infty}^{+\infty} d\omega f(\omega) \text{Tr}[\mathbf{v}_{\mathbf{k}\alpha} \text{Im}G_{\mathbf{k}\sigma}(\omega) \mathbf{v}_{\mathbf{k}\alpha} \text{Re}G_{\mathbf{k}\sigma}(\omega)]. \end{aligned} \quad (3.99)$$

Since Eq. (3.96) implies

$$\frac{\partial}{\partial \mathbf{k}_\alpha} \text{Im}G_{\mathbf{k}\sigma} = 2 \text{Im}G_{\mathbf{k}\sigma} \mathbf{v}_{\mathbf{k}\alpha} \text{Re}G_{\mathbf{k}\sigma}, \quad (3.100)$$

we have

$$\int_{-\infty}^{+\infty} d\omega f(\omega) \text{Tr}[\mathbf{v}_{\mathbf{k}\alpha} \text{Im}G_{\mathbf{k}\sigma}(\omega) \mathbf{v}_{\mathbf{k}\alpha} \text{Re}G_{\mathbf{k}\sigma}(\omega)] = -\frac{\pi}{\hbar} \text{Tr} \left[ \mathbf{v}_{\mathbf{k}\alpha} \frac{\partial n_{\mathbf{k}\sigma}}{\partial \mathbf{k}_\alpha} \right] = \frac{\pi}{\hbar} \text{Tr} \left[ \frac{\partial \mathbf{v}_{\mathbf{k}\alpha}}{\partial \mathbf{k}_\alpha} n_{\mathbf{k}\sigma} \right], \quad (3.101)$$

where  $n_{\mathbf{k}\sigma}$  is the electron momentum distribution function

$$n_{\mathbf{k}\sigma} \equiv \hbar \int d\omega f(\omega) A_{\mathbf{k}\sigma}(\omega). \quad (3.102)$$

Integrating  $\text{Re}\sigma_{\alpha\alpha}(\omega)$  over all positive frequencies then yields

$$\int_0^{+\infty} d\omega \text{Re}\sigma_{\alpha\alpha}(\omega) = \frac{\pi e^2}{2\hbar^2 \mathcal{V}} \sum_{\mathbf{k}\sigma} \text{Tr} \left[ \frac{\partial \mathbf{v}_{\mathbf{k}\alpha}}{\partial \mathbf{k}_\alpha} n_{\mathbf{k}\sigma} \right]. \quad (3.103)$$

For a cubic lattice, the dispersion obeys

$$\sum_{\alpha=1}^d \frac{\partial \mathbf{v}_{\mathbf{k}\alpha}}{\partial \mathbf{k}_\alpha} = -a^2 \epsilon_{\mathbf{k}}, \quad (3.104)$$

where  $d$  is the spatial dimension. Eq. (3.103) becomes

$$\int_0^{+\infty} d\omega \text{Re}\sigma_{\alpha\alpha}(\omega) = -\frac{\pi e^2}{2\hbar^2 a d} \frac{1}{N} \sum_{\mathbf{k}\sigma} \text{Tr}[\epsilon_{\mathbf{k}} n_{\mathbf{k}\sigma}], \quad (3.105)$$

where  $N = \mathcal{V}/a^3$  is the number of the lattice sites and  $\frac{1}{N} \sum_{\mathbf{k}\sigma} \text{Tr}[\epsilon_{\mathbf{k}} n_{\mathbf{k}\sigma}]$  is the kinetic energy of the conduction electrons. Eq. (3.105) is called the  $f$ -sum rule. It relates the integral of  $\text{Re}\sigma_{\alpha\alpha}(\omega)$  to the kinetic energy of the conduction electrons. Note that we have to use the maximum entropy method in order to get the optical conductivity, whereas the electron momentum distribution function  $n_{\mathbf{k}\sigma}$  and hence the kinetic energy can be calculated directly by summing over the Matsubara frequency in Eq. (3.72). The sum rule thus provides a powerful tool for checking the reliability of our numerical results.

Integrating over the frequency from 0 to  $\omega$ , we can define

$$S(\omega) = \frac{2}{\pi} \int_0^\omega d\omega' \sigma(\omega'). \quad (3.106)$$

This gives

$$N_{eff}(\omega) = \frac{\mathcal{V}m}{e^2} S(\omega), \quad (3.107)$$

and

$$K(\omega) = \frac{a}{e^2} S(\omega). \quad (3.108)$$

which are often used in experiments and represent the effective carrier concentration and their kinetic energy, respectively.

### 3.5 LDA+DMFT approach

In this section, we introduce the LDA+DMFT approach. The LDA approach has been very successful for weakly-correlated systems [Jones & Gunnarsson 1989]. By combining LDA with DMFT, the LDA+DMFT approach allows for a realistic investigation of correlated materials. Although the realistic model (2.20) is believed to provide a good description of the electronic structure and the lattice effects in the perovskite manganites, the realistic lattice structure is more complicated, which may significantly affect the electronic behavior and require a better treatment. Therefore, a comparison between LDA+DMFT investigations and DMFT model calculations is certainly helpful. This will be done in the next chapter. In the following, we first give a brief introduction to the density functional theory and the local density approximation and then explain the LDA+DMFT approach.

**Band theory** One of the most important theorems in solid state physics is the Bloch theorem which states that for free electrons moving in a lattice with periodic potential  $V(\mathbf{r} + \mathbf{R}) = V(\mathbf{r})$ , the wave function  $\psi(\mathbf{r})$  must follow the condition:

$$\psi(\mathbf{r} + \mathbf{R}) = e^{i\mathbf{k}\cdot\mathbf{R}}\psi(\mathbf{r}), \quad (3.109)$$



where  $\mathbf{k}$  is some vector in the Brillouin zone and  $\mathbf{R}$  is any lattice vector.

The wave function can be expanded with respect to the discrete atomic states  $\phi_n(\mathbf{r})$ ,

$$\psi_{\mathbf{k}}(\mathbf{r}) = \sum_{\mathbf{R},n} c_n e^{i\mathbf{k}\cdot\mathbf{R}} \phi_n(\mathbf{r} + \mathbf{R}). \quad (3.110)$$

By solving the Schrödinger equation,

$$\left[ -\frac{\hbar^2}{2m_e} \nabla^2 + V(\mathbf{r}) \right] \psi(\mathbf{r}) = E\psi(\mathbf{r}), \quad (3.111)$$

we find that each atomic level gives rise to an energy band.

The conventional band theory does not take into account electronic correlations, so the many-electron wave function can be constructed from the Slater determinant of the single-electron wave functions. If the electron-electron interaction is taken into account, we have to solve the Hamiltonian

$$\begin{aligned} H = & \sum_{\sigma} \int d^3\mathbf{r} \Psi^{\dagger}(\mathbf{r}, \sigma) \left[ -\frac{\hbar^2}{2m_e} \nabla^2 + V_{ion}(\mathbf{r}) \right] \Psi(\mathbf{r}, \sigma) \\ & + \frac{1}{2} \sum_{\sigma\sigma'} \int d^3\mathbf{r} d^3\mathbf{r}' \Psi^{\dagger}(\mathbf{r}, \sigma) \Psi^{\dagger}(\mathbf{r}', \sigma') V_{ee}(\mathbf{r} - \mathbf{r}') \Psi(\mathbf{r}', \sigma') \Psi(\mathbf{r}, \sigma), \end{aligned} \quad (3.112)$$

where  $\Psi^{\dagger}(\mathbf{r}, \sigma)$  and  $\Psi(\mathbf{r}, \sigma)$  are field operators that create and annihilate an electron at position  $\mathbf{r}$  with spin  $\sigma$ ,  $V_{ion}(\mathbf{r})$  denotes the ionic potential and  $V_{ee}(\mathbf{r} - \mathbf{r}')$  is the Coulomb interaction between electrons. The density functional theory was then developed to study the ground-state properties of correlated electrons.

**Density functional theory** The basic theorem of the density functional formalism was derived by Hohenberg and Kohn in 1964 [Hohenberg & Kohn 1964]. A simpler but more general derivation was later given by Levy [Levy 1982]. The theorem states that the ground state of Hamiltonian (3.112) is uniquely determined by its electron density  $\rho_{GS}(\mathbf{r})$  if it is nondegenerate, and the ground state energy,  $E[\rho(\mathbf{r})]$ , is a functional of the electron density whose minimum is given by  $\rho_{GS}(\mathbf{r})$ . In general,  $E[\rho(\mathbf{r})]$  is a nonlocal functional of  $\rho_{GS}(\mathbf{r})$ .

The theorem is easy to prove since the ground state is by definition the lowest energy state:

$$\begin{aligned} E_{GS} &= \min_{\phi(\mathbf{r}_i, \sigma_i)} \langle \phi(\mathbf{r}_i, \sigma_i) | H | \phi(\mathbf{r}_i, \sigma_i) \rangle \\ &= \min_{\rho(\mathbf{r})} \min_{\phi_{\rho}(\mathbf{r}_i, \sigma_i)} \langle \phi_{\rho}(\mathbf{r}_i, \sigma_i) | H | \phi_{\rho}(\mathbf{r}_i, \sigma_i) \rangle, \end{aligned} \quad (3.113)$$

where  $\phi_\rho(\mathbf{r}_i, \sigma_i)$  denotes the many-electron wave function  $\phi(\mathbf{r}_i, \sigma_i)$  which has the electron density  $\rho(\mathbf{r})$ . If we define the energy functional

$$E[\rho(\mathbf{r})] = \min_{\phi_\rho(\mathbf{r}_i, \sigma_i)} \langle \phi_\rho(\mathbf{r}_i, \sigma_i) | H | \phi_\rho(\mathbf{r}_i, \sigma_i) \rangle, \quad (3.114)$$

$E[\rho(\mathbf{r})]$  achieves its minimum  $E_{GS}$  when the electron density is  $\rho_{GS}(\mathbf{r})$ .

The theorem tells us nothing about the property of the ground state. However, by relating the electron density to a set of one-particle wave functions  $\phi_i(\mathbf{r})$  via

$$\rho(\mathbf{r}) = \sum_{i=1}^N |\phi_i(\mathbf{r})|^2, \quad (3.115)$$

$E[\rho(\mathbf{r})]$  can be minimized with respect to  $\phi_i$  instead of  $\rho$  to yield the Kohn-Sham equation [Kohn & Sham 1964, Kohn & Sham 1965, Sham & Kohn 1966]:

$$\left[ -\frac{\hbar^2}{2m_e} \nabla^2 + V_{ion}(\mathbf{r}) + \int d^3\mathbf{r}' V_{ee}(\mathbf{r} - \mathbf{r}') \rho(\mathbf{r}') + \frac{\delta E_{xc}[\rho(\mathbf{r})]}{\delta \rho(\mathbf{r})} \right] \phi_i(\mathbf{r}) = \epsilon_i \phi_i(\mathbf{r}), \quad (3.116)$$

where  $\epsilon_i$  denotes the Lagrange parameters and  $E_{xc}[\rho(\mathbf{r})]$  is the exchange-correlation energy, given by the total Coulomb energy minus the Hartree energy

$$E_{Hartree}[\rho(\mathbf{r})] = \frac{1}{2} \int d^3\mathbf{r} d^3\mathbf{r}' \rho(\mathbf{r}') \rho(\mathbf{r}) V_{ee}(\mathbf{r} - \mathbf{r}'). \quad (3.117)$$

Eq. (3.116) has the same form as a one-particle Schrödinger equation, which, together with Eq. (3.115), yields a set of self-consistent equations and can be solved numerically if we can write down the explicit form of the exchange-correlation energy functional  $E_{xc}[\rho(\mathbf{r})]$ . But  $E_{xc}[\rho(\mathbf{r})]$  is generally not known, so we have to make approximations.

**Local density approximation (LDA)** LDA assumes that the electron density varies slowly in the real space so that the exchange-correlation energy functional  $E_{xc}[\rho(\mathbf{r})]$  can be approximated by a function that depends only locally on the electron density, i.e.

$$E_{xc}[\rho(\mathbf{r})] = \int d^3\mathbf{r} \mathcal{E}_{xc}^{LDA}(\rho(\mathbf{r})). \quad (3.118)$$

$\mathcal{E}_{xc}^{LDA}(\rho(\mathbf{r}))$  can be obtained approximately from the perturbation calculation or the numerical simulation of the jellium problem with a uniform ionic potential. The result is [Kohn & Sham 1965]

$$\mathcal{E}_{xc}^{LDA}(\rho(\mathbf{r})) = -\alpha \rho(\mathbf{r})^{\frac{4}{3}}, \quad (3.119)$$

where  $\alpha = 3/4(3/\pi)^{1/3}$  can be varied in the so-called  $X\alpha$  method proposed by Slater to take into account some corrections (see, e.g., [Jones & Gunnarsson 1989]). With this approximation, Eqs. (3.115) and (3.116) can be solved in an iterative way.

**LDA+DMFT approach** If we interpret the Lagrange parameters  $\epsilon_i$  in the Kohn-Sham equation (3.116) as the physical energy of the one-particle excitation, the LDA calculations produce the band structure of the electronic system. By expanding the field operators with respect to a suitable basis, we obtain a tight-binding Hamiltonian

$$H^{LDA} = \sum_{ij;\mu\nu\sigma} t_{\mu\nu}^{ij} c_{i\mu\sigma}^\dagger c_{j\nu\sigma} = \sum_{\mathbf{k};\mu\nu\sigma} \epsilon^{\mu\nu}(\mathbf{k}) c_{\mathbf{k}\mu\sigma}^\dagger c_{\mathbf{k}\nu\sigma}, \quad (3.120)$$

where  $i, j$  denote the lattice sites and  $\mu, \nu$  the orbital indices. In our work (see chapter 4), the NMTO ( $N$ th-order Muffin tin orbitals) method is used to generate a minimal basis set (Mn  $e_g$  basis). Details about this method can be found in Refs. [Andersen & Saha-Dasgupta 2000, Pavarini et al. 2004, Pavarini et al. 2005, Zurek et al. 2005].

The Kohn-Sham equation (3.116) is based on a single particle picture. For strongly correlated system such as d and f electron system, the strong on-site Coulomb interactions have to be taken into account. This yields the low-energy Hamiltonian

$$H = H^{LDA} + \frac{1}{2} \sum_{i\mu\nu\sigma} U_{\mu\nu} n_{i\mu\sigma} n_{i\nu\sigma} + \frac{1}{2} \sum_{i\mu(\neq\nu)\sigma} (U_{\mu\nu} - J_{\mu\nu}) n_{i\mu\sigma} n_{i\nu\sigma}, \quad (3.121)$$

where  $U_{\mu\nu}$  is the general intra- or inter-orbital Coulomb interaction and  $J_{\mu\nu}$  is the exchange interaction. This low-energy Hamiltonian can be solved by DMFT. In this way, the LDA+DMFT approach combines the LDA band structure calculations and the DMFT calculations for strong electronic correlations.

The LDA+DMFT approach has been successfully applied to many materials such as the transition metals Fe and Ni [Lichtenstein et al. 2001], the transition metal oxides  $V_2O_3$  [Held et al. 2001a, Laad et al. 2003],  $SrRuO_3$  [Liebsch & Lichtenstein 2000],  $SrVO_3$  [Nekrasov et al. 2000, Nekrasov et al. 2002, Nekrasov et al. 2005], and  $LaTiO_3$  [Anisimov et al. 1997, Zöfl et al. 2000, Nekrasov et al. 2000], as well as the rare earth element such as Ce [Zöfl et al. 2001, Held et al. 2001b, McMahan et al. 2003] etc. On the other hand, the electronic correlations also affect the ground state properties (the electron density) and thus the band structure. This feedback from DMFT to LDA can be important. Such a fully self-consistent LDA+DMFT scheme is presently under development [Savrasov & Kotliar 2004, Anisimov et al. 2005].



## 4 Pressure-induced metal-insulator transition

LaMnO<sub>3</sub> is well-known to be an insulator at ambient conditions, but the physical mechanism is not yet sufficiently understood. Although both the Coulomb interaction and the Jahn-Teller coupling can give rise to the insulating behavior, their relative importance in LaMnO<sub>3</sub> is still under debate [Loa et al. 2001, Banach & Temmerman 2004, Zenia et al. 2005]. To clarify the individual roles of both interactions, we study the pressure-induced insulator-to-metal (IM) transition in LaMnO<sub>3</sub> [Loa et al. 2001] and compare the experimental results with the LDA+DMFT calculations. The chapter is outlined as follows: In section 4.1 we explain in detail the experiment on the pressure-induced metal-insulator transition. The LDA+DMFT calculations are presented in section 4.2. By comparing the LDA and LDA+DMFT results with experiment, we show that the realistic crystal field splitting is not enough to produce an insulating ground state at ambient conditions. We conclude that both the Coulomb interaction and the Jahn-Teller coupling are necessary for understanding the electronic behavior of LaMnO<sub>3</sub> and, contrary to earlier works [Loa et al. 2001, Banach & Temmerman 2004, Zenia et al. 2005], the pressure-induced insulator-to-metal transition is not of Mott-Hubbard type. Section 4.3 is devoted to the DMFT model calculations. The explicit inclusion of the Jahn-Teller phonons allows us to study the dynamic Jahn-Teller effect and thus the structural (orbital order-disorder) transition from dynamic to static Jahn-Teller distortion in LaMnO<sub>3</sub>.

### 4.1 Experiment

At ambient conditions LaMnO<sub>3</sub> is an insulator with 3  $t_{2g}$  electrons and 1  $e_g$  electron. Above 1000 K, it has a rhombohedral structure. At the cooperative Jahn-Teller temperature  $T_{OO} = 740$  K, it undergoes a structural transition from a weakly distorted orthorhombic phase with the GdFeO<sub>3</sub>-type distortion (rotation of MnO<sub>6</sub> octahedra) to a strongly distorted orthorhombic structure with an additional static cooperative Jahn-Teller distortion. The structural transition is accompanied by an orbital ordering transition. Below the Néel temperature  $T_N = 140$  K, LaMnO<sub>3</sub> has an A-type antiferromagnetic spin structure. These complicated behaviors (see the phase diagram Fig. 4.1) are due to the interplay of spin, orbital and lattice degrees of

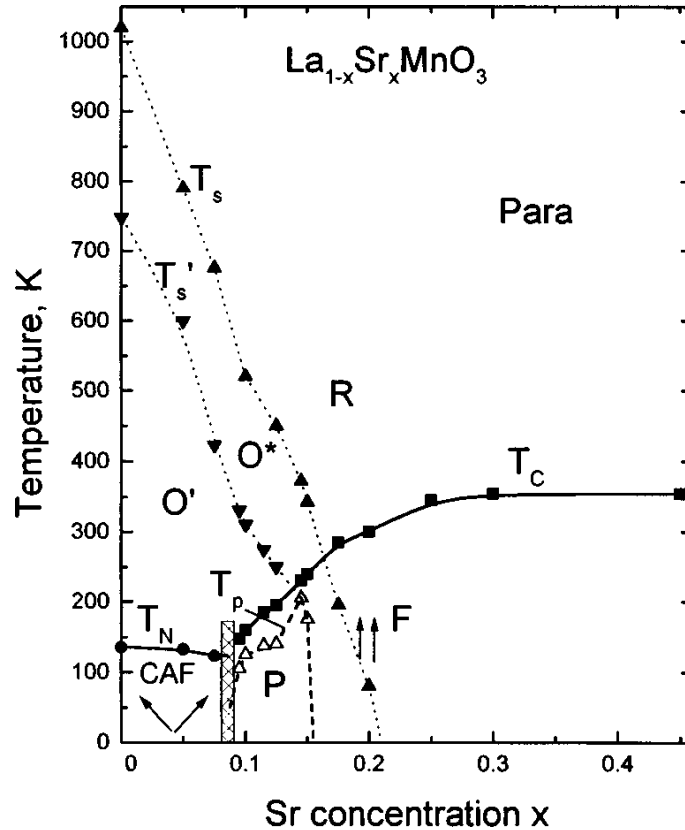


Figure 4.1: Structural and magnetic  $T$ - $x$  phase diagram of  $La_{1-x}Mn_xO_3$ .  $R$  — rhombohedral phase;  $O^*$  — weakly distorted orthorhombic phase;  $O'$  — strongly distorted (Jahn-Teller) orthorhombic phase;  $P$  — polaron-ordering phase;  $Para$  — paramagnetic phase;  $F$  — ferromagnetic phase;  $CAF$  — noncollinear phase;  $T_C$  and  $T_N$  — Curie temperature and Néel temperature;  $T_s$  and  $T'_s$  — temperature of the transitions  $O^* \rightarrow R$  and  $O' \rightarrow O^*$ , respectively; and  $T_p$  — temperature of the transition to the polaron-ordering phase. Figure taken from Ref. [Mukhin et al. 1998].

freedom.

When an external pressure is applied, an insulator-to-metal transition is observed at 32 GPa [Loa et al. 2001]. While the strength of the Coulomb interaction is not much affected by pressure, the lattice distortion which is defined by the displacements of the oxygen atoms from the equilibrium positions is significantly reduced under pressure. This reduction of the lattice distortion also changes the angle of the Mn-O-Mn bond and thus enhances the effective bandwidth of the  $e_g$  electrons. Both effects may lead to an insulator-to-metal transition.

An important question is whether the Jahn-Teller distortion is completely suppressed before the insulator-to-metal (IM) transition occurs. If the transition occurs at a higher pressure so that the Jahn-Teller distortion is completely suppressed at the transition point, namely,  $P_{IM} > P_{JT}$ , then the Coulomb interaction alone can already explain the insulating ground state and the Jahn-Teller coupling is not of particular importance for determining the electronic properties of  $\text{LaMnO}_3$ . But if, on the contrary, the transition happens at a lower pressure, namely,  $P_{IM} < P_{JT}$ , then the Jahn-Teller distortion is indispensable for making  $\text{LaMnO}_3$  an insulator. The pressure-induced insulator-to-metal transition thus provides a good example to study the relative importance of the Coulomb interaction and the Jahn-Teller coupling in manganites.

The experimental study of the pressure-induced insulator-to-metal transition [Loa et al. 2001] was carried out at a temperature of 300 K. By applying a pressure up to 40 GPa, the lattice structure of  $\text{LaMnO}_3$  was studied by x-ray powder diffraction and the lattice parameters and atomic positions were determined. Fig. 4.2(a) and Fig. 4.2(b) show that with increasing pressure, the lattice parameters and correspondingly the volume of the unit-cell and the  $\text{MnO}_6$  octahedra are considerably reduced. In Fig. 4.2(c), the atomic coordinates of the La ions change continuously up to 12 GPa. Then the intensity of the (111) reflection becomes zero (see the inset of Fig. 4.2(c)), indicating that the position of the La ion remains located at  $x=0$  (and  $x=1/2$ ).

Fig. 4.2(d) shows the lengths of the three different Mn-O bonds as a function of pressure. This allows for the determination of the amplitude of the Jahn-Teller distortion. The data was measured only up to 11 GPa. In [Loa et al. 2001], they were fit linearly versus pressure and then found to become equal at about 18 GPa. So the static Jahn-Teller distortion was expected to be completely suppressed above 18 GPa.

On the other hand, the insulator-to-metal transition occurs at a much higher pressure. Below 32 GPa, the optical reflectivity spectra has a broad peak around 2 eV [Fig. 4.3(a)] corresponding to an optical transition and a related 1 eV energy gap, which agrees with other optical experiments [Jung et al. 1998, Takenaka et al. 1999] and reflects the insulating nature of  $\text{LaMnO}_3$  at ambient pressure. The dramatic change of the shape of the spectra at higher pressure indicates an insulator-to-metal transition at 32 GPa. This is further confirmed by the electrical resistivity measurements. In Fig. 4.3(b), the resistance shows a sharp drop and a change in sign of  $dR(T)/dT$  at 32 GPa.

Since for a linear extrapolation the lattice distortion exists only below 18 GPa, an intermediate insulating phase which is dominated by the Coulomb interaction

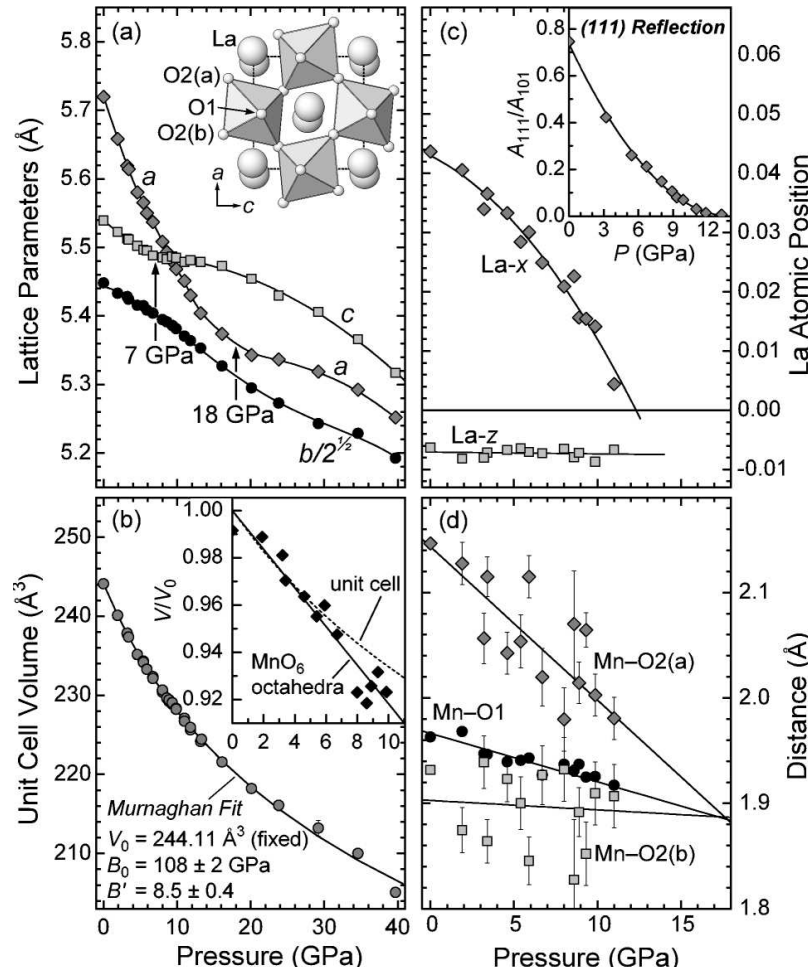


Figure 4.2: (a) Lattice parameters of  $\text{LaMnO}_3$  at ambient temperature as a function of pressure. The crystal structure of  $\text{LaMnO}_3$  is also shown in the inset. (b) Volume of the unit cell and the  $\text{MnO}_6$  octahedra versus pressure. (c) Atomic coordinates of La ions as a function of pressure ( $y_{\text{La}} = 1/4$ ). (d) Lengths of the Mn-O bonds versus pressure. Figure taken from Ref. [Loa et al. 2001]

alone was suggested in [Loa et al. 2001]. It was argued that the insulator-to-metal transition at 32 GPa must be purely a result of the increasing electronic bandwidth under pressure and thus a (bandwidth-control) Mott transition. This also means that even if the Jahn-Teller coupling may somehow enhance the insulating behavior, it does not play an important role in determining the electronic properties of  $\text{LaMnO}_3$ .

This is puzzling since it seems to contradict the tendency to attribute a major



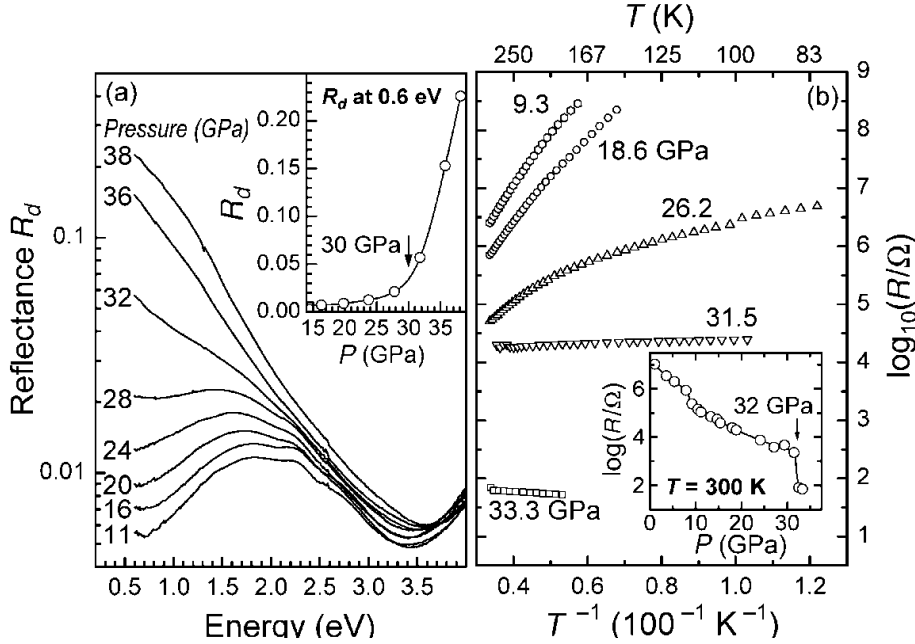


Figure 4.3: (a) Optical reflectivity spectra of  $\text{LaMnO}_3$  at  $T = 300$  K as a function of pressure. (b) Temperature dependence of the resistance at different pressures. The inset shows the pressure dependence of the resistance at  $T = 300$  K. The arrow marks the insulator-to-metal transition at 32 GPa. Figure taken from Ref. [Loa et al. 2001].

role to the Jahn-Teller coupling in the physics of manganites [Millis et al. 1995]. For this, we note that the above argument is based on the single fact that the lengths of the three Mn-O bonds would become equal to each other when extrapolated to the pressure 18 GPa. In fact, there is no guarantee that the bond lengths should behave linearly with pressure. This leaves some ambiguity and should be further discussed.

## 4.2 LDA+DMFT investigations

In this section, we study the pressure-induced insulator-to-metal transition using the LDA+DMFT approach. We will see from the LDA band structure that the realistic crystal field splitting is not enough to produce an insulating ground state in  $\text{LaMnO}_3$  at ambient conditions. The on-site Coulomb interaction is then taken into account and studied by DMFT. The results agree well with experimental observations and demonstrate the indispensable role of both the Coulomb interaction and the Jahn-Teller coupling. The work of this section has been published in [Yamasaki et al. 2006].

### 4.2.1 Band structures

The LDA band structure calculation was performed based on the orthorhombic crystal structure of  $\text{LaMnO}_3$  shown in Fig. 4.4. The  $\text{O}_6$  octahedra are elongated in the  $y$  direction (nearly parallel to  $\mathbf{b}-\mathbf{a}$ ) in subcells 1 and 3, and in the  $x$  direction (nearly parallel to  $\mathbf{b}+\mathbf{a}$ ) in subcells 2 and 4. Both the  $\text{GdFeO}_3$ -type distortion and the Jahn-Teller distortion are included in the calculation and the lattice parameters are taken from the experiment in Ref. [Loa et al. 2001]. The Jahn-Teller distortion can be estimated from Fig. 4.2(d). It decreases linearly from 11% at 0 GPa to 4% at 11 GPa. The  $\text{GdFeO}_3$ -type distortion tilts the corner sharing octahedra around the  $b$  axis and rotate them around the  $c$  axis, both in alternating directions. When the pressure increases from 0 to 11 GPa, the tilt is reduced from  $12^\circ$  to  $8^\circ$  and the rotation from  $7^\circ$  to  $5^\circ$ .

Fig. 4.5 shows the paramagnetic LDA bands at normal pressure for both the orthorhombic structure (top right) and the hypothetical cubic structure with the same volume (top left). Since there are 4 subcells in each unit cell for the orthorhombic structure, the total number of the bands is then 4 times larger compared to that for the cubic structure. The dashed bands were obtained with a large basis set of  $N$ th-order muffin tin orbitals (NMTOs) [Andersen & Saha-Dasgupta 2000, Pavarini et al. 2004, Pavarini et al. 2005, Zurek et al. 2005]. We see  $3(\times 4)$   $\text{Mn } t_{2g}$  and  $2(\times 4)$   $\text{Mn } e_g$  bands. Near the top of Fig. 4.5 — and continuing above it — is

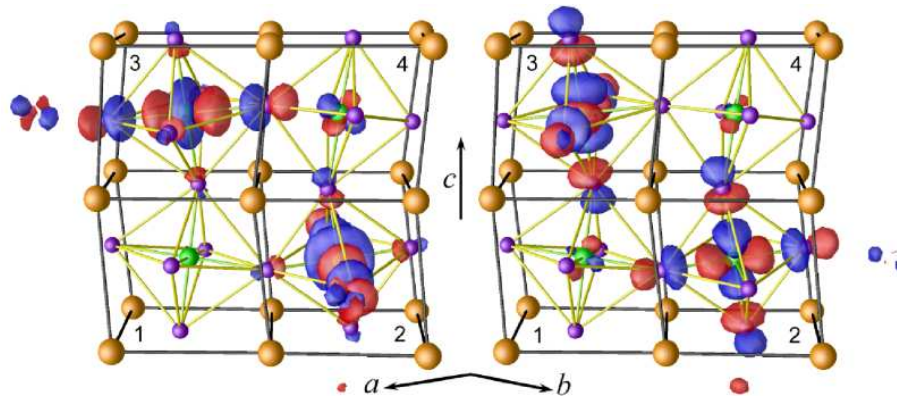


Figure 4.4:  $\text{LaMnO}_3$  orthorhombic translational cell ( $Pbnm$ ) and LDA-NMTO  $\text{Mn } e_g$  crystal-field orbital  $|1\rangle$  (left) and  $|2\rangle$  (right) of respectively lowest and highest energy. The orbitals have been placed only in subcells 3 and 2; those in subcells 1 and 4 may be obtained by the  $\text{LaO}$  mirror plane perpendicular to the  $c(=z)$  axis. Since they have antibonding  $\text{O } 2p$  tails, orbitals  $|1\rangle$  and  $|2\rangle$  are directed respectively along and perpendicular to the longest  $\text{Mn}-\text{O}$  bond. Red/blue indicates a positive/negative sign.

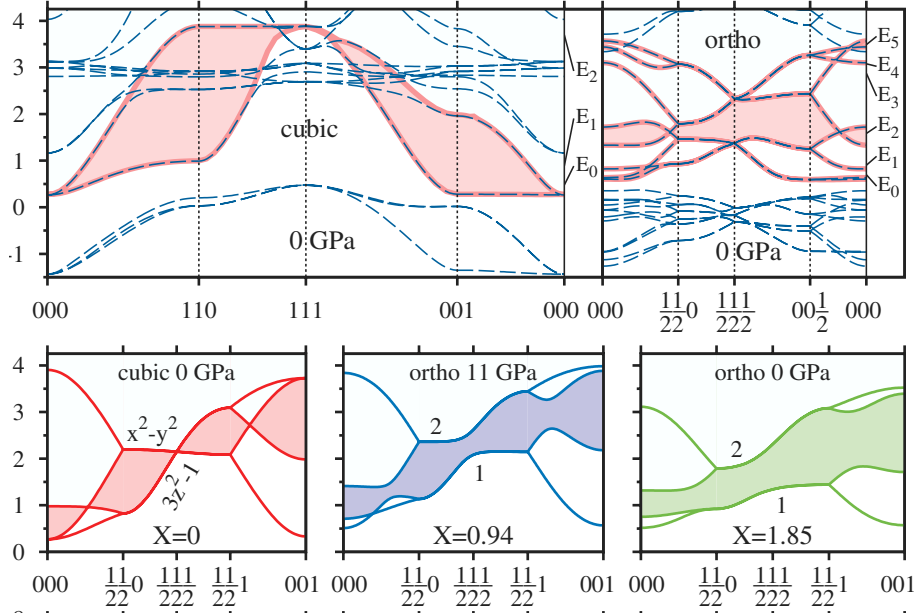


Figure 4.5: **Top:** Paramagnetic LDA band structure for orthorhombic (right) and hypothetical cubic (left)  $\text{LaMnO}_3$  at 0 GPa plotted along the high-symmetry lines in the  $k_x=k_y$  plane. Energies are in eV, the  $\mathbf{k}$ -unit is  $\pi$ , and the  $\mathbf{k}$ -points marked are  $\Gamma\text{MRX}\Gamma$  in the cubic, and  $\Gamma\text{YTZ}\Gamma$  in the orthorhombic Brillouin zone (BZ). The latter is folded in from the former and has the following smallest inequivalent reciprocal-lattice vectors:  $\mathbf{Q} = 000, 110, 111,$  and  $001$ . Dashed blue bands: large NMTO basis set; red bands: Mn  $e_g$  NMTO basis set employed in the low-energy Hamiltonian used later in LDA+DMFT calculation. The  $N+1$  support energies  $E_i$  are shown at the right-hand sides. The zero of energy corresponds to configuration  $t_{2g}^4$ . **Bottom:** 0 and 11 GPa orthorhombic (0 GPa cubic)  $e_g$  bands folded out (in) to the  $(000, 110)$ -BZ. The dimensionless band-shape parameter,  $X$ , is the LDA crystal-field splitting in units of the effective hopping integral  $t \equiv |t_{dd\sigma}| \sim W/6$ , both obtained from the NMTO Mn  $e_g$  Wannier functions.

the La  $5d$  band which is pushed 2 eV up by  $pd\sigma$  hybridization with oxygen when going from the cubic to the orthorhombic structure. The narrow band crossing the cubic Mn  $e_g$  band is La  $4f$ , and the O  $2p$  bands are below and not shown.

The minimum basis set, here the Mn  $e_g$  basis, generated by the NMTO down-folding gives rise to the red solid bands in Fig. 4.5. The corresponding Wannier functions are essentially localized so that a Mn  $e_g$  orbital has no  $e_g$  character on neighboring Mn atoms.

The bottom of Fig. 4.5 shows the  $e_g$  bands in a reduced Brillouin zone. For the realistic orthorhombic structure, we see clearly the crystal field splitting between two  $e_g$  orbitals. The LDA calculations produce a crystal field splitting  $X = \Delta_{JT}/t$

of 1.85 at 0 GPa and 0.94 at 11 GPa. Yet, even though the crystal field splitting is present, the two  $e_g$  orbitals still overlap with each other and we get a metallic behavior, contrary to the experimental fact that  $\text{LaMnO}_3$  is an insulator below 32 GPa.

This demonstrates that the Jahn-Teller coupling alone cannot explain the insulating ground state found in  $\text{LaMnO}_3$  at ambient conditions. The deviation of LDA calculations from experiments is a general phenomenon since by neglecting the on-site Coulomb interaction, the LDA band structure calculation fails for strongly correlated materials such as transition metals, transition metal oxides, and f-metals. In these materials, the localized  $d$ - and  $f$ -orbitals are extensively overlapping on the same site and hence the on-site Coulomb interaction is of prime importance. Below, we will take into account the Coulomb interaction between the  $e_g$  electrons and use the LDA+DMFT approach to investigate its effect in  $\text{LaMnO}_3$ .

#### 4.2.2 Electronic properties

Including the Hund's coupling between the  $e_g$  and  $t_{2g}$  spins and the Coulomb interaction between the  $e_g$  orbitals, the low-energy Hamiltonian reads

$$\begin{aligned}
 H = & - \sum_{ij;\mu\nu\sigma} t_{\mu\nu}^{ij} c_{i\mu\sigma}^\dagger c_{j\nu\sigma} - 2J \sum_{i;\mu} \mathbf{s}_{i\mu} \cdot \mathbf{S}_i \\
 & + U \sum_{i;\mu} n_{i\mu\uparrow} n_{i\mu\downarrow} + \sum_{i;\sigma\bar{\sigma}} (V - \delta_{\sigma\bar{\sigma}} F) n_{i1\sigma} n_{i2\bar{\sigma}}
 \end{aligned} \tag{4.1}$$

where  $t_{\mu\nu}^{ij}$  is the LDA Hamiltonian in the representation of the two ( $\mu=1,2$ )  $e_g$  NMTO-Wannier orbitals per site (see Fig. 4.4 and Fig. 4.5). The second line describes the intra- and inter-orbital Coulomb interactions between  $e_g$  electrons, and  $F$  is the  $e_g$ - $e_g$  exchange interaction. We have  $V = U - 2F$  due to the cubic symmetry.

In our work, the Hund's coupling  $2J|\mathbf{S}| = 2.7$  eV is estimated by the splitting of the  $e_g^\uparrow$  and  $e_g^\downarrow$  bands in a ferromagnetic NMTO calculation. The Coulomb interaction  $U = 5$  eV is estimated from Ref. [Park et al. 1996]. We take  $F = 0.75$  eV so that  $V = 3.5$  eV which is slightly larger than our estimates in section 2.4. Since at the moment we cannot say which estimate is better, we will take the larger value and focus mainly on the physics of the insulating behavior of  $\text{LaMnO}_3$ . We will see that our main conclusions do not change with a slightly smaller Coulomb interaction.

In the DMFT calculations, the orbital off-diagonal elements of the on-site Green's function are neglected for simplicity. The DMFT density for  $e_g$  orbitals is forced to have the same symmetry as the LDA crystal field with a rotation of the local basis from subcell to subcell (see Fig. 4.4). We believe that this is a good approximation for  $e_g$  systems.

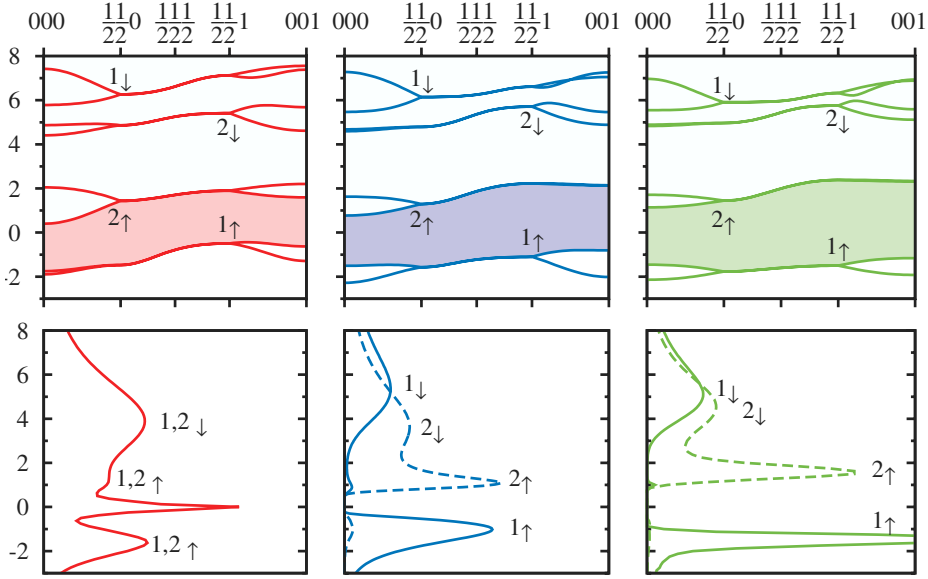


Figure 4.6: **Top:** From left to right: 0 GPa cubic, 11 and 0 GPa orthorhombic  $e_g$  bands, obtained by spin-polarized LDA+ $U$  for random spin orientations (room temperature), folded out (in) to the (000, 110)-BZ. The dimensionless band-shape parameter,  $X$ , is the LDA crystal-field splitting in units of the effective hopping integral  $t \equiv |t_{dd\sigma}| \sim W/6$ , both obtained from the NMTO Mn  $e_g$  Wannier functions. Bands are labelled by their main character. The zero of energy is the Fermi level. **Bottom:** Spectra calculated by LDA+DMFT. The full and dashed lines give the projections onto orbitals  $|1\rangle$  and  $|2\rangle$ , respectively.

Fig. 4.6 presents the LDA+ $U$  (top panel) and LDA+DMFT (bottom panel) results for the hypothetical cubic structure and the orthorhombic structure at 0 and 11 GPa. For the cubic structure without a crystal field splitting, even the strong Coulomb interaction cannot make the system insulating and the LDA+DMFT spectrum reveals a metallic feature with a sharp quasiparticle peak. It is only for the orthorhombic structure with a realistic crystal field splitting that we obtain an energy gap which is about 2 eV at 0 GPa and reduced to 1 eV at 11 GPa. The 2 eV energy gap at 0 GPa is slightly larger than the experimental result [Jung et al. 1998, Takenaka et al. 1999], implying a slightly larger Coulomb interaction used in the calculations. Also marked in the figure are the spin and orbital contributions to the spectra, illustrating the split spin states due to the Hund's coupling and the split orbitals due to the lattice distortion.

Comparing the LDA and LDA+DMFT results, we conclude that neither the Coulomb interaction nor the Jahn-Teller coupling is strong enough to give rise to the observed insulating behavior of  $\text{LaMnO}_3$  at ambient conditions. The electronic properties of manganites can only be understood from their combination of both.

To study the pressure-induced insulator-to-metal transition by LDA+DMFT, we need the pressure dependence of the lattice parameters with which the realistic crystal field splitting  $X$  and the  $e_g$  bandwidth  $W$  can be calculated by LDA. In Ref. [Loa et al. 2001], however, the lattice parameters were only measured below 11 GPa. As plotted in the left panel of Fig. 4.7, we have  $X = 1.85$  and  $W = 3.0$  eV at 0 GPa (square) and  $X = 0.94$  and  $W = 3.6$  eV at 11 GPa (triangle). To obtain the high pressure results, we have to extrapolate these LDA results for the 0 and 11 GPa orthorhombic structure. This can be done in two different ways. The first way is to fix the dimensionless crystal field splitting  $X = 0.94$  and rescale the bandwidth for the 11 GPa orthorhombic structure. The pressure dependence of the bandwidth for the cubic structure can be calculated by LDA (the red line). If we assume a similar pressure dependence for the 11 GPa orthorhombic structure, we obtain the blue line as shown in the left panel of Fig. 4.7. This gives a critical bandwidth  $W_c = 4$  eV at the transition point (32 GPa). In the second way, we connect the two points for the 0 and 11 GPa orthorhombic structure (the dotted line). This may include some

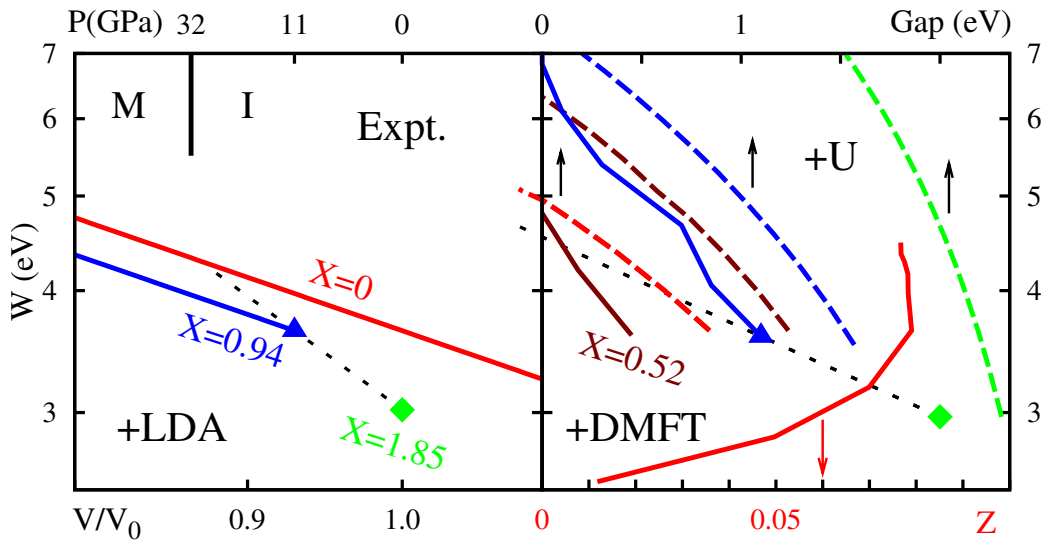


Figure 4.7: **Left:** LDA  $e_g$  bandwidths,  $W \sim 6t$ , calculated as functions of compression,  $V/V_0$ . The top abscissa gives the experimental pressures, with 32 GPa marking the observed IM transition [Loa et al. 2001]. **Right:** 300 K LDA+DMFT (solid lines) and LDA+U (dashed lines) results calculated as functions of  $W$ . For insulators, we plot the DOS gap (top scale) and for metals the quasiparticle weights (bottom scale). Full symbols indicate actual experimental structures and connecting black dotted lines are extrapolations. Each curve was calculated with fixed structure type (band shape): orthorhombic 0 GPa (green,  $X=1.85$ ), orthorhombic 11 GPa (blue,  $X=0.94$ ), cubic plus crystal-field splitting (dark red,  $X=0.52$ ), and cubic (red,  $X=0$ ).

effect of the reduction of the crystal field splitting  $X$  with increasing pressure. So we find a slightly larger critical bandwidth  $W_c = 4.5$  eV.

These results are supported by the linear extrapolation of the energy gap. The right panel of Fig. 4.7 depicts the LDA+U (dashed lines) and LDA+DMFT (solid lines) gap (or quasiparticle weight) as a function of the bandwidth. Let us focus on the LDA+DMFT results since LDA+U systematically overestimates the insulating gap. The DMFT calculations yield a 2 eV gap at 0 GPa (square) and a 1 eV gap at 11 GPa (triangle). The dotted line connects these two points and intersects with the  $W$ -axis at about 4.6 eV. All together, the LDA and LDA+DMFT calculations give a critical bandwidth  $W_c = 4.0 - 4.6$  eV at the insulator-to-metal transition point.

However, neither the cubic structure nor the 11 GPa orthorhombic structure allows for such a critical value. For the cubic structure (red line), the system is always metallic and has a finite quasiparticle weight in the whole calculated range ( $W > 2$  eV), whereas for the 11 GPa orthorhombic structure ( $X = 0.94$ , blue line), the energy gap only goes away for  $W > 7$  eV. In fact, it is only with a much reduced but still finite crystal field splitting  $X = 0.52$  (dark red line) that we find a comparable critical bandwidth  $W_c = 4.8$  eV. This shows that the lattice distortion is not fully suppressed at the insulator-to-metal transition point. There exists no intermediate insulating phase as suggested in Ref. [Loa et al. 2001].

Note that the above results are not affected by a small reduction of the on-site Coulomb interaction. The lattice distortion alone cannot give rise to an insulating behavior. We always need both the Coulomb interaction and the Jahn-Teller coupling to explain the finite energy gap in LaMnO<sub>3</sub> at ambient conditions. With a smaller  $U$ , an even larger crystal field splitting is required to account for the insulator-to-metal transition at 32 GPa.

In conclusion, both the Coulomb interaction and the Jahn-Teller coupling play very important and indispensable roles in determining the insulating nature of LaMnO<sub>3</sub> at ambient conditions. But neither is strong enough to make the system insulating. Fig. 4.8 illustrates the roles of the Coulomb interaction, the Jahn-Teller coupling, as well as the the Hund's rule coupling, in LaMnO<sub>3</sub>. The different spin and orbital components are first split by the Hund's rule coupling and the Jahn-Teller distortion. However, the splitting is not strong enough to make the system an insulator at 0 pressure. It is only with the on-site Coulomb interaction that the splitting is further enhanced, giving rise to the insulating behavior in LaMnO<sub>3</sub>. When an external pressure is applied, the lattice distortion is reduced and the effective bandwidth is enhanced. Hence the split  $e_g$  bands are pushed together with increasing pressure until they overlap with each other and the system becomes metallic. Therefore, there exists no intermediate insulating phase

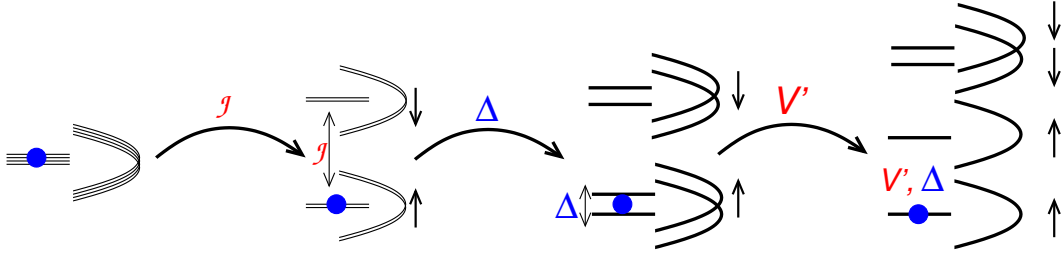


Figure 4.8: Diagram illustrating the roles of the Hund's rule coupling  $\mathcal{J}$ , the Coulomb interaction  $V'$ , and the Jahn-Teller splitting  $\Delta$  in determining the insulating nature of  $\text{LaMnO}_3$ .

dominated by the Coulomb interaction alone and the pressure-induced insulator-to-metal transition is not of Mott-Hubbard type, in contrast to previous claims in Refs. [Loa et al. 2001, Banach & Temmerman 2004, Zenia et al. 2005].

### 4.3 DMFT model calculations

In this section, we discuss the DMFT calculations for the realistic microscopic model proposed in section 2.4. Including the Jahn-Teller coupling, the Hamiltonian reads

$$\begin{aligned}
 H = & - \sum_{\langle\langle ij \rangle\rangle; \mu\nu\sigma} t_{\mu\nu}^{ij} c_{i\mu\sigma}^\dagger c_{j\nu\sigma} - 2J \sum_{i;\mu} \mathbf{s}_{i\mu} \cdot \mathbf{S}_i \\
 & + U \sum_{i;\mu} n_{i\mu\uparrow} n_{i\mu\downarrow} + \sum_{i;\sigma\bar{\sigma}} (V - \delta_{\sigma\bar{\sigma}} F) n_{i1\sigma} n_{i2\bar{\sigma}} \\
 & - g \sum_{i;\mu\nu\sigma} c_{i\mu\sigma}^\dagger (Q_{2i} \tau^x + Q_{3i} \tau^z)_{\mu\nu} c_{i\nu\sigma} + \sum_{i;a} \left( \frac{P_{ai}^2}{2} + \frac{\Omega^2}{2} Q_{ai}^2 \right), \quad (4.2)
 \end{aligned}$$

where  $t_{\mu\nu}^{ij}$  is the hopping integral:

$$t^x = t_0 \begin{pmatrix} \frac{3}{4} & -\frac{\sqrt{3}}{4} \\ -\frac{\sqrt{3}}{4} & \frac{1}{4} \end{pmatrix}, \quad t^y = t_0 \begin{pmatrix} \frac{3}{4} & \frac{\sqrt{3}}{4} \\ \frac{\sqrt{3}}{4} & \frac{1}{4} \end{pmatrix}, \quad t^z = t_0 \begin{pmatrix} 0 & 0 \\ 0 & 1 \end{pmatrix}. \quad (4.3)$$

The parameters are again  $U = 5 \text{ eV}$ ,  $F = 0.75 \text{ eV}$ , and, due to symmetry,  $V = U - 2F = 3.5 \text{ eV}$ . The Hund's coupling  $2J|\mathbf{S}| = 2.7 \text{ eV}$  is estimated by the splitting of the  $e_g^\uparrow$  and  $e_g^\downarrow$  bands in a ferromagnetic NMTO calculation as is in the LDA+DMFT calculations. From Raman spectroscopy [Iliev et al. 1998], we obtain the phonon frequency  $\Omega = 0.07 \text{ eV}$ . The Jahn-Teller coupling  $g$  is left for the moment as a free parameter.

Unlike the LDA band structure calculations which take care of the effect of the static lattice distortion, the explicit inclusion of the Jahn-Teller phonons in the



model Hamiltonian (4.2) allows us to treat the dynamic Jahn-Teller effect. In the following, we first discuss the dynamic Jahn-Teller distortion which is related directly to the Jahn-Teller coupling  $g$ . We show that although the model cannot predict the realistic magnitude and direction of the lattice distortion, it still leads to a proper description of the electronic behavior of manganites and surprisingly, it even gives rise to the correct critical temperature for the structural (orbital disorder-order) transition from dynamic to static Jahn-Teller effect in  $\text{LaMnO}_3$  (see the phase diagram in Fig. 4.1).

### 4.3.1 Lattice distortion

To study the dynamic Jahn-Teller effect, we define the probability distribution function  $P(Q)$  for the lattice distortion

$$Q = \frac{1}{L} \sum_i \sqrt{Q_2(\tau_i)^2 + Q_3(\tau_i)^2}, \quad \tau_i = \frac{i-1}{L} \beta. \quad (4.4)$$

Here we use  $dQ$  instead of  $QdQ$  as the phonon measure so that  $P(Q)$  represents the probability of the dynamic Jahn-Teller distortion in the range  $[Q, Q + dQ]$ , which can be easily calculated in the DMFT (QMC) calculations.

Let me note that for some reason, the symmetry between the two Jahn-Teller modes is broken in the QMC calculations once we introduce the Hubbard-Stratonovich transformation for the Coulomb interactions. The distribution functions of the two Jahn-Teller modes are thus very different. This phenomenon is stable with increasing temperature or QMC sweeps. However, the symmetry is recovered when the Coulomb interaction  $U$  or  $\Delta\tau$  goes to zero. In practice, we only need to do the averaging with respect to the orbital indices for electronic quantities such as the local Green's function which we are most interested in. Moreover, the DMFT results of the phonon distribution of  $Q_2$  and  $Q_3$  are not necessarily related to the realistic lattice distortion due to the simplification of the model (see below). Therefore, from now on, we will only focus on the probability distribution of the total lattice distortion  $Q$  defined in Eq. (4.4).

Fig. 4.9 plots the distribution function  $P(Q)$  for  $g = 0.05 \text{ eV}^{3/2}$  and  $\beta = 16$ . The the lattice distortion are converted into units of  $\text{\AA}$  by multiplying a factor of  $\hbar/\sqrt{M}$  where  $M$  is the mass of oxygen atom. We see that  $P(Q)$  has one broad peak located at around

$$\bar{Q} = \frac{\int dQ Q P(Q)}{\int dQ P(Q)} = 0.167 \text{ \AA}, \quad (4.5)$$

which agree roughly to  $Q^* = g/\Omega^2 \approx 0.15 \text{ \AA}$  for a single-site model (see section 2.2).

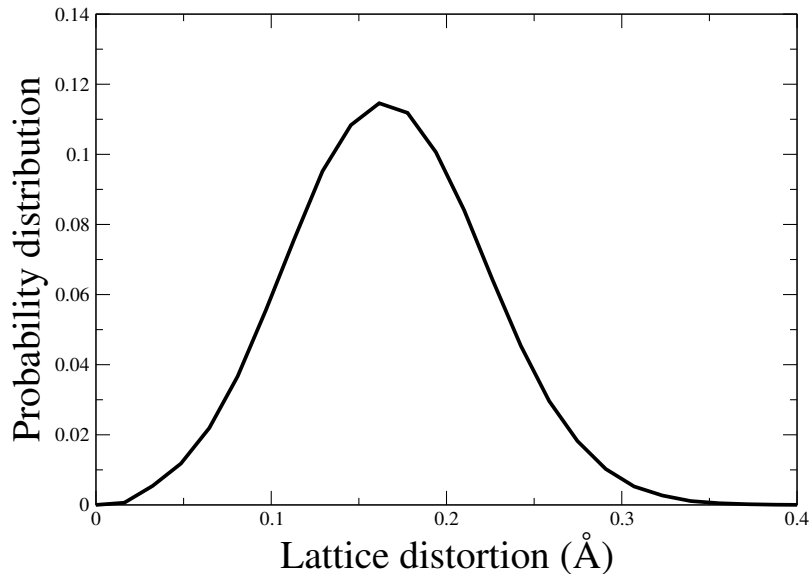


Figure 4.9: Probability distribution (in arbitrary unit) of the lattice distortion for the Jahn-Teller coupling  $g = 0.05 \text{ eV}^{3/2}$ , the  $e_g$  bandwidth  $W = 3.6 \text{ eV}$  and the inverse temperature  $\beta = 16$ . We have taken  $\Delta\tau = 0.2$  and  $L = 80$  in the DMFT calculations. The lattice distortion in units of  $\text{\AA}$  is obtained by multiplying a factor  $\hbar/\sqrt{M}$ , where  $M$  is the mass of oxygen atom.

Such a lattice distortion of the order of  $0.1 \text{ \AA}$  was once believed to be roughly in agreement with experimental results in early theoretical studies [Millis et al. 1996c, Satpathy et al. 1996a, Meskine & Satpathy 1999, Popovic & Satpathy 2000]. So a coupling  $g = 0.05 \text{ eV}^{3/2}$  has been generally used which leads to a Jahn-Teller energy

$$E_{JT} = \frac{g^2}{2\Omega^2} = 0.25 \text{ eV}, \quad (4.6)$$

consistent with some LDA calculations [Pickett&Singh 1996, Yin et al. 2006]. However, recent x-ray powder diffraction and neutron powder diffraction measurements found a much larger distortion of about  $0.4 \text{ \AA}$  [Chatterji et al. 2003]. The experimental results are shown in Fig. 4.10. In our model, the larger distortion is only possible if the Jahn-Teller phonons are much softer which, however, contradicts the Raman experiment [Iliev et al. 1998], or the Jahn-Teller coupling is extraordinary strong which leads to a larger Jahn-Teller energy in contradiction with the LDA calculations. Therefore, we suggest that the simple description of the electron-phonon interaction in our model cannot account for properly the realistic lattice distortions and we have to take into account higher order effects such as the cooperative lattice effect and the quadratic vibronic coupling to the electron degrees of freedom.

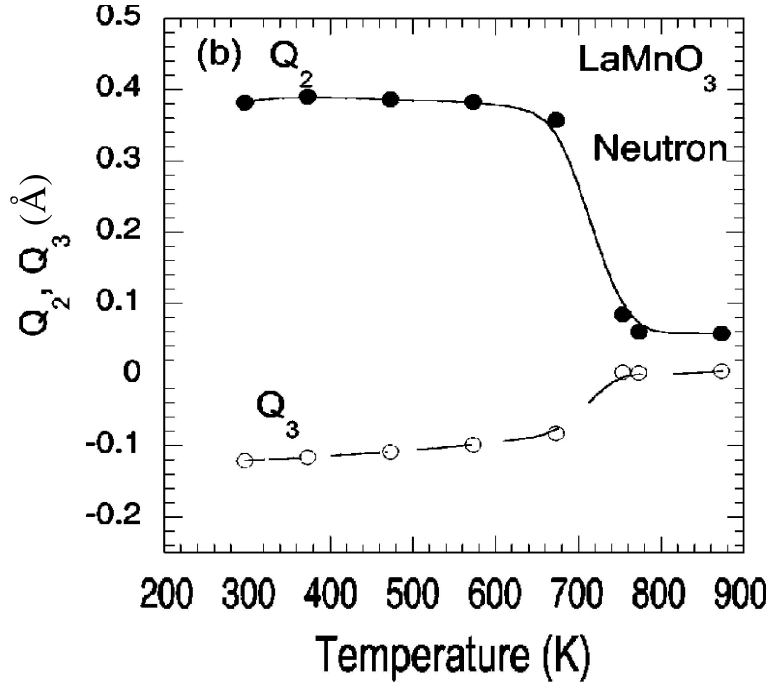


Figure 4.10: Static Jahn-Teller distortions as a function of temperature obtained from neutron powder diffraction measurements. Below the transition temperature 740 K,  $Q_2 = 0.39 \text{ \AA}$  and  $Q_3 = 0.12 \text{ \AA}$ . So the total distortion is  $Q = \sqrt{Q_2^2 + Q_3^2} = 0.4 \text{ \AA}$ , which is different from earlier estimates [Millis et al. 1996c, Satpathy et al. 1996a, Meskine & Satpathy 1999, Popovic & Satpathy 2000]. Figure taken from Ref. [Chatterji et al. 2003].

**Quadratic vibronic coupling and cooperative effect** The quadratic vibronic coupling to the electron degrees of freedom contributes to the Hamiltonian an additional term [Kanamori 1960, Popovic & Satpathy 2000]

$$H_{quad} = -G(Q_3^2 - Q_2^2)\tau^z + 2GQ_2Q_3\tau^x, \quad (4.7)$$

where  $G$  is a positive coupling constant and  $\tau^x, \tau^z$  are Pauli matrices describing the two  $e_g$  orbitals with  $|\uparrow\rangle = |3z^2 - r^2\rangle$  and  $|\downarrow\rangle = |x^2 - y^2\rangle$ . For an isolated octahedron,  $H_{quad}$  leads to the well-known "Mexican-hat" type potential with three minima in the  $Q_2$ - $Q_3$  plane along  $\phi \equiv \tan^{-1}(Q_2/Q_3) = 0, \pm 2\pi/3$  directions [Kanamori 1960].

The cooperative effect, on the other hand, comes from the fact that the adjacent  $\text{MnO}_6$  octahedra share a common oxygen atom in the  $\text{LaMnO}_3$  crystal. This adds to the lattice Hamiltonian a term [Popovic & Satpathy 2000]

$$H_{co} = K' \sum_{\langle ij \rangle_\alpha} \tilde{Q}_{i\alpha} \tilde{Q}_{j\alpha}, \quad (4.8)$$

where  $K'$  is a constant and  $\langle ij \rangle_\alpha$  denotes the adjacent octahedra along the direction  $\alpha = x, y$ , and  $z$ .  $\tilde{Q}_{i\alpha}$  are defined as

$$\tilde{Q}_x = \frac{Q_3 + \sqrt{3}Q_2}{2}, \quad \tilde{Q}_y = \frac{Q_3 - \sqrt{3}Q_2}{2}, \quad \tilde{Q}_z = Q_3. \quad (4.9)$$

This cooperative effect could modify the location of the energy minima in the  $Q_2$ - $Q_3$  plane [Popovic & Satpathy 2000].

We will not go into the detail here, but note that a recent LDA+U calculation [Yin et al. 2006] actually produced the correct experimental results, namely, the lattice distortion  $Q = 0.4 \text{ \AA}$  and the "orbital mixing angle"  $\phi = \tan^{-1}(Q_2/Q_3) = \pm 109^\circ$  which corresponds to the lattice distortion of the type  $(Q_2, Q_3; -Q_2, Q_3)$  for each two neighboring  $\text{MnO}_6$  octahedra in the  $a$ - $b$  plane of the orthorhombic  $\text{LaMnO}_3$  (see Fig. 4.4). The realistic "orbital mixing angle" is determined by and reflects the competition of the anharmonic terms of the potential energy and higher order couplings which favors  $\phi = 0, \pm 2\pi/3$  [Kanamori 1960], the tetragonal crystal field splitting which favors  $\phi = 0$  [Yin et al. 2006], the superexchange interaction which favors  $\phi = \pi/2$  (for the cubic structure) [Bala & Oleś 2000], as well as the kinetic motion of the  $e_g$  electrons and the cooperative Jahn-Teller contributions [Popovic & Satpathy 2000].

To properly describe the lattice distortion in the model calculations, we need to extend the model Hamiltonian (4.2) to include the cooperative effect and the higher order anharmonic contributions, etc. This is beyond our single-impurity DMFT (QMC) method and can only be treated in more sophisticated methods such as the cluster extensions of DMFT [Hettler et al. 1998, Lichtenstein & Katsnelson 2000, Kotliar et al. 2001, Potthoff et al. 2003, Kotliar et al. 2006].

### 4.3.2 Insulating ground state

Fig. 4.11 shows the spin- and orbital-averaged spectral density

$$A(\omega) = -\frac{1}{4\pi} \sum_{\mu\sigma} \text{Im} G^{\mu\sigma}(\omega) \quad (4.10)$$

in the paramagnetic phase obtained by the maximum entropy method. The Jahn-Teller coupling is taken as  $g = 0.05 \text{ eV}^{-3/2}$  and the  $e_g$  bandwidth  $W = 3.6 \text{ eV}$  ( $t_0 = 0.6 \text{ eV}$ ). Compared to the LDA+DMFT results in Fig. 4.6,  $A(\omega)$  has a similar three-peak structure. These peaks stem from the localized orbital and the states pushed up by the Hund's rule coupling and the Jahn-Teller splitting as already marked in Fig. 4.6.

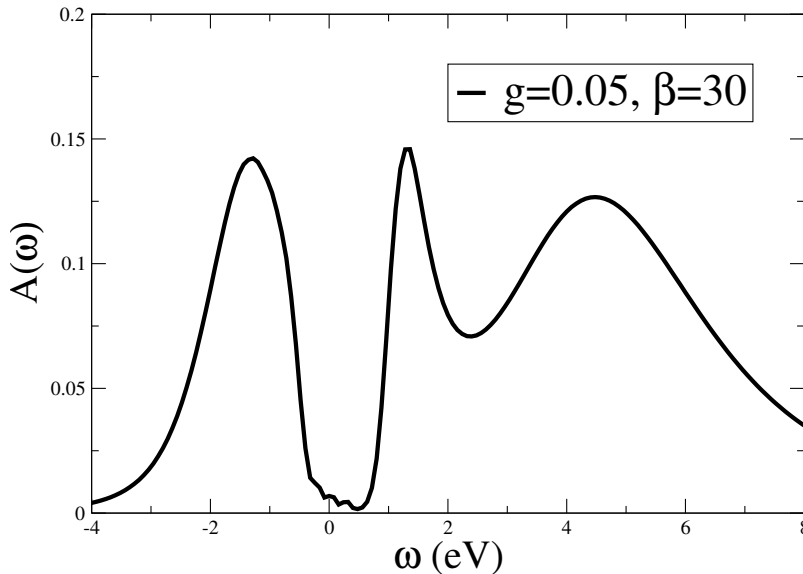


Figure 4.11: Local spectral density in the paramagnetic phase obtained from the maximum entropy method for  $g = 0.05 \text{ eV}^{-3/2}$ ,  $W = 3.6 \text{ eV}$  and  $\beta = 30$ . We use  $\Delta\tau = 0.25$  so that  $L = 120$  imaginary time slices are taken in the QMC samplings.

In Fig. 4.11, there is still some spectral weight in the gap which may stem from the phonon sideband [Edwards 2002]. The energy gap can hence only be obtained approximately. Fig. 4.12 plots the gap as a function of bandwidth for  $g = 0.04, 0.05, \text{ and } 0.06 \text{ eV}^{3/2}$ . The results can be compared with the experimental gap of about 1 eV [Jung et al. 1998, Takenaka et al. 1999]. We find that for  $U = 5 \text{ eV}$ , a Jahn-Teller coupling  $g = 0.04 - 0.05 \text{ eV}^{3/2}$  is required to account for the electronic properties of  $\text{LaMnO}_3$ . Such a coupling also gives rise to a critical bandwidth of 4.2 – 4.8 eV for the insulator-to-metal transition, consistent with the LDA+DMFT calculations. A larger coupling constant  $g = 0.06 \text{ eV}^{3/2}$  leads to a larger energy gap for  $W = 3.6 \text{ eV}$  and a larger critical bandwidth of 5.4 eV for the insulator-to-metal transition.

The consistency between the LDA+DMFT and DMFT model calculations supports our realistic microscopic model (4.2) for describing the electronic behavior of  $\text{LaMnO}_3$  and demonstrates once again that the insulating ground state in  $\text{LaMnO}_3$  at ambient conditions results from the combination of the Coulomb interaction and the Jahn-Teller coupling in addition to the Hund’s coupling between the  $e_g$  and  $t_{2g}$  spins.

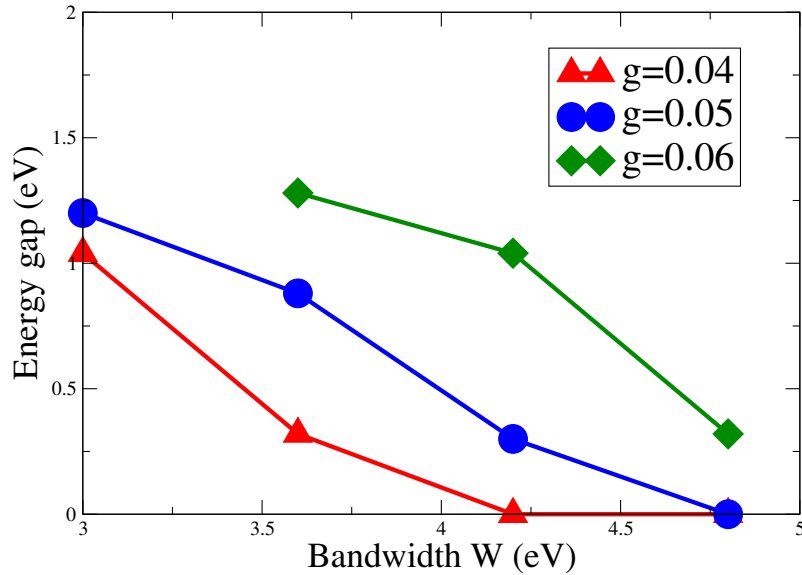


Figure 4.12: Energy gap as a function of bandwidth  $W$  for the Jahn-Teller coupling  $g = 0.04, 0.05, 0.06 \text{ eV}^{3/2}$  at  $\beta = 30$

### 4.3.3 Structural transition

As is shown in Fig. 4.10, the structural transition at  $T_{OO} \approx 740 \text{ K}$  is a first-order transition with an abrupt volume contraction [Chatterji et al. 2003]. The lattice is nearly cubic above  $T_{OO}$  but has a strongly distorted orthorhombic structure due to the static Jahn-Teller distortion below  $T_{OO}$ . The structural transition is accompanied by an orbital order-disorder transition. The low temperature phase shows a staggered ordering of  $d_{3x^2-r^2}$  and  $d_{3y^2-r^2}$  orbitals in the  $a$ - $b$  plane which repeats itself along the  $c$ -direction. With a slight modification of the single-impurity DMFT (QMC) algorithm, we can study a hypothetical antiferromagnetic orbital ordering on an  $AB$  lattice and draw some conclusions about the structural transition in  $\text{LaMnO}_3$ .

**$AB$  lattice** To study the antiferromagnetic orbital ordering, the cubic lattice is separated into two sublattices A and B with alternating  $e_g$  occupancy. Neglecting the orbital off-diagonal elements, the two orbital components of the local self-energy change from site to site so that

$$\Sigma_{\mu}^A(\omega) = \Sigma_{\bar{\mu}}^B(\omega), \quad (4.11)$$

which is equivalent to a uniform potential

$$\Sigma(\omega) = \begin{pmatrix} \frac{\Sigma_1^A(\omega) + \Sigma_2^A(\omega)}{2} & 0 \\ 0 & \frac{\Sigma_1^A(\omega) + \Sigma_2^A(\omega)}{2} \end{pmatrix} \quad (4.12)$$

plus a staggered potential

$$\Sigma'(\omega) = \begin{pmatrix} \frac{\Sigma_1^A(\omega) - \Sigma_2^A(\omega)}{2} & 0 \\ 0 & -\frac{\Sigma_1^A(\omega) - \Sigma_2^A(\omega)}{2} \end{pmatrix}. \quad (4.13)$$

In DMFT, they contribute to the effective action by a term

$$\sum_{i\mu\sigma} \left[ \Sigma_\mu(\omega) \left( c_{Ai\mu\sigma}^\dagger c_{Ai\mu\sigma} + c_{Bi\mu\sigma}^\dagger c_{Bi\mu\sigma} \right) + \Sigma'_\mu(\omega) \left( c_{Ai\mu\sigma}^\dagger c_{Ai\mu\sigma} - c_{Bi\mu\sigma}^\dagger c_{Bi\mu\sigma} \right) \right], \quad (4.14)$$

where we use subscript A and B for the fermionic operators on A and B sublattices respectively. In momentum space, Eq. (4.14) becomes

$$\sum_{\mathbf{k} \in \frac{1}{2}\mathcal{BZ}, \mu\sigma} \left[ \Sigma_\mu(\omega) \left( c_{\mathbf{k}\mu\sigma}^\dagger c_{\mathbf{k}\mu\sigma} + c_{\mathbf{k}+\mathbf{Q}\mu\sigma}^\dagger c_{\mathbf{k}+\mathbf{Q}\mu\sigma} \right) + \Sigma'_\mu(\omega) \left( c_{\mathbf{k}\mu\sigma}^\dagger c_{\mathbf{k}+\mathbf{Q}\mu\sigma} + c_{\mathbf{k}+\mathbf{Q}\mu\sigma}^\dagger c_{\mathbf{k}\mu\sigma} \right) \right], \quad (4.15)$$

where  $\mathbf{Q} = (\pi, \pi, \pi)$  and  $\mathbf{k}$  is summed over half of the original Brillouin zone.

Note that  $\Sigma'_\mu(i\omega_n)$  mixes the two momentum states  $|\mathbf{k}\rangle$  and  $|\mathbf{k} + \mathbf{Q}\rangle$  so that we have to take into account the momentum off-diagonal Green's function

$$G_{\mathbf{k}, \mathbf{k}+\mathbf{Q}}^{\mu\sigma}(\tau) = -\langle \mathcal{T} c_{\mathbf{k}\mu\sigma}(\tau) c_{\mathbf{k}+\mathbf{Q}\mu\sigma}^\dagger(0) \rangle. \quad (4.16)$$

The equation of motion for the Green's function has the form:

$$\begin{pmatrix} F_{\mathbf{k}}(i\omega_n) & -\Sigma'(i\omega_n) \\ -\Sigma'(i\omega_n) & F_{\mathbf{k}+\mathbf{Q}}(i\omega_n) \end{pmatrix} \begin{pmatrix} G_{\mathbf{k}}(i\omega_n) & G_{\mathbf{k}, \mathbf{k}+\mathbf{Q}}(i\omega_n) \\ G_{\mathbf{k}+\mathbf{Q}, \mathbf{k}}(i\omega_n) & G_{\mathbf{k}+\mathbf{Q}}(i\omega_n) \end{pmatrix} = \begin{pmatrix} \mathcal{I} & 0 \\ 0 & \mathcal{I} \end{pmatrix}, \quad (4.17)$$

where  $\mathcal{I}$  is the  $2 \times 2$  unit matrix and the spin and orbital indices are suppressed to simplify the notations.  $F_{\mathbf{k}}(i\omega_n)$  is a  $2 \times 2$  matrix defined as

$$F_{\mathbf{k}}(i\omega_n) = (i\omega_n + \mu)\mathcal{I} - \epsilon_{\mathbf{k}} - \Sigma(i\omega_n). \quad (4.18)$$

Solving the equation yields

$$\begin{aligned} G_{\mathbf{k}, \mathbf{k}+\mathbf{Q}}(i\omega_n) &= F_{\mathbf{k}}(i\omega_n)^{-1} \Sigma'(i\omega_n) G_{\mathbf{k}+\mathbf{Q}}(i\omega_n), \\ G_{\mathbf{k}+\mathbf{Q}, \mathbf{k}}(i\omega_n) &= F_{\mathbf{k}+\mathbf{Q}}(i\omega_n)^{-1} \Sigma'(i\omega_n) G_{\mathbf{k}}(i\omega_n), \end{aligned} \quad (4.19)$$

and

$$\begin{aligned} G_{\mathbf{k}}(i\omega_n) &= [F_{\mathbf{k}}(i\omega_n) - \Sigma'(i\omega_n)F_{\mathbf{k}+\mathbf{Q}}(i\omega_n)^{-1}\Sigma'(i\omega_n)]^{-1}, \\ G_{\mathbf{k}+\mathbf{Q}}(i\omega_n) &= [F_{\mathbf{k}+\mathbf{Q}}(i\omega_n) - \Sigma'(i\omega_n)F_{\mathbf{k}}(i\omega_n)^{-1}\Sigma'(i\omega_n)]^{-1}. \end{aligned} \quad (4.20)$$

The local Green's functions are then

$$\begin{aligned} G_A^{\mu\sigma}(i\omega_n) &= -\langle \mathcal{T} c_{A\mu\sigma}(\tau) c_{A\mu\sigma}^\dagger(0) \rangle_{i\omega_n} \\ &= \frac{1}{\mathcal{V}} \sum_{\mathbf{k} \in \frac{1}{2}\mathcal{BZ}} [G_{\mathbf{k}}^{\mu\sigma}(i\omega_n) + G_{\mathbf{k}+\mathbf{Q}}^{\mu\sigma}(i\omega_n) + 2G_{\mathbf{k},\mathbf{k}+\mathbf{Q}}^{\mu\sigma}(i\omega_n)], \\ G_B^{\mu\sigma}(i\omega_n) &= -\langle \mathcal{T} c_{B\mu\sigma}(\tau) c_{B\mu\sigma}^\dagger(0) \rangle_{i\omega_n} \\ &= \frac{1}{\mathcal{V}} \sum_{\mathbf{k} \in \frac{1}{2}\mathcal{BZ}} [G_{\mathbf{k}}^{\mu\sigma}(i\omega_n) + G_{\mathbf{k}+\mathbf{Q}}^{\mu\sigma}(i\omega_n) - 2G_{\mathbf{k},\mathbf{k}+\mathbf{Q}}^{\mu\sigma}(i\omega_n)]. \end{aligned} \quad (4.21)$$

In the simple case  $\epsilon_{\mathbf{k}}^{\mu\nu} = \epsilon_{\mathbf{k}}\delta_{\mu\nu}$ , we recover the familiar result

$$G_{A/B}^{\mu\sigma}(i\omega_n) = \frac{\zeta_{\mu}^{A/B}}{\mathcal{V}} \sum_{\mathbf{k} \in \mathcal{BZ}} \frac{1}{\zeta_{\mu}^A \zeta_{\mu}^B - \epsilon_{\mathbf{k}}^2}, \quad (4.22)$$

where  $\zeta_{\mu}^{A/B} = i\omega_n + \mu - \Sigma_{\mu}^{A/B}(\omega)$ . We find

$$G_A^{\mu\sigma}(i\omega_n) = G_B^{\bar{\mu}\sigma}(i\omega_n), \quad (4.23)$$

indicating the alternating occupancy of the  $e_g$  orbitals on the lattice.

Therefore, in the DMFT calculations, we only need to take care of a single lattice site of either type (say A). Once the local Green's function is obtained from Eqs. (4.20) and (4.21), the effective Weiss field can be calculated from the Dyson equation

$$\mathcal{G}_A^0(\omega) = [G_A(\omega) + \Sigma^A(\omega)]^{-1}. \quad (4.24)$$

The Coulomb interaction and the Jahn-Teller phonons are then treated on a single site (type A) in QMC. After the DMFT convergence, the orbital symmetry breaking can be easily seen from the orbital polarization

$$P = \left| \sum_{\sigma} (n_{1\sigma}^A - n_{2\sigma}^A) \right|. \quad (4.25)$$

If  $P = 0$ , there is no symmetry breaking and the orbitals are disordered. If  $P \neq 0$ , then the two  $e_g$  orbitals are differently occupied, the orbital symmetry is broken and there exists a finite static Jahn-Teller distortion. Below we discuss the electronic behavior of the realistic model on an  $AB$  lattice.



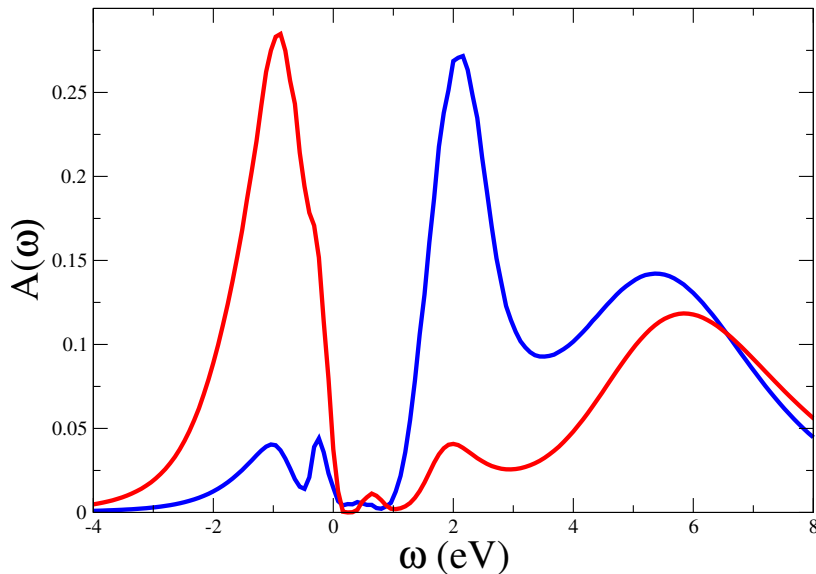


Figure 4.13: Local spectral density for the antiferromagnetic orbital ordering calculated by DMFT (QMC). The parameters are  $W = 3.6$  eV,  $T = 0.05$  eV and  $g = 0.05$  eV<sup>3/2</sup>.

**Electronic behavior** Fig. 4.13 shows the local spectral densities of two  $e_g$  orbitals for  $W = 3.6$  eV,  $T = 0.05$  eV and  $g = 0.05$  eV<sup>3/2</sup>. The orbital symmetry is strongly broken. The occupation number of one orbital is close to one, while the other orbital is only slightly occupied. Fig. 4.13 also indicates the contributions from different spin and orbital components. The two peaks at  $-1$  eV and  $2$  eV stem from the spin states parallel to the local  $t_{2g}$  spins. They are split by the Jahn-Teller coupling. Other spectral weights are pushed to higher energies by the Hund's coupling and the strong on-site Coulomb repulsion. However, the average spectral density is consistent with our earlier results (see Fig. 4.6 and Fig. 4.11).

Fig. 4.14 plots the orbital polarization as a function of bandwidth and temperature. For  $W = 3.6$  eV, we find a finite orbital polarization below  $T \approx 725$  K, in agreement with the experimental result of the structural transition temperature  $T_{OO} = 740$  K [Chatterji et al. 2003].

If we fix the temperature  $T = 0.05$  eV, the orbital polarization is almost a constant for the bandwidth  $W < 4.8$  eV and then decreases with increasing bandwidth until it is reduced to zero at  $W = 6.0$  eV. Such a behavior reflects the nature of the bandwidth-control metal-insulator transition in LaMnO<sub>3</sub>.  $W = 4.8$  eV corresponds to the critical bandwidth where the split minority and majority  $e_g$  bands start to overlap. So for larger bandwidth, the orbital polarization decreases rapidly with increasing bandwidth. The spectral weight at  $\omega = 0$  is no longer zero and the system becomes metallic. Below 4.8 eV, the orbital polarization remains constant

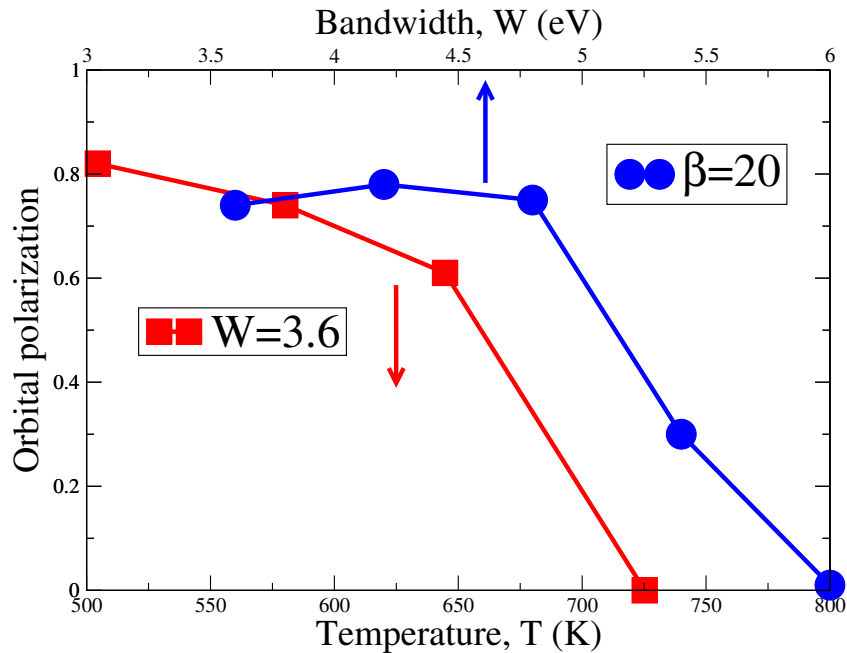


Figure 4.14: Orbital polarization versus temperature for  $W = 3.6$  eV (red curve) and bandwidth for  $T = 0.05$  eV (blue curve). The Jahn-Teller coupling is  $g = 0.05$  eV<sup>3/2</sup>.

since the two  $e_g$  bands are well separated.

The bandwidth  $W = 6.0$  eV marks a second transition where the orbital polarization and the Jahn-Teller distortion are completely suppressed. Although different from Ref. [Loa et al. 2001], we can still identify three distinct regimes at low temperature: (i) an insulating phase with orbital ordering and static Jahn-Teller distortion below  $W \approx 4.8$  eV (or  $P_{IM} = 32$  GPa); (ii) an intermediate metallic phase with orbital ordering and static Jahn-Teller distortion below  $W \approx 6$  eV; (iii) a metallic phase with orbital symmetry and dynamic Jahn-Teller distortion above  $W \approx 6$  eV. Following Ref. [Loa et al. 2001, Chatterji et al. 2003], they can be examined by x-ray and neutron powder diffraction and electrical resistivity measurements.

## 5 Doped manganites

We are interested in the extraordinary property of colossal magnetoresistance found over a wide range of doping in perovskite manganites. In  $\text{La}_{1-x}\text{Sr}_x\text{MnO}_3$ , the colossal magnetoresistance has been observed to be most pronounced around the Curie temperature for doping  $0.15 < x < 0.2$  [Tokura et al. 1994] where the system undergoes a metal-insulator transition as shown in Fig. 1.2. This suggests a strong connection between the electronic and magnetic properties of manganites.

Theoretically, the low temperature ferromagnetic metallic phase has been qualitatively explained by the double exchange mechanism [Zener 1951a, Zener 1951b]. However, the high temperature paramagnetic insulating phase is not yet fully understood. Since the first reports of the colossal magnetoresistance [Chahara et al. 1993, von Helmolt et al. 1993, Jin et al. 1994], considerable theoretical and experimental efforts have been devoted to the understanding of the unusual electronic properties of doped manganites such as the pseudo-gap behavior in the insulating-like phase. On the theoretical side, the paramagnetic insulating behavior has been attributed to the formation of orbital [Kilian & Khaliullin 1998, Horsch et al. 1999] or lattice polarons [Röder et al. 1996, Millis et al. 1996a], as well as Anderson localization [Varma 1996] and electronic phase separation/percolation [Yunoki et al. 1998, Moreo et al. 2000, Mayr et al. 2001]. On the experimental side, the optical properties have been intensively investigated and discussed based on qualitative pictures [Okimoto et al. 1995, Okimoto et al. 1997, Quijada et al. 1998, Jung et al. 1998, Takenaka et al. 1999]. The lattice structures have also been carefully analyzed [Elemans et al. 1971, Hibble et al. 1999].

These studies help to clarify the nature of the paramagnetic insulating phase. However, a quantitative and complete picture is still needed. As shown in the last chapter, the Coulomb interaction and the Jahn-Teller coupling are both indispensable. They are, however, always treated separately due to the numerical difficulties. Also, we still lack the knowledge of the values of the most relevant parameters, namely, the Coulomb interaction  $U$  and the Jahn-Teller coupling  $g$ . Very different estimates of these parameters can be found in the literature [Bocquet et al. 1992, Pickett & Singh 1996, Satpathy et al. 1996a, Satpathy et al. 1996b, Zampieri et al. 1998, Perebeinos & Allen 2000, Popovic & Satpathy 2000].

In this chapter, we try to go one step further and make a detailed numerical analy-

sis based on the DMFT (QMC) calculations of the realistic microscopic model (4.2). We will see that the model describes the physics of doped manganites. This allows for a quantitative comparison between the DMFT calculations and the experimental data of  $\text{LaMnO}_3$  and  $\text{La}_{1-x}\text{Sr}_x\text{MnO}_3$  and hence a plausible estimate of the Coulomb interaction  $U$  and the Jahn-Teller coupling  $g$ .

The chapter is organized as follows: In section 5.1, we discuss qualitatively the optical properties of doped manganites. The DMFT results for the realistic microscopic model are presented in section 5.2. By comparing the DMFT results with experiment, we devote section 5.3 to a new estimate of the parameters. The comparison also reveals some discrepancies which require further investigations.

## 5.1 Experiments

In the last decade, the experimental study of the electronic properties of doped manganites has made substantial progresses. The phase diagrams of many compounds have been established from resistivity measurements [Tokura et al. 1996, Tokura & Tomioka 1999, Salamon & Jaime 2001, Dagotto et al. 2001]. In optical experiments, a pseudo-gap behavior is found in the high temperature insulating phase [Okimoto et al. 1995, Okimoto et al. 1997, Quijada et al. 1998, Jung et al. 1998, Takenaka et al. 1999], leading to various theoretical suggestions. In the following, we will first discuss some of these experiments in order to get an impression of the physics of doped manganites before we perform the numerical calculations in the next section.

**Colossal magnetoresistance** Fig. 5.1(a) plots the doping dependence of the resistivity as a function of temperature for  $\text{La}_{1-x}\text{Sr}_x\text{MnO}_3$  [Urushibara et al.1995]. Above the Curie temperature  $T_c$ , the resistivity ( $\rho(T)$ ) shows an insulating behavior ( $d\rho(T)/dT < 0$ ) for small doping  $x < 0.3$  but becomes metallic ( $d\rho(T)/dT > 0$ ) for larger doping. Below  $T_c$ , the system is more metallic with an insulating behavior only for  $x < 0.175$ . The results are summarized in the phase diagram (Fig. 1.2). A metal-insulator transition occurs at  $T_c$  over a doping range ( $0.175 \leq x \leq 0.25$ ) with an abrupt change of the resistivity. When an external magnetic field is applied, a large magnetoresistance is observed near  $T_c$  in this doping range.

Fig. 5.1(b) shows the magnetic field dependence of the resistivity at doping  $x = 0.175$ . The magnetic field enhances the Curie temperature and turns the insulating behavior at  $T_c$  into a metallic behavior. A large magnetoresistance  $\eta' \approx 6$  is found under 15 T [Tokura et al. 1994]. The effect can be even stronger in the manganites with a smaller  $T_c$  such as  $\text{Pr}_{1-x}\text{Ca}_x\text{MnO}_3$  (see, e.g., Ref. [Dagotto et al. 2001]).

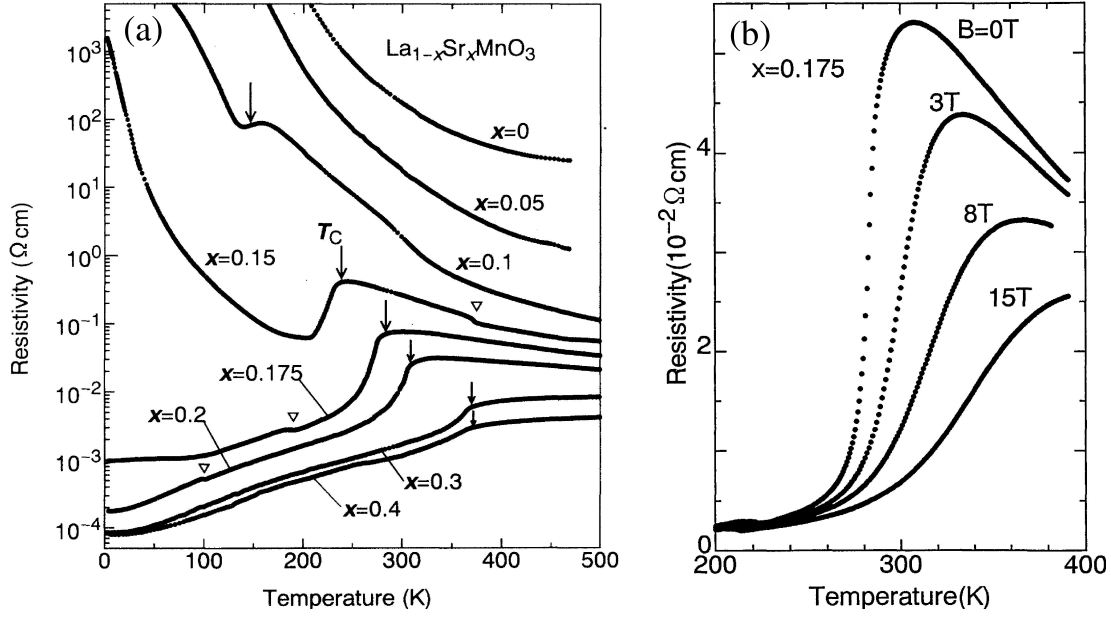


Figure 5.1: (a) Doping dependence of the resistivity as a function of temperature in  $\text{La}_{1-x}\text{Sr}_x\text{MnO}_3$  crystal. Arrows indicate the critical temperature  $T_c$  of the ferromagnetic transition. Open triangles indicate the anomalies due to the structural transition (corresponding to  $T_s$  in Fig. 4.1). Figure taken from Ref. [Urushibara et al.1995]. (b) Magnetic field dependence of the resistivity as a function of temperature in  $\text{La}_{0.825}\text{Sr}_{0.175}\text{MnO}_3$  crystal. Figure taken from Ref. [Tokura et al. 1994].

Thus the CMR effect and the large drop of resistivity at  $T_c$  must be related to the unusual electronic properties such as the high temperature insulating behavior in doped manganites. If the insulating phase was understood, the CMR, as well as the metal-insulator transition at  $T_c$  over the doping range of  $0.175 \leq x \leq 0.25$  in  $\text{La}_{1-x}\text{Sr}_x\text{MnO}_3$ , could simply be described as a result of the ferromagnetic transition.

**Optical conductivity** Fig. 5.2 shows the optical conductivity at room temperature (295 K) obtained from the reflectivity spectra measured on the cleaved surfaces of  $\text{La}_{1-x}\text{Sr}_x\text{MnO}_3$  [Takenaka et al. 1999]. The insulator-metal phase boundary lies between the doping  $x=0.175$  and  $0.20$ . The compound is an insulator in the doping range of  $0 \leq x < 0.175$  and a metal at  $x = 0.3$ . We find that:

- The low energy optical conductivity is strongly suppressed in the insulating phase ( $x = 0.1, 0.15, 0.175$ ). A Drude peak is only present deep into the metallic region at large doping ( $x > 0.3$ ).
- The optical conductivity has two peaks in the insulating phase. The low energy

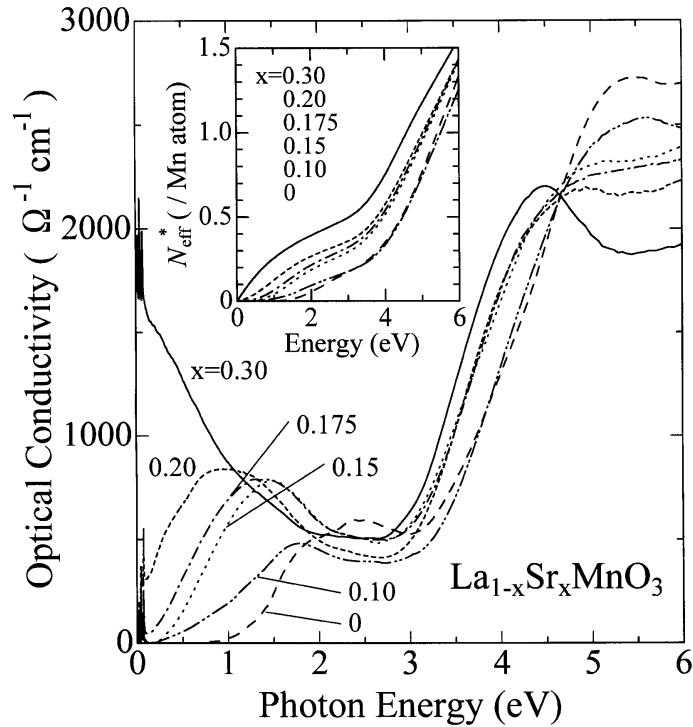


Figure 5.2: Optical conductivity of  $\text{La}_{1-x}\text{Sr}_x\text{MnO}_3$  at room temperature (295 K) for different dopings:  $x=0$  (long-dashed line), 0.10 (dashed-and-double-dotted line), 0.15 (dotted line), 0.175 (dashed-and-dotted line), 0.20 (short-dashed line), and 0.30 (solid line). Inset: Effective carrier number per Mn-atom  $N_{eff}^*(\omega)$  defined as the integration of  $\sigma(\omega)$ , see Eq. (3.107).  $T_C = 235$  K ( $x = 0.15$ ), 283 K (0.175), 305 K (0.20), and 362 K (0.30). The insulator-metal phase boundary lies between  $x = 0.175$  and 0.20. Figure taken from Ref. [Takenaka et al. 1999].

peak locates at  $\omega \approx 1 - 2$  eV and shifts toward lower energies with increasing doping. The high energy peak locates at about  $\omega \approx 6$  eV.

Such an optical conductivity suggests a pseudo-gap which has been observed in  $\text{La}_{1-x}\text{Ca}_x\text{MnO}_3$  ( $x \sim 0.3$ ) by scanning tunneling spectroscopy [Fäth et al. 1999]. With increasing doping, the system becomes more and more metallic and the pseudo-gap is gradually filled. An external magnetic field is expected to have the same effect.

Fig. 5.3 shows the optical conductivity in  $\text{La}_{1-x}\text{Sr}_x\text{MnO}_3$  as a function of temperature [Okimoto et al. 1995, Okimoto et al. 1997]. With decreasing temperature, the low energy part of the optical spectra is less suppressed. However, the spectrum is very different for different dopings. It remains insulating-like at  $x = 0.1$  but has a broad Drude peak at  $x = 0.3$ . In between ( $x = 0.175$ ), the spectrum is almost constant in the frequency range below 1 eV.

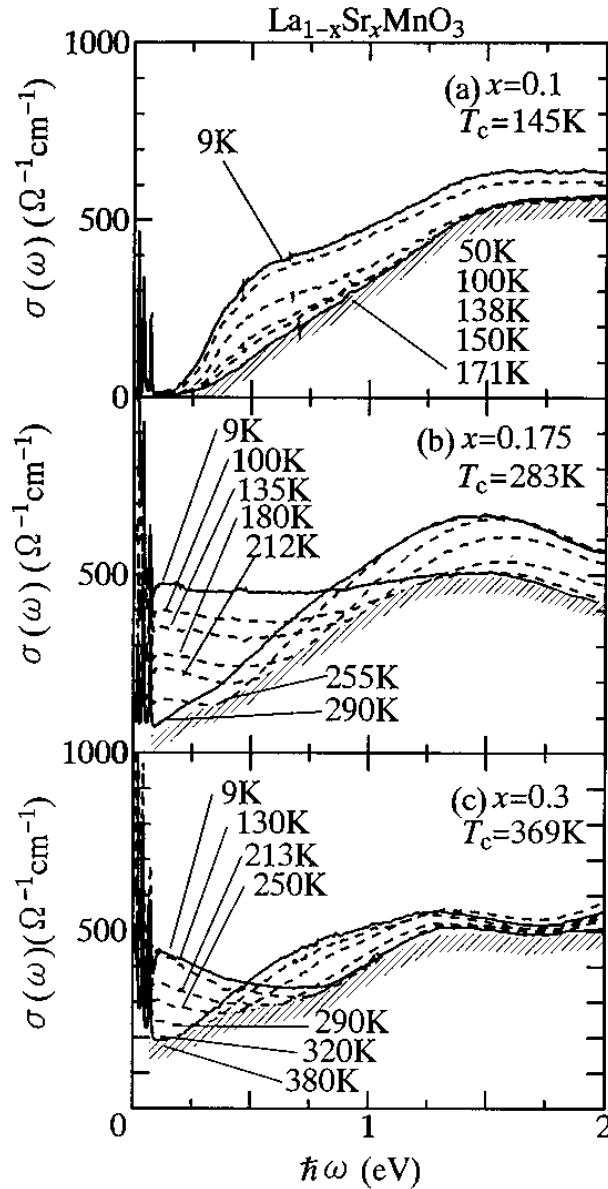


Figure 5.3: Temperature dependence of the optical conductivity in  $\text{La}_{1-x}\text{Sr}_x\text{MnO}_3$  at doping  $x=0.1$  (a),  $0.10$  (b) and  $0.3$  (c). The hatched curves represent the temperature independent parts of the spectra deduced from the envelope of the respective curves. Figure taken from Ref. [Okimoto et al. 1997].

Since the  $t_{2g}$  and  $e_g$  spins are almost fully polarized at  $T \ll T_c$ , the unusual feature at  $x = 0.175$  implies the existence of scattering mechanisms other than the spin disorder. It is the combination of these additional mechanisms and the spin scattering that results in the insulating behavior in the high temperature paramagnetic phase.

Without spin scattering (below  $T_c$ ), these additional mechanisms lead to a "bad" metal in  $\text{La}_{0.825}\text{Sr}_{0.175}\text{MnO}_3$ . As discussed in chapter 2, both the on-site Coulomb interaction and the Jahn-Teller coupling can give rise to additional scatterings of the  $e_g$  conduction electrons. The question is, of course, whether their effects are strong enough to account for the unusual behavior of the optical spectra of doped manganites. In the next section, we will study this issue based on DMFT (QMC) calculations of our realistic microscopic model.

## 5.2 DMFT model calculations

In the section, we present the DMFT calculations for doped manganites. Part of the work is contained in the preprint [Yang & Held 2006]. The Hamiltonian is again given by

$$\begin{aligned}
H = & - \sum_{\langle\langle ij \rangle\rangle; \mu\nu\sigma} t_{\mu\nu}^{ij} c_{i\mu\sigma}^\dagger c_{j\nu\sigma} - 2J \sum_{i;\mu} \mathbf{s}_{i\mu} \cdot \mathbf{S}_i \\
& + U \sum_{i;\mu} n_{i\mu\uparrow} n_{i\mu\downarrow} + \sum_{i;\sigma\bar{\sigma}} (V - \delta_{\sigma\bar{\sigma}} F) n_{i1\sigma} n_{i2\bar{\sigma}} \\
& - g \sum_{i;\mu\nu\sigma} c_{i\mu\sigma}^\dagger (Q_{2i}\tau^x + Q_{3i}\tau^z)_{\mu\nu} c_{i\nu\sigma} + \sum_{i;a} \left( \frac{P_{ai}^2}{2} + \frac{\Omega^2}{2} Q_{ai}^2 \right). \quad (5.1)
\end{aligned}$$

The hopping integral  $t_{\mu\nu}^{ij}$  is given by Eq. (2.23). The parameters are taken as:  $W = 3.6$  eV from the LDA calculations for the cubic structure,  $2J\mathbf{S} = 2.66$  eV from the constrained LDA calculations,  $U = 5$  eV,  $F = 0.75$  eV, and  $V = U - 2F = 3.5$  eV estimated from Ref. [Park et al. 1996], and  $\Omega = 0.07$  eV from Raman spectroscopy [Iliev et al. 1998]. The Jahn-Teller coupling  $g$  is assumed to be a free parameter.

As for the undoped system, we first discuss the probability distribution of the lattice distortion in section 5.2.1. The DMFT results for the electron spectral density are presented in section 5.2.2. Based on these results, the optical conductivity (section 5.2.3) and the Curie temperature (section 5.2.4) are calculated and compared with experiments, which allows us to conclude that the Jahn-Teller coupling and the Coulomb interaction can actually explain the optical experiments discussed in the last section.

### 5.2.1 Lattice distortion

Fig. 5.4 plots the probability distribution of the lattice distortion for  $n = 0.8$  ( $x = 0.2$ ) at different temperatures and couplings. Unlike the single peak distribution obtained for the undoped case in section 4.3.1, we find two peaks in the distribution



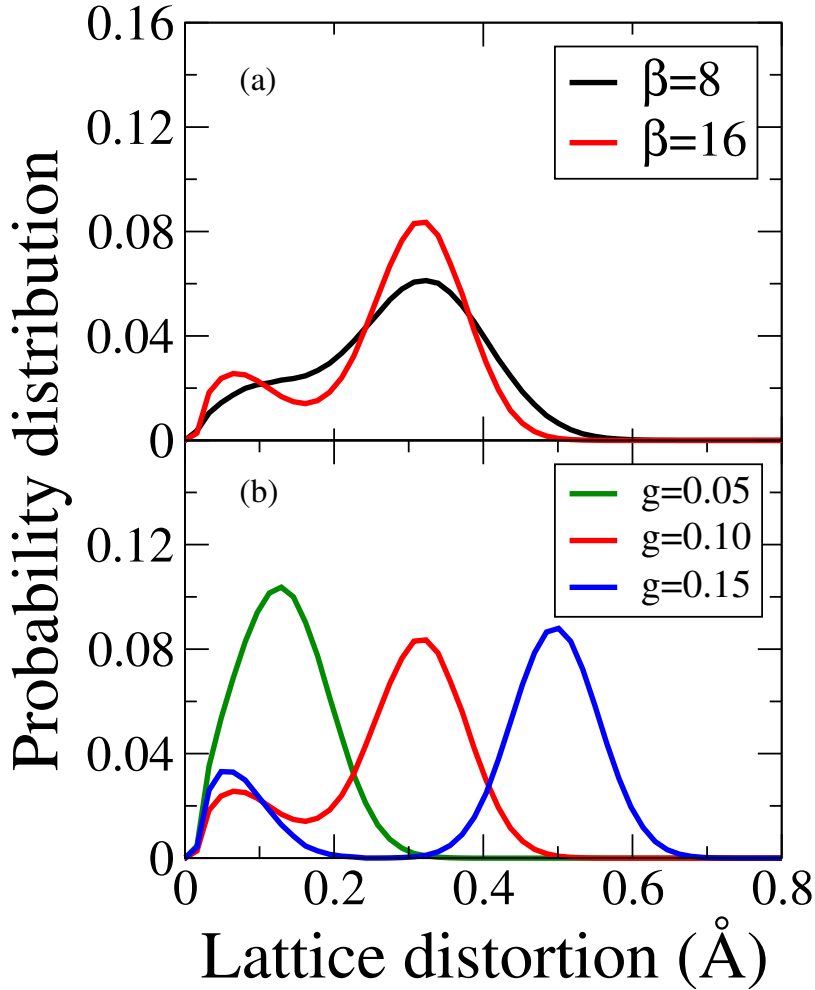


Figure 5.4: Probability distribution of the lattice distortion at  $n = 0.8$  ( $x = 0.2$ ) for: (a)  $g = 0.10$  and  $\beta = 8$  and 16; (b)  $\beta = 16$  and  $g = 0.05, 0.10,$  and  $0.15$ .

function at large Jahn-Teller couplings for doped systems. The large peak located at about  $g/\Omega^2$  corresponds to the large lattice distortion due to the Jahn-Teller coupling, while the small peak stems from the quantum and thermal fluctuation of the  $\text{MnO}_6$  octahedra which do not couple to  $e_g$  electrons because of doping. For a weak coupling  $g = 0.05$ , the two peaks are merged together. With increasing  $g$ , the structure gradually shows up and the two peaks become well separated for a strong coupling  $g = 0.15$ .

The position of the large distortion peak and its coupling dependence can be easily understood from the single-site model (2.8), in which the static lattice distortion locates approximately at  $g/\Omega^2$ , while the position of small distortion peak remains independent of the coupling  $g$  as shown in Fig. 5.4(b). Thus for a small  $g$ , the two

peaks are overlapping. It is only for strong couplings such as  $g = 0.10$  and  $0.15$  that the two peaks can be separated and the separation increases linearly with the coupling constant  $g$ . The temperature dependence of the probability distribution in Fig. 5.4(a) can be understood by the reduction of the thermal vibration which narrows both peaks and thus enhances their separation at low temperatures.

The separation of the two peaks in the probability distribution makes it difficult for the QMC sampling at low temperature or for strong Jahn-Teller coupling. The important configurations locate in two separated regions in the configuration space of the Jahn-Teller phonons. It is almost impossible to update the phonon fields from one region to the other. To obtain a good QMC sampling, we would have to use special methods [Swendsen & Wang 1986, Moreno et al. 2003, Earl & Deem 2005]. Unfortunately, these special methods often require a bigger computational effort.

One way out is to assign a relative probability  $\mathcal{P}_a$  to each separated region  $a$  at low temperature (e.g.,  $\beta = 30$ ) or for strong Jahn-Teller coupling ( $g > 0.12$ ). We then sample each region separately and average the results according to the assigned probabilities. Note that in Fig. 5.4(a), the distribution function shows a low temperature limit. Therefore, we can obtain the assigned probabilities by extrapolating the high temperature results which do not lead to numerical problems in the QMC simulations. In fact, we find

$$\mathcal{P}_c = 1 - n = x, \quad (5.2)$$

where  $\mathcal{P}_c$  is the relative probability of the lattice distortion between  $[0, g/2\Omega^2]$ . Fig. 5.5 plots the calculated  $\mathcal{P}_c$  as a function of doping at  $\beta = 8$  and  $16$ . With decreasing temperature, the results approach Eq. (5.2).

The physical background of the above approximation is the localization of the  $e_g$  electrons. For strong Jahn-Teller coupling, the local property of the system can be approximately described by a single-site model. The conduction electrons are completely localized by the large lattice distortion so that the probability of the large distortion region in the distribution function should be approximately equal to the electron occupation number  $n$ . This explains Eq. (5.2).

In the lattice model, the above discussion suggests a relation between the structure of the distribution function and the electron spectrum. Fig. 5.6 compares the distribution of the lattice distortion and the corresponding electron spectral densities. For clarity, we separate the spectrum into two parts originated from the large and small lattice distortions, respectively. For the large lattice distortion, the corresponding spectral density locates well below or far above the Fermi energy. The low energy part can be identified as localized  $e_g$  electrons, while the high energy part stems from the states which are pushed up by the Hund's rule coupling, the

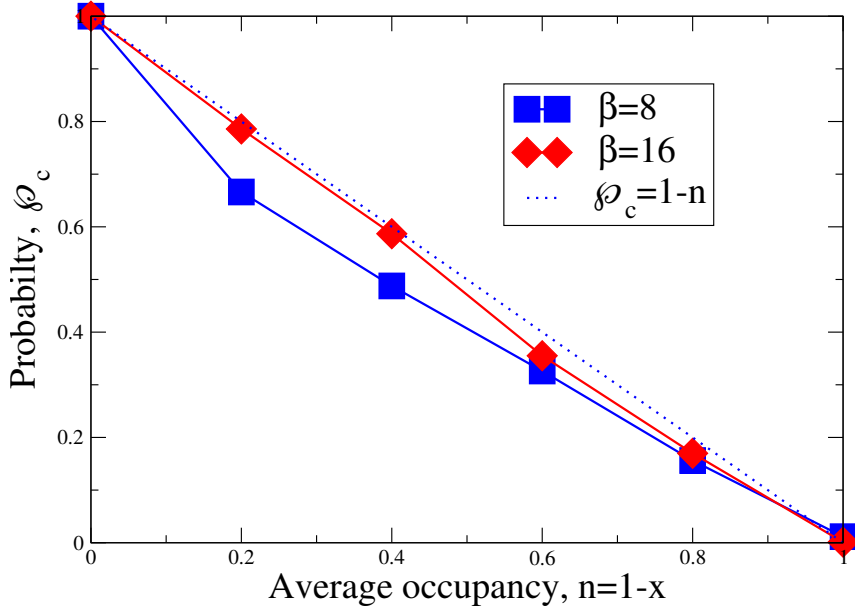


Figure 5.5: Probability of the lattice distortion between  $[0, g/2\Omega^2]$  in the distribution function of the lattice distortion versus the average occupation number  $n$ . The parameters are  $\beta = 8, 16$  and  $g = 0.10$ . These high temperature results can be extrapolated to give the low temperature probability of each peak in the distribution function.

Jahn-Teller splitting and the Coulomb repulsion. For the small lattice distortion, most of the spectral density locates slightly above the Fermi energy. They stem from the "undistorted" unoccupied states which are also called "midgap states" in the literature [Millis et al. 1996a, Jung et al. 1998].

We note that a very similar (two maxima) distribution of the averaged Ising-like field is observed for the DMFT Mott insulator, where it indicates the presence of a localized spin (up or down); and the slow QMC dynamics from spin up to down reflects the long-time stability of the spins in the Mott-insulating phase of the Hubbard model. Thus the slow dynamics from large (small) lattice distortion to small (large) lattice distortion may also indicate a long-time stability of the lattice distortion in real material. This is exactly the lattice polaron picture. The electrons are trapped as lattice polarons by the large lattice distortion. The spectral density of the  $e_g$  electrons can be regarded as a combination of the polaron states and the midgap states.

The separation the spectrum into the polaron states and the midgap states leads to an effective two-band model as was discussed in Ref. [Ramakrishnan et al. 2004], where it was assumed that the low-energy  $e_g$  band separates into a localized band below the Fermi energy and a delocalized band which dominates the transport prop-

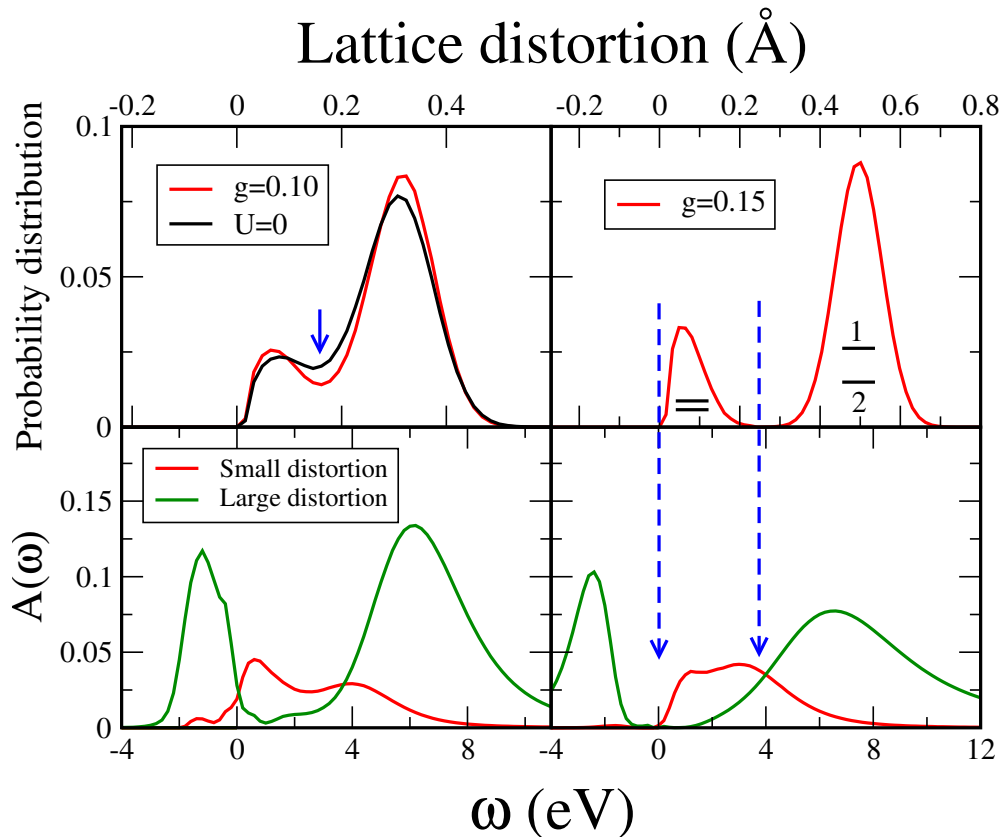


Figure 5.6: Probability distribution of the lattice distortion and the corresponding electron spectral densities for the Jahn-Teller coupling  $g = 0.10$  (left panel) and  $0.15$  (right panel) at inverse temperature  $\beta = 16$ . The electron spectral densities are separated into two parts with large and small lattice distortions. The arrows indicate the separation between peaks. The phonon distribution at  $g = 0.10$  without the Coulomb interaction is also shown for comparison.

erties of doped manganites. This model neglects the hybridization of the two kind of states. According to our results, it is valid only if we focus on the low energy electronic behavior of the system and the Jahn-Teller coupling is strong enough so that the  $e_g$  electrons can be trapped as lattice polarons.

Finally, we remark about the role of the on-site Coulomb interaction. Fig. 5.6 also compares the probability distribution of the lattice distortion with and without the Coulomb interaction. For  $U = 0$ , the two peaks are less separated which indicates the enhancement of the polaron formation by the Coulomb interaction. This is because the quasiparticles are strongly renormalized by the strong Coulomb interaction and thus much easier to be trapped by lattice distortion and spin disorder. Fig. 5.7 compares the spectral densities for  $g = 0.10$  with and without the Coulomb interac-

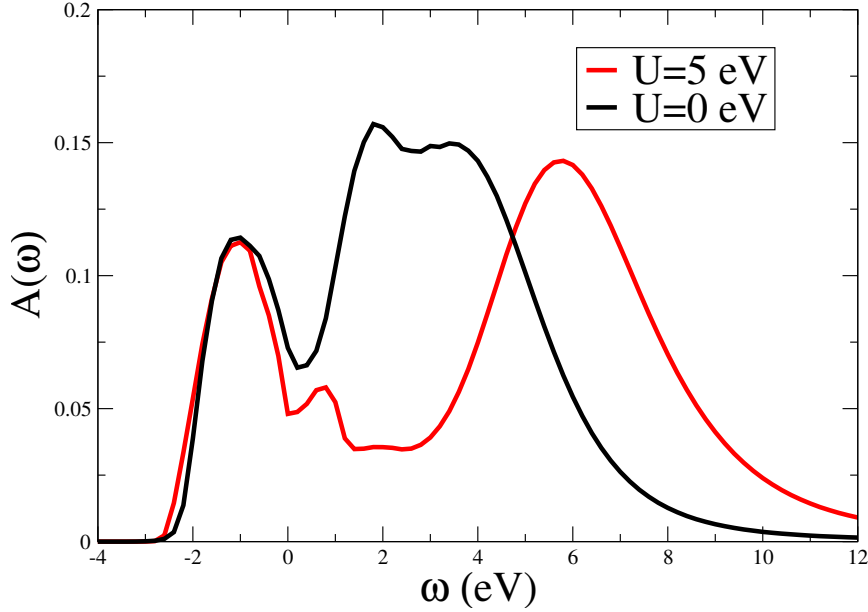


Figure 5.7: Paramagnetic spectral density at  $n = 0.8$ ,  $\beta = 16$  and  $g = 0.10$  for  $U = 0$  eV and  $U = 5$  eV.

tion. For  $U = 5$  eV, the polaron states below the Fermi energy are more localized. Some spectral weight is pushed away from the Fermi energy to higher energies and the pseudo-gap is strongly enhanced by the Coulomb interaction. Together with our LDA+DMFT results for  $\text{LaMnO}_3$ , this further confirms the important role of the Coulomb interaction in manganites.

### 5.2.2 Spectral density

The formation of lattice polarons provides for the basic physics of doped manganites. The electron spectral density can be seen as a combination of polaron states well below the Fermi energy and the midgap states above the Fermi energy. As shown in Fig. 5.6, this results in the strong suppression of the spectral weight at the Fermi energy and gives rise to a large energy gap for  $g = 0.15$  and a pseudo-gap for  $g = 0.10$ .

Fig. 5.8 plots the spectral density of the paramagnetic state for different couplings at  $\beta = 16$  and  $n = 0.8$ . Without Jahn-Teller coupling, the spectrum has a broad quasiparticle peak at the Fermi energy and the system is metallic. With increasing  $g$ , the quasiparticle peak is gradually suppressed and the spectral weight at the Fermi energy is reduced, leaving a dip in the spectrum for intermediate coupling and an energy gap for strong coupling. The low (high) energy Hubbard band also shifts toward lower (higher) energies. An additional peak shows up at  $\omega = 1 - 2$  eV,

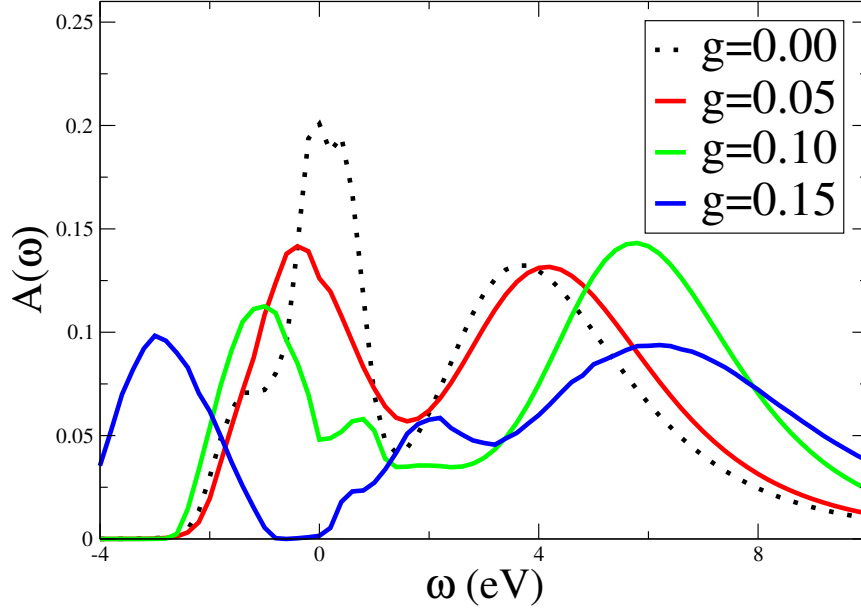


Figure 5.8: *Electron spectral density in the paramagnetic phase for different couplings  $g = 0, 0.05, 0.10,$  and  $0.15$ . The parameters are  $\beta = 16$  and  $n = 0.8$ . The quasiparticle peak is suppressed at large  $g$ , giving the pseudo-gap behavior for intermediate coupling and a large energy gap for strong coupling.*

ascribed to the midgap states with small dynamic lattice distortion.

The temperature dependence of the spectra is presented in Fig. 5.9 for both the paramagnetic and ferromagnetic phases. In the paramagnetic phase, the spectral weight at the Fermi energy is found to be more suppressed at lower temperature (see Fig. 5.9(a)). This is consistent with the temperature dependence of the distribution function of the lattice distortion shown in Fig. 5.4(a) in which the two peaks with small and large distortions are more separated at lower temperature.

Fig. 5.9(b) compares the spectral density of the paramagnetic and ferromagnetic phases at  $\beta = 30$ . Here the ferromagnetic results are obtained with (artificial) full spin polarization. We find that the pseudo-gap at the Fermi energy is filled in the ferromagnetic phase. This can be understood by the enhancement of the effective quasiparticle bandwidth with the spin ordering in the ferromagnetic phase. The low energy polaron peak in the spectrum is thus expected to be widened, giving rise to a larger spectral weight at the Fermi energy.

Now we turn to the doping dependence of the spectrum. Fig. 5.10 shows the spectral density for different dopings at  $\beta = 16$  and  $g = 0.10$ . Without doping, the system is a good insulator. The spectrum shows a large energy gap (about 2.3 eV) which is beyond the experimental value of 1 eV and hence suggests a slightly larger

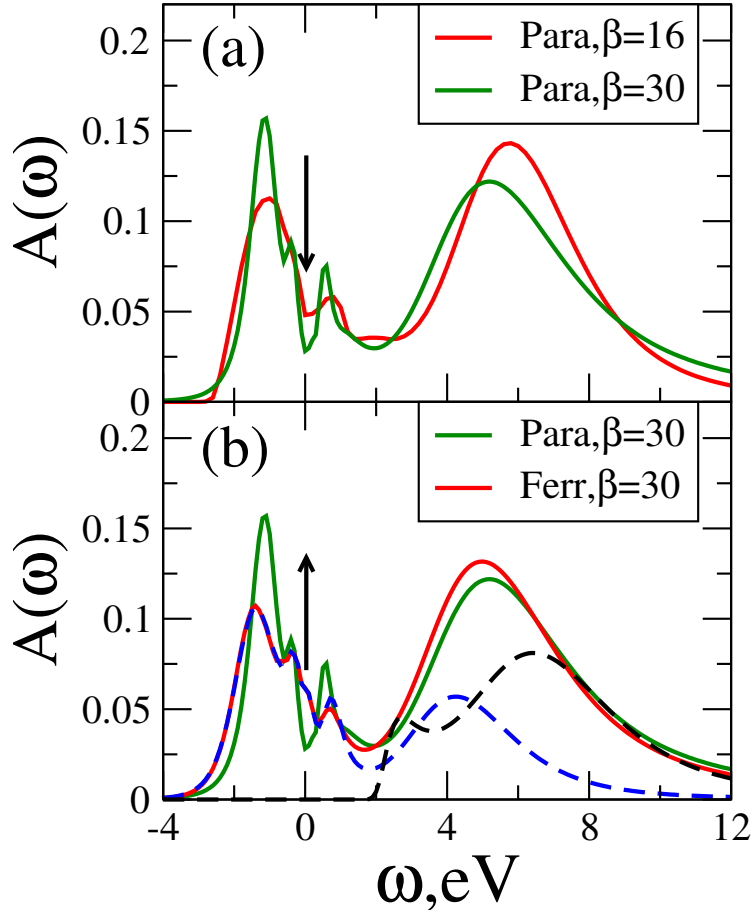


Figure 5.9: Spin-averaged spectral density at: (a)  $\beta = 16$  and 30 in the paramagnetic phase; (b)  $\beta = 30$  in both the paramagnetic and ferromagnetic phases. The parameters are  $g = 0.10$  and  $n = 0.8$ . The different spin components in the ferromagnetic spectral density are also plotted (the dashed lines). The antiparallel spin states only contribute to the high energy broad peak due to the large Hund's coupling.

Coulomb interaction and/or Jahn-Teller coupling used in the calculations. A small doping  $x = 0.1$  introduces some midgap states just above the Fermi energy and changes the large energy gap into a pseudo-gap at the Fermi energy. If the doping is large enough, the midgap states can dominate at the Fermi energy so that the pseudo-gap is completely filled (at  $n = 0.3$ ). However, due to the strong lattice, orbital and spin scatterings, the quasiparticle peak is still suppressed.

### 5.2.3 Optical conductivity

In this section, we calculate the optical conductivity from the DMFT results following the method discussed in section 3.4 and compare it with experiments. We

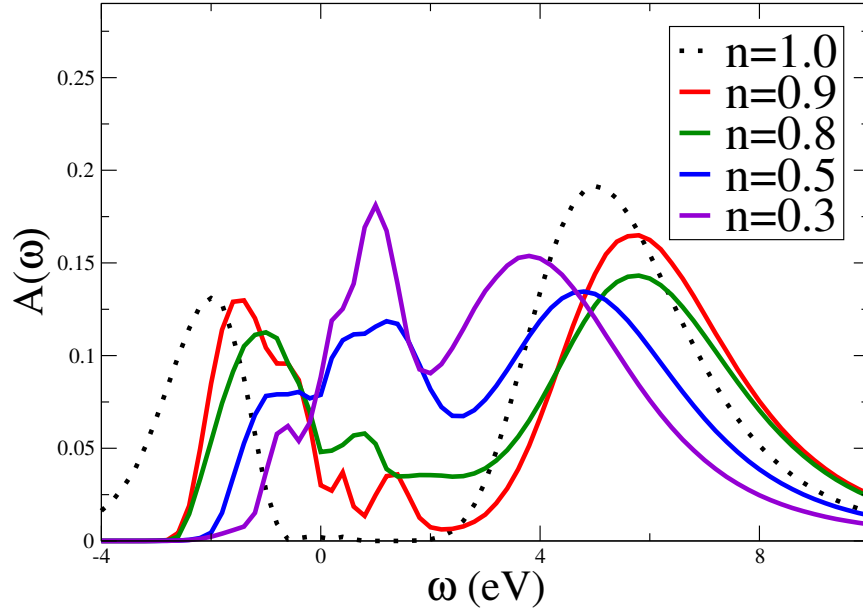


Figure 5.10: Paramagnetic spectral density for different electron occupations  $n = 1.0, 0.9, 0.8, 0.5,$  and  $0.3$  at  $\beta = 16$  and  $g = 0.10$ .

find that all the optical properties such as the pseudo-gap behavior in the paramagnetic phase and the "bad" metallic behavior in the ferromagnetic phase can be obtained theoretically by DMFT. The metal-insulator transition and the colossal magnetoresistance are also explained as a result of the magnetic transition.

Fig. 5.11 shows the optical conductivity in the paramagnetic phase for different occupancies  $n = 0.8, 0.5,$  and  $0.3$ . We take  $\beta = 30$  and  $g = 0.10$ . The spectra have two peaks at 1-2 eV and 6 eV and with increasing doping, the low energy optical peak shifts to lower energies, in agreement with the experimental observations (see Fig. 5.2, for example) [Okimoto et al. 1995, Jung et al. 1998, Takenaka et al. 1999, Tobe et al. 2004].

This agreement allows us to identify the origin of the two optical peaks. Note that in Fig. 5.9, the electron spectral densities contain three peaks, consisting of the polaron states below the Fermi energy, the undistorted unoccupied states or the midgap states just above the Fermi energy, and the distorted unoccupied states far above the Fermi energy. The charge transitions between these states give rise to the optical peaks in the numerical calculations (Fig. 5.11). So the low energy optical peak at 1-2 eV is from the excitation of the localized polarons to the (undistorted unoccupied) midgap states (interatomic  $\text{Mn}^{3+}\text{Mn}^{4+} \rightarrow \text{Mn}^{4+}\text{Mn}^{3+}$ ), while the high energy optical peak at 6 eV stems from the interatomic  $\text{Mn}^{3+}\text{Mn}^{3+} \rightarrow \text{Mn}^{4+}\text{Mn}^{2+}$  transition, namely, the excitation of the polaron states to the high energy states



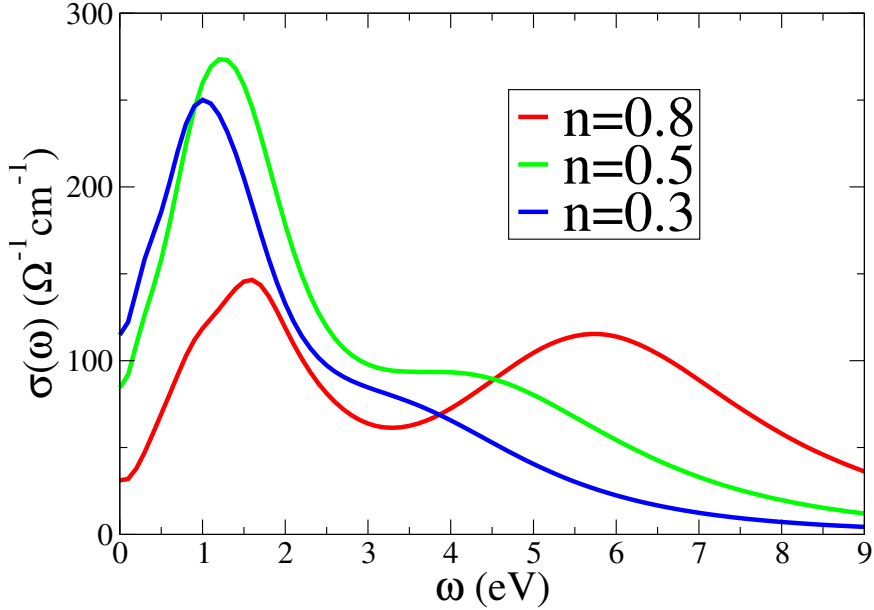


Figure 5.11: *Optical conductivity in paramagnetic phase for different electron occupations  $n = 0.8, 0.5, 0.3$  at  $\beta = 30$  and  $g = 0.10$ .*

on a neighboring occupied site. Since in our theory the midgap states do not exist in the undoped case and are unique for doped manganites, they do not contribute to the optical spectrum of  $\text{LaMnO}_3$ . For different parameters such as a smaller Coulomb interaction  $U$ , part of the interatomic  $\text{Mn}^{3+}\text{Mn}^{3+} \rightarrow \text{Mn}^{4+}\text{Mn}^{2+}$  process may also contribute to the low energy optical peak. Thus the low energy optical peak at 1-2 eV may have two different contributions: the polaron excitation to the (undistorted unoccupied) midgap states (only in doped manganites) and part of the interatomic  $\text{Mn}^{3+}\text{Mn}^{3+} \rightarrow \text{Mn}^{4+}\text{Mn}^{2+}$  transition. Fig. 5.12 sketches these different optical processes.

Historically, the midgap states (the 1-eV feature) in the optical spectra was first observed by [Okimoto et al. 1997] and ascribed to the transition between the  $e_g$  spin states parallel and antiparallel to the local  $t_{2g}$  spin. This interpretation was later proved to be wrong [Quijada et al. 1998, Jung et al. 1998]. Experimentally, an intraatomic  $\text{Mn}^{3+} \rightarrow \text{Mn}^{3+}$  process has also been argued to be present in both doped and undoped manganites due to the O  $2p$  and Mn  $3d$  hybridization [Jung et al. 1998]. But more work is necessary and the exact origin of the first optical peak is not yet established experimentally.

Let me also note that, in experiment, the high energy optical peak has a larger magnitude than the low energy peak, which is different from our numerical results. This may be ascribed to other contributions from the oxygen charge transfer, La

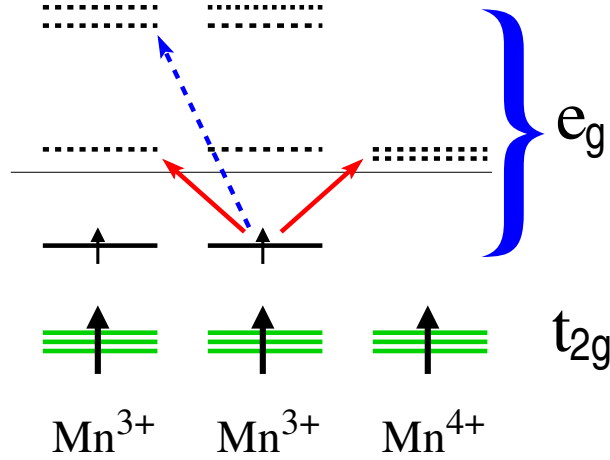


Figure 5.12: Schematic representation of the optical processes in doped manganites. Arrows indicate the processes. The right red arrow represents the polaron excitation to the midgap states. The left arrows represent the interatomic  $Mn^{3+}Mn^{3+} \rightarrow Mn^{4+}Mn^{2+}$  transition. We use the red color for the possible contributions to the low energy optical peak and the blue color for the process contributed to the high energy optical peak.

bands, and the upper Hubbard band of the  $t_{2g}$  electrons, etc. Such effects are beyond our low-energy Hamiltonian. In fact, in Ref. [Jung et al. 1998], the effective kinetic energy of the  $e_g$  electrons calculated from the experimental optical conductivity below 3 eV is already beyond the noninteracting kinetic energy, indicating the existence of additional contributions other than the Mn  $e_g$  bands.

Fig. 5.13 shows the temperature dependence of the optical conductivity in the paramagnetic phase. The low energy optical conductivity is suppressed as a result of the pseudo-gap in the spectral density. With decreasing temperature, the optical spectrum is more suppressed since there is less thermal excitation. The resistivity is thus enhanced at low temperature, giving rise to the insulating behavior in the paramagnetic phase.

Fig. 5.14 compares the optical conductivity in the paramagnetic and ferromagnetic phase at  $n = 0.8$  and  $\beta = 30$ . Due to the spin ordering in the ferromagnetic phase, the pseudo-gap in the low energy optical conductivity is filled. However, instead of a sharp Drude peak, the optical spectrum is almost constant below 1 eV in agreement with experiment (see Fig. 5.3). This indicates the strong damping of quasiparticles due to the orbital disorder and the lattice distortion in doped manganites, even in the ferromagnetic phase. In fact, we find a large imaginary part of the self-energy  $|\text{Im}\Sigma(0)| \sim 1.9$  eV. The system is a "bad" metal below  $T_c$ .

At  $\omega = 0$ , Fig. 5.14 shows that the resistivity in the paramagnetic phase is about

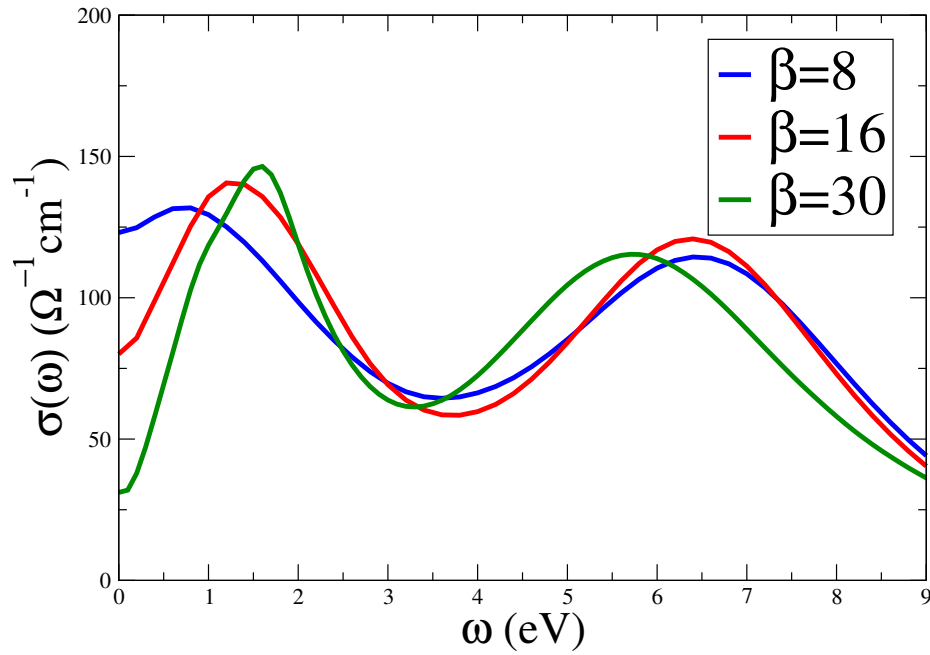


Figure 5.13: Optical conductivity in the paramagnetic phase at average occupancy  $n = 0.8$  and inverse temperature  $\beta = 8, 16,$  and  $30$ .

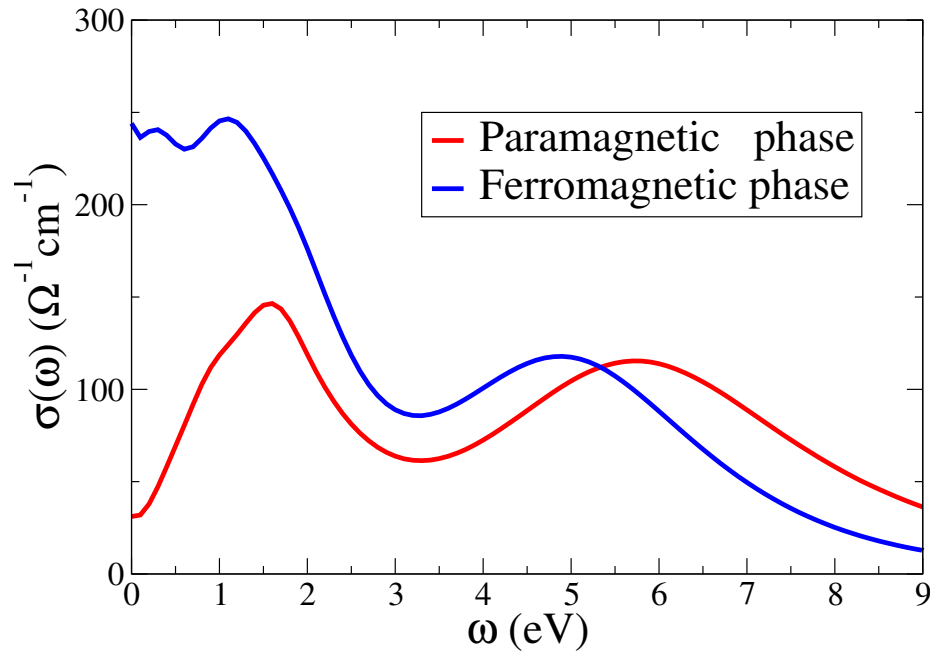


Figure 5.14: Optical conductivity in both the paramagnetic and ferromagnetic phases at  $n = 0.8$  and  $\beta = 30$ . The low energy part of the optical spectrum is strongly enhanced in the ferromagnetic phase.

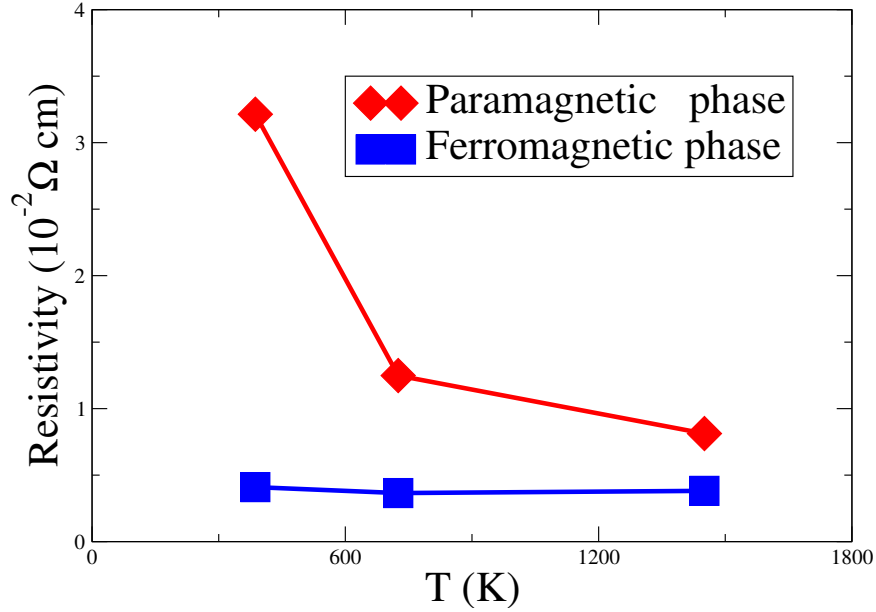


Figure 5.15: Resistivity as a function of temperature in both the paramagnetic and ferromagnetic phases at  $n = 0.8$ . The different temperature dependence of the resistivity between two phases leads to the "colossal" magnetoresistance under magnetic field and the metal-insulator transition at  $T_c$ .

8 times larger than that in the ferromagnetic phase at  $\beta = 30$ . This indicates an abrupt drop of the resistivity at the Curie temperature. Since in our DMFT calculations the ferromagnetic phase is treated by assuming (artificial) full spin polarization, a strong magnetic field should lead to the same results. We thus expect a large magnetoresistance, although the detailed behavior of the resistivity below  $T_c$  or under an external magnetic field is more complicated due to the incomplete magnetization. The results also demonstrate that the magnetoresistance is strongly enhanced by the different behavior of the resistivity, namely, the metallic and insulating behavior, below and above  $T_c$ .

Fig. 5.15 plots the resistivity at high temperature in both the paramagnetic phase and the hypothetic ferromagnetic phase. This allows us to observe the tendency of the resistivity at low temperature ( $T < 400$  K). We see good agreement with the experimental results shown in Fig. 5.1(a).

To summarize, a strong Jahn-Teller coupling suppresses the spectral weight at the Fermi energy. The electron spectral density is found to be a combination of the polaron states, the (undistorted unoccupied) midgap states, and the distorted unoccupied states. This gives rise to the pseudo-gap behavior in the high temperature paramagnetic phase. The excitation from the polaron states to the midgap states

explains the low energy optical peak observed in doped manganites. The high energy optical peak comes from the interatomic  $\text{Mn}^{3+}\text{Mn}^{3+} \rightarrow \text{Mn}^{4+}\text{Mn}^{2+}$  transition, as well as other possible contributions beyond the two-band model. In the ferromagnetic phase, the  $e_g$  electrons are less scattered due to the spin ordering. So the system is more metallic below  $T_c$  and the metal-insulator transition occurs as a result of the magnetic transition. Despite of this, the orbital disorder and the lattice distortion induce strong damping of quasiparticles even far below the Curie temperature and the system shows "bad" metallic behavior over a wide doping range. The abrupt change of the magnetization at the Curie temperature leads to the abrupt change of the spin scattering and thus the resistivity. Under an external magnetic field, the Curie temperature increases and the system changes from an insulator to a metal, resulting in the "colossal" magnetoresistance in doped manganites.

#### 5.2.4 Curie temperature

To complete our DMFT investigations for doped manganites, we also present a short discussion on the theoretical Curie temperature following the method introduced in section 3.3. We first calculate the static spin susceptibility  $\chi(T)$  in the high temperature paramagnetic phase and then fit  $\chi(T)^{-1}$  linearly to obtain the Curie temperature  $T_c$ .

As an example, Fig. 5.16 shows the doping dependence of the Curie temperature for the Jahn-Teller coupling  $g = 0.10 \text{ eV}^{3/2}$ . Compared to the experimental results in Fig. 1.2, the theoretical predictions of  $T_c$  have a similar shape with a maximum at intermediate doping but are about 2-3 times larger in magnitude. As discussed previously in section 3.3, the Curie temperature is suppressed close to  $n = 1$  ( $x = 0$ ) due to the high energy cost of double occupancy to overcome the strong Coulomb repulsion, the Jahn-Teller splitting, and the Hund's rule coupling. For large doping, the total kinetic energy is reduced, and according to the double exchange mechanism, the indirect ferromagnetic coupling between Mn  $t_{2g}$  spins induced by the hopping of the  $e_g$  electrons is also reduced, resulting in a relative low Curie temperature. The effect of the Coulomb interaction is most important near  $n = 1$  and becomes less effective at large doping.

The magnitude of the Curie temperature depends strongly on the strength of the Jahn-Teller coupling and the hopping integral of the  $e_g$  electrons. Fig. 5.17 plots its coupling dependence at  $n = 0.8$ , which are similar to the previous results in [Millis et al. 1996c, Edwards 2002] (also see Fig. 2.5). The Curie temperature decreases rapidly with increasing coupling. For strong Jahn-Teller coupling, a slight increase of  $g$  from 0.10 to 0.12 (or the dimensionless coupling  $\lambda$  from 2.0 to 2.2)

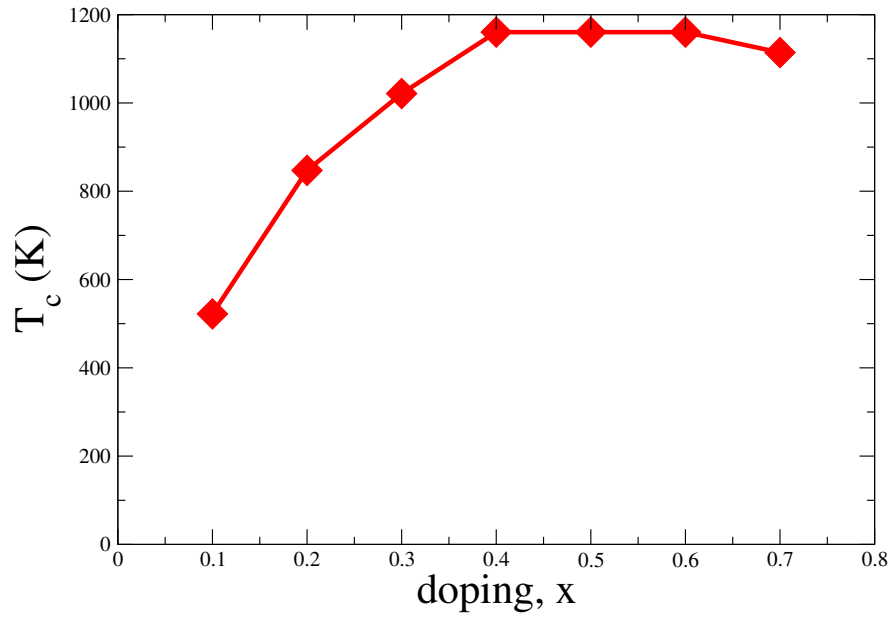


Figure 5.16: Curie temperature as a function of doping  $x = 1 - n$  for  $g = 0.10$ .

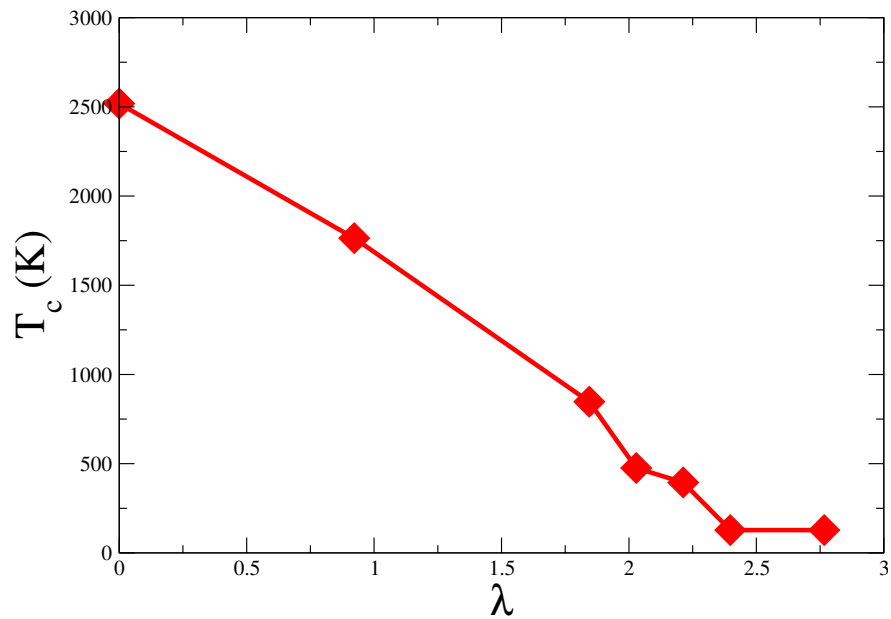


Figure 5.17: Curie temperature as a function of the dimensionless coupling  $\lambda = g/\Omega\sqrt{t_0}$  at  $n = 0.8$ . The parameters are  $t_0 = 0.6$  eV and  $\Omega = 0.07$  eV.

reduces  $T_c$  by a factor of 2 so that  $g = 0.12$  (or  $\lambda = 2.2$ ) gives the correct experimental value.

The Curie temperature may also be affected by many factors which are not in the low-energy Hamiltonian. These include the quantum fluctuation of Mn  $t_{2g}$  spins

and the antiferromagnetic superexchange coupling between Mn  $t_{2g}$  spins. Both tend to weaken the ferromagnetic order and suppress the Curie temperature. The antiferromagnetic superexchange coupling has been estimated to be the order of 200 K [Perring et al. 1997, Dagotto et al. 2001] which, if taken into account, would greatly reduce the theoretical value of the Curie temperature.

Historically, the Curie temperature has been calculated with different methods such as DMFT [Millis et al. 1995, Millis et al. 1996a, Held & Vollhardt 2000], the mean-field theory [Röder et al. 1996], QMC simulations [Yunoki et al. 1998], and the many-body CPA [Edwards 2002]. Some of the results seem to be in better agreement with experiments. However, we should note that these results are all based on the details of the models and approaches and are very sensitive to the values of the parameters which, unfortunately, are not always reliable and, as a matter of fact, vary considerably in the literature. A complete analysis of the problem is still required.

### 5.3 Estimates of parameters

In the last section, we have discussed the DMFT (QMC) calculations for doped manganites. The pseudo-gap behavior in the paramagnetic phase and the bad metallic behavior in the ferromagnetic phase have been understood theoretically, and the optical spectra have been interpreted as the excitation of lattice polarons. Also in the last chapter, we have clarified the nature of the pressure-induced insulator-to-metal transition based on LDA+DMFT calculations. These results support the important roles of both the Coulomb interaction and the Jahn-Teller coupling in manganites. Therefore, if it is true that the low energy optical peak of  $\text{LaMnO}_3$  stems from the interatomic  $\text{Mn}^{3+}\text{Mn}^{3+} \rightarrow \text{Mn}^{4+}\text{Mn}^{2+}$  transition as is that of doped manganites, our realistic microscopic Hamiltonian (2.20) allows for a unified description of both doped and undoped manganites.

Qualitatively, the effects of both interactions are already very clear. The Jahn-Teller coupling leads to the formation of lattice polarons and plays a crucial role in determining the physics of doped manganites, whereas the Coulomb interaction strongly renormalizes the quasiparticle bandwidth and thus enhances the formation of lattice polarons. In  $\text{LaMnO}_3$ , the orbital splitting induced by the Jahn-Teller distortion is enhanced by the Coulomb repulsion, giving rise to the insulating ground state. In both doped and undoped systems, the low energy spectral weight in the optical conductivity is transferred to higher energies because of the existence of the two interactions and the Hund's rule coupling.

However, we still need to find a set of consistent parameters for both systems. To

obtain the 1 eV energy gap in LaMnO<sub>3</sub>, we have taken  $U = 5$  eV and  $g = 0.05$  eV<sup>3/2</sup>, but a larger Jahn-Teller coupling  $g = 0.10$  eV<sup>3/2</sup> is required to explain the pseudo-gap behavior in doped manganites. Therefore, a quantitative and systematic study is still necessary in order to find a unique set of  $U$  and  $g$ .

To this end, we include the breathing mode  $Q_{1i}$  and study the model Hamiltonian

$$\begin{aligned}
 H = & - \sum_{\langle\langle ij \rangle\rangle; \mu\nu\sigma} t_{\mu\nu}^{ij} c_{i\mu\sigma}^\dagger c_{j\nu\sigma} - 2J \sum_{i;\mu} \mathbf{s}_{i\mu} \cdot \mathbf{S}_i \\
 & + U \sum_{i;\mu} n_{i\mu\uparrow} n_{i\mu\downarrow} + \sum_{i;\sigma\bar{\sigma}} (V - \delta_{\sigma\bar{\sigma}} F) n_{i1\sigma} n_{i2\bar{\sigma}} \\
 & - g \sum_{i;\mu\nu\sigma} c_{i\mu\sigma}^\dagger (Q_{1i} \mathcal{I} + Q_{2i} \tau^x + Q_{3i} \tau^z)_{\mu\nu} c_{i\nu\sigma} + \sum_{i;a} \left( \frac{P_{ai}^2}{2} + \frac{\Omega^2}{2} Q_{ai}^2 \right). \quad (5.3)
 \end{aligned}$$

The effect of the breathing mode will be first discussed. Then we provide a new estimate of the parameters by comparing the theoretical and experimental results of the energy gap in LaMnO<sub>3</sub> and the resistivity in La<sub>1-x</sub>Sr<sub>x</sub>MnO<sub>3</sub>.

**The breathing mode** As before, we use DMFT (QMC) to study the physical effect of the breathing mode. As an example, Fig. 5.18 shows the probability distribution of both the breathing and Jahn-Teller phonon fields at  $\beta = 16$  and  $n = 0.8$ . The

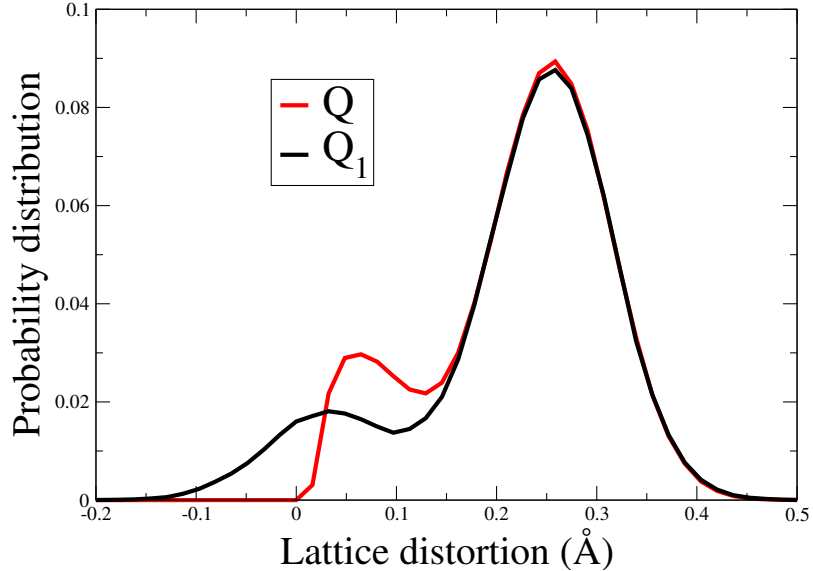


Figure 5.18: Probability distribution of the breathing ( $Q_1$ ) and Jahn-Teller ( $Q$ ) modes for the model Hamiltonian (5.3) at  $n = 0.8$  and  $\beta = 16$ . The parameters are  $U = 5$  eV,  $V = 3.5$  eV,  $F = 0.75$  eV, and  $g = 0.08$  eV<sup>3/2</sup>. The phonon frequencies are  $\Omega = 0.07$  eV for all three modes.



phonon frequency is  $\Omega = 0.07 \text{ eV}$  for all three modes. We take  $g = 0.08 \text{ eV}^{3/2}$ ,  $U = 5 \text{ eV}$ ,  $F = 0.75 \text{ eV}$  and  $V = 3.5 \text{ eV}$ . Except for the Jahn-Teller distortion  $Q$  being positive by definition, the distribution function of the breathing phonon is similar to that of the Jahn-Teller distortion and has also two peaks located at about  $g/\Omega^2$  and 0. These two peaks are related to the polaron states and the midgap states discussed before. The only difference is the way in which the phonon modes are coupled to the  $e_g$  electrons: The breathing mode is coupled to the electron density, while the Jahn-Teller modes are coupled to the orbital polarization (with respect to a certain basis). Due to the Hund's coupling and the strong Coulomb interaction, the double occupancy is forbidden. So the difference is not reflected in the distribution function.

Since the breathing mode only couples to the electron density, it lowers the localization energy of the polaron states but leaves the midgap states unchanged. The  $e_g$  electrons are thus more localized due to the inclusion of the breathing mode and the system becomes more insulating.

Fig. 5.19 compares the spectral densities at  $\beta = 16$  and  $n = 0.8$  with and without the breathing phonon. As expected, we see the density of states at the Fermi energy is strongly suppressed by the existence of the breathing mode.

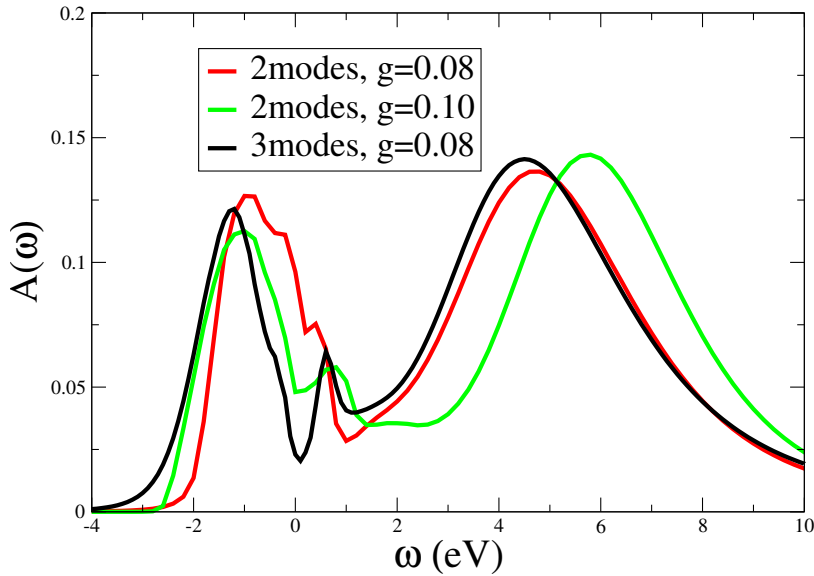


Figure 5.19: *Electron spectral density for  $U = 5 \text{ eV}$ ,  $V = 3.5 \text{ eV}$ ,  $F = 0.75 \text{ eV}$ ,  $n = 0.8$  and  $\beta = 16$ . The coupling constant is taken as  $g = 0.08$  for calculations with all three phonon modes and  $g = 0.08, 0.10$  for calculations with only the Jahn-Teller modes. The phonon frequencies are  $\Omega = 0.07 \text{ eV}$  for all three modes.*

**Parameters** To complete the thesis, we make a new estimate of the most relevant parameters, the on-site Coulomb interaction  $U$  and the Jahn-Teller coupling  $g$ , based on the DMFT model calculations of the realistic microscopic model (5.3) and the optical data of manganites. We take into account the breathing mode and, for simplicity, fix all other parameters as following: the bandwidth  $W = 3.6$  eV for the cubic structure, the exchange interaction  $F = 0.75$  eV, the Hund's rule coupling  $2J|\mathbf{S}| = 2.7$  eV, and the phonon frequency  $\Omega = 0.07$  eV for all three phonon modes. Due to the cubic symmetry, we have  $V = U - 2F$ .

The two parameters  $U$  and  $g$  will be determined by fitting the optical data of the energy gap (about 1 eV) in  $\text{LaMnO}_3$  [Okimoto et al. 1995, Quijada et al. 1998, Jung et al. 1998, Takenaka et al. 1999] and the resistivity (roughly  $0.035 \Omega\text{cm}$  at  $\beta = 30$ ) in  $\text{La}_{0.825}\text{Sr}_{0.175}\text{MnO}_3$  [Tokura et al. 1994, Urushibara et al.1995].

The inset (a) of Fig. 5.20 plots the energy gap for different Coulomb interactions  $U$  and Jahn-Teller couplings  $g$  calculated by DMFT (QMC) for the model Hamiltonian

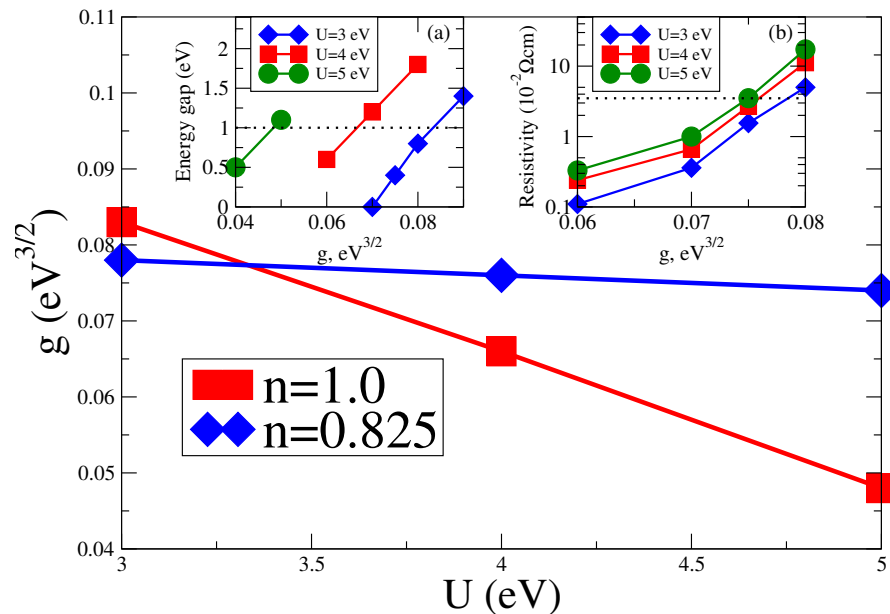


Figure 5.20: Two sets of parameters which fit the experimental energy gap in  $\text{LaMnO}_3$  and the resistivity in  $\text{La}_{0.825}\text{Sr}_{0.175}\text{MnO}_3$ . Their intersection gives a single set of  $U$  and  $g$  which is expected to describe quantitatively both doped and undoped manganites. The insets show the DMFT (QMC) results as a function of the Coulomb interaction  $U$  and the Jahn-Teller coupling  $g$  for: (a) the energy gap at  $n = 1$  and (b) the resistivity at  $n = 0.825$ . Both are calculated at  $\beta = 30$ . The experimental results are indicated by the dotted line with the 1 eV energy gap in  $\text{LaMnO}_3$  and the resistivity of about  $0.035 \Omega\text{cm}$  for  $\text{La}_{0.825}\text{Sr}_{0.175}\text{MnO}_3$  [Tokura et al. 1994, Urushibara et al.1995].

(5.3). As expected, the energy gap depends strongly on both parameters.

The inset (b) of Fig. 5.20 shows the DMFT (QMC) results of the resistivity for different  $U$  and  $g$  at  $n = 0.825$  ( $x = 0.175$ ) and  $\beta = 30 \text{ eV}^{-1}$ . As has been analyzed before, the Coulomb interaction also affects the resistivity of the system since it enhances the electron localization. This is now proved explicitly in the figure. The resistivity increases with increasing  $U$ . Also, it depends more sensitive on  $g$  than  $U$  due to the polaron physics in which the Coulomb interaction has only an indirect influence. As we can see, the effect of the Coulomb interaction is most important near  $n = 1$  and becomes less effective at large dopings.

By comparing with the experimental data, the above two figures provide for two different sets of  $U$  and  $g$  which we plot in the main panel in Fig. 5.20. The intersection of the two sets of parameters gives  $U = 3.3 \text{ eV}$  and  $g = 0.077 \text{ eV}^{3/2}$ . These results agree with the previous experimental estimates (Table 2.1 in section 2.4) and are thus expected to be a proper choice for the model Hamiltonian (5.3) to describe quantitatively the optical experiments of both doped and undoped manganites. Table 5.1 presents the estimated values of all the parameters.

As a final example, Fig. 5.21 shows the optical conductivity for different dopings using the new parameters. The inset is the effective carrier concentration  $N_{eff}(\omega)$  calculated from the integral of the optical conductivity using Eq. (3.107). For direct comparison, the figure is plotted analogous to the experiment in Fig. 5.2. We see a continuous crossover from the undoped to the doped system and a good agreement in the general behavior of the optical conductivity. However, as discussed before, the experimental magnitude of the optical peaks are 2-3 times larger than the theoretic-

W	U	2J S	F	$\Omega$	g
3.6 eV	3.3 eV	2.7 eV	0.75 eV	0.07 eV	$0.077 \text{ eV}^{3/2}$

Table 5.1: Parameters estimated for manganites. W: bandwidth; U: intra-orbital Coulomb interaction; F:  $e_g$ - $e_g$  exchange interaction; J:  $e_g$ - $t_{2g}$  Hund's coupling;  $\Omega$ : phonon frequency;  $g$ : Jahn-Teller coupling. The bandwidth is obtained from the LDA calculations for the cubic structure [Yamasaki et al. 2006], the Hund's coupling is calculated by the constrained LDA for the ferromagnetic phase, and the phonon frequency is estimated from the Raman spectroscopy [Iliev et al. 1998]. Only the Coulomb interaction  $U$  and the Jahn-Teller coupling  $g$  are estimated from the DMFT (QMC) calculations for the model Hamiltonian (5.3) by fitting the experimental data of the energy gap in  $\text{LaMnO}_3$  and the resistivity in  $\text{La}_{0.825}\text{Sr}_{0.175}\text{MnO}_3$ .

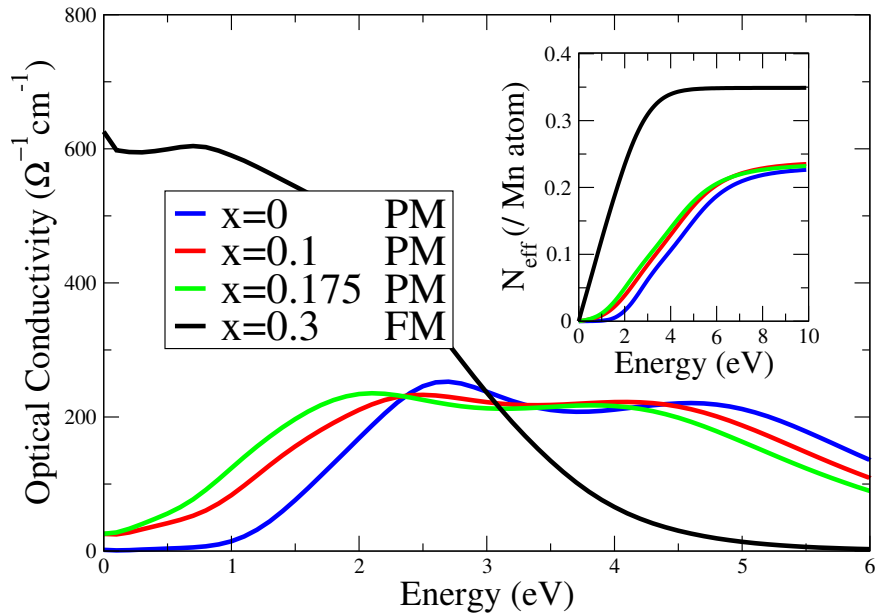


Figure 5.21: Optical conductivity at  $x = 0, 0.1, 0.175$  in the paramagnetic phase and  $x = 0.3$  in the ferromagnetic phase. The parameters are taken as is in Table 5.1 and the inverse temperature is  $\beta = 30$  eV. The inset shows the effective carrier concentration calculated according to Eq. (3.107).

cal one [Quijada et al. 1998]. This gives rise to an unexpected large experimental  $N_{eff}(\omega)$  even below 4 eV and keeps increasing at higher energies, in contrast to the theoretical predictions presented in the inset of Fig. 5.21.

The discrepancies indicate other mechanisms besides the two-band model of the Mn  $e_g$  electrons. We suggest additional contributions to the low energy optical peak from the O  $2p$  and Mn  $3d$  hybridization. In Ref. [Jung et al. 1998], an intraatomic  $Mn^{3+} \rightarrow Mn^{3+}$  process has been argued to be present in both doped and undoped manganites due to the hybridization. The high energy optical peak may also be enhanced by contributions such as La bands and the upper Hubbard band of the  $t_{2g}$  electrons, which are beyond the effective low-energy Hamiltonian. All these new mechanisms require further investigations.

## 6 Conclusions and outlook

In this thesis, we have used DMFT to study the physics of manganites. By combining DMFT with LDA band structure calculations, we have investigated the pressure-induced insulator-to-metal transition in  $\text{LaMnO}_3$ . The  $e_g$  orbital splitting induced by the Jahn-Teller distortion was found to be strongly enhanced by the strong on-site Coulomb interaction, giving rise to the insulating ground state of  $\text{LaMnO}_3$  at ambient conditions. Under external pressure, the orbital splitting is suppressed and an insulator-to-metal transition occurs. However, there exists no intermediate insulating phase without the lattice distortion, in contrast to previous claims [Loa et al. 2001, Banach & Temmerman 2004, Zenia et al. 2005]. Instead, a reduced but still finite Jahn-Teller distortion is present at the transition point and the insulator-to-metal transition is thus not of Mott-Hubbard type. On the other hand, the band structure calculations also show that the Jahn-Teller distortion alone is not strong enough to make  $\text{LaMnO}_3$  an insulator at 0 GPa. Hence our results demonstrate that both the Coulomb interaction and the electron-phonon interaction play important roles for the electronic behavior in manganites.

A realistic microscopic model was then proposed for taking into account both the electron-electron and electron-phonon interactions, together with the Hund's rule coupling between the  $e_g$  conduction electrons and the  $t_{2g}$  spins [Yang & Held 2006]. DMFT calculations were performed for both undoped and doped systems. In the undoped system, the model produces similar results as the LDA+DMFT calculations and, most surprisingly, it also predicts the correct structural transition temperature from dynamic to static Jahn-Teller distortion [Chatterji et al. 2003]. In doped manganites, the model leads to the lattice polaron picture [Millis et al. 1996a]. The  $\text{MnO}_6$  octahedra are found to be partially distorted. The  $e_g$  electrons are trapped by the large lattice distortion and form lattice polarons. This localization of the polarons is found to be supported by the Coulomb interaction. The undistorted unoccupied states explain the so-called midgap states observed in experiments [Jung et al. 1998]. The spectral density at the Fermi energy is then found to be determined by the combination of the polaron states and the midgap states, which, for intermediate electron-phonon coupling, gives rise to the pseudo-gap behavior observed in doped manganites. Our results provide for an explanation of the insulating-like behavior above  $T_c$  and the bad metallic behavior below  $T_c$  over

a wide range of doping. The metal-insulator transition at  $T_c$  is a result of the magnetic transition which changes the spin scattering of the  $e_g$  conduction electrons. An external magnetic field shifts the Curie temperature and can hence turn an insulator into a metal, resulting in the so-called colossal magnetoresistance.

These results show that the realistic microscopic model (2.20) can be applied to both doped and undoped manganites and can therefore be taken as the starting point towards a complete understanding of the physics of the materials. The quantitative effect of the Coulomb interaction and the electron-phonon coupling was then investigated numerically and a new estimate of the parameters was provided by comparing the results to the optical data [Tokura et al. 1994, Urushibara et al. 1995, Okimoto et al. 1995, Quijada et al. 1998, Jung et al. 1998, Takenaka et al. 1999]. The values of these parameters lie within the experimental estimates [Park et al. 1996, Kovaleva et al. 2004]. The general behavior of the theoretical optical spectra is found to be in good agreement with experiments.

Despite these successes, the work also reveals some problems which require further investigations. These include:

- A better treatment of the ferromagnetic phase which allows for calculations of the magnetization around  $T_c$ . The problem has been studied by other groups using simplified models, but is impossible for the full Hamiltonian of this work due to the limitation of the finite temperature QMC to relatively high temperatures. A different impurity solver is necessary.
- The magnitude of the optical peaks observed in both doped and undoped manganites. The optical experiments give an unexpected larger sum rule than the theoretical one (see section 5.3). This suggests other contributions, e.g., from the O  $2p$  orbitals, La bands, and the upper Hubbard band of the  $t_{2g}$  electrons, which are beyond our low-energy effective Hamiltonian and can only be treated in a more complicated model.
- The realistic lattice distortion. For this, we have to include other contributions such as the cooperative Jahn-Teller effect and the anharmonic phonon potential (see section 4.3.1). The problem is beyond our single-impurity DMFT (QMC) method and can only be treated in a more sophisticated method such as the cluster extensions of DMFT [Kotliar et al. 2001, Potthoff et al. 2003, Kotliar et al. 2006].

Huge numerical efforts are the main obstacles for further investigations of the above problems. However, comparisons between experimental data and numerical calculations will be the only way towards a complete theory of manganites.

## Bibliography

In the online PDF file, simply click on the journal references and arXiv numbers!  
After each citation appear the page numbers where it is referenced.

- [Aliaga et al. 2003] H. Aliaga, D. Magnoux, A. Moreo, D. Poilblanc, S. Yunoki, and E. Dagotto, *Theoretical study of half-doped models for manganites: Fragility of CE phase with disorder, two types of colossal magnetoresistance, and charge-ordered states for electron-doped materials*, Phys. Rev. B **68**, 104405 (2003). 23
- [Andersen & Saha-Dasgupta 2000] O. K. Andersen and T. Saha-Dasgupta, *Muffin-tin orbitals of arbitrary order*, Phys. Rev. B **62**, R16219 (2000). 57, 64
- [Anderson & Hasegawa 1955] P. W. Anderson and H. Hasegawa, *Considerations on double exchange*, Phys. Rev. **100**, 675 (1955). 16
- [Anisimov & Gunnarsson 1991] V. I. Anisimov and O. Gunnarsson, *Density-functional calculation of effective Coulomb interactions in metals*, Phys. Rev. B **43**, 7570 (1991). 31
- [Anisimov et al. 1997] V. I. Anisimov, A. I. Poteryaev, M. A. Korotin, A. O. Anokhin, and G. Kotliar, *First-principles calculations of the electronic structure and spectra of strongly correlated systems: dynamical mean-field theory*, J. Phys.: Condens. Matter **9**, 7359 (1997). 12, 57
- [Anisimov et al. 2005] V. I. Anisimov, D. E. Kondakov, A. V. Kozhevnikov, I. A. Nekrasov, Z. V. Pchelkina, J. W. Allen, S.-K. Mo, H.-D. Kim, P. Metcalf, S. Suga, A. Sekiyama, G. Keller, I. Leonov, X. Ren, and D. Vollhardt, *Full orbital calculation scheme for materials with strongly correlated electrons*, Phys. Rev. B **71**, 125119 (2005). 57
- [Bala & Oleś 2000] J. Bala and A. M. Oleś, *Jahn-Teller effect on orbital ordering and dynamics in ferromagnetic LaMnO<sub>3</sub>*, Phys. Rev. B **62**, R6085 (2000). 74
- [Banach & Temmerman 2004] G. Banach and W. M. Temmerman, *Pressure induced charge disproportionation in LaMnO<sub>3</sub>*, J. Phys.: Condens. Matter **16**, S5633 (2004). 12, 59, 70, 107

- [Bao et al. 1993] W. Bao, C. Broholm, S. A. Carter, T. F. Rosenbaum, G. Aeppli, S. F. Trevino, P. Metcalf, J. M. Honig, and J. Spalek, *Incommensurate spin density wave in metallic  $V_{2-y}O_3$* , Phys. Rev. Lett. **71**, 766 (1993). 25
- [Blankenbecler et al. 1981] R. Blankenbecler, D. J. Scalapino, and R. L. Sugar, *Monte Carlo calculations of coupled boson-fermion systems. I*, Phys. Rev. D **24**, 2278 (1981). 27, 36, 37, 38
- [Blümer 2003] N. Blümer, *Mott-Hubbard metal-insulator transition and optical conductivity in high dimensions*, Shaker Verlag, Aachen, 2003. 50, 53
- [Bocquet et al. 1992] A. E. Bocquet, T. Mizokawa, T. Saitoh, H. Namatame, and A. Fujimori, *Electronic structure of 3d-transition-metal compounds by analysis of the 2p core-level photoemission spectra*, Phys. Rev. B **46**, 3771 (1992). 11, 27, 81, 129
- [Brandt & Mielsch 1989] U. Brandt and C. Mielsch, *Thermodynamics and correlation functions of the Falicov-Kimball model in large dimensions*, Z. Phys. B **75**, 365 (1989). 34
- [Brandt & Mielsch 1990] U. Brandt and C. Mielsch, *Thermodynamics of the Falicov-Kimball model in large dimensions II: Critical temperature and order parameter*, Z. Phys. B **79**, 295 (1990). 34
- [Brandt & Mielsch 1991] U. Brandt and C. Mielsch, *Free energy of the Falicov-Kimball model in large dimensions*, Z. Phys. B **82**, 37 (1991). 34
- [Bryan 1990] R. K. Bryan, *Maximum entropy analysis of oversampled data problems*, Eur. Biophys. J. **18**, 165 (1990). 47
- [Caffarel&Krauth 1994] M. Caffarel and W. Krauth, *Exact diagonalization approach to correlated fermions in infinite dimensions: Mott transition and superconductivity*, Phys. Rev. Lett. **72**, 1545 (1994). 33, 35
- [Carter et al. 1993] S. A. Carter, T. F. Rosenbaum, P. Metcalf, J. M. Honig, and J. Spalek, *Mass enhancement and magnetic order at the Mott-Hubbard transition*, Phys. Rev. B **48**, 16841 (1993). 25
- [Chahara et al. 1993] K. Chahara, T. Ohno, M. Kasai, and Y. Kozono, *Magnetoresistance in magnetic manganese oxide with intrinsic antiferromagnetic spin structure*, Appl. Phys. Lett. **63**, 1990 (1993). 10, 81, 128
- [Chainani et al. 1993] A. Chainani, M. Mathew, and D. D. Sarma, *Electron spectroscopic investigation of the semiconductor-metal transition in  $La_{1-x}Sr_xMnO_3$* , Phys. Rev. B **47**, 15 397 (1993). 11, 129



- [Chatterji et al. 2003] T. Chatterji, F. Fauth, B. Ouladdiaf, P. Mandal, and B. Ghosh, *Volume collapse in  $\text{LaMnO}_3$  caused by an orbital order-disorder transition*, Phys. Rev. B **68**, 052406 (2003). 72, 73, 76, 79, 80, 107
- [Ciuchi et al. 1997] S. Ciuchi, F. de Pasquale, S. Fratini, and D. Feinberg, *Dynamical mean-field theory of the small polaron*, Phys. Rev. B **56**, 4494 (1997). 23
- [Dagotto et al. 2001] E. Dagotto, T. Hotta, and A. Moreo, *Colossal magnetoresistant materials: the key role of phase separation*, Phys. Rep. **344**, 1 (2001). 9, 10, 11, 16, 28, 32, 82, 101, 128
- [Dederichs et al. 1984] P. H. Dederichs, S. Blügel, R. Zeller, and H. Akai, *Ground states of constrained systems: application to cerium impurities*, Phys. Rev. Lett. **53**, 2512 (1984). 31
- [Earl & Deem 2005] D. J. Earl and M. W. Deem, *Parallel tempering: Theory, application, and new perspectives*, 2005, cond-mat/0508111. 88
- [Edwards et al. 1999] D. M. Edwards, A. C. M. Green, and K. Kubo, *Electronic structure and resistivity of the double exchange model*, J. Phys.: Condens. Matter **11**, 10511 (1999). 17
- [Edwards 2002] D. M. Edwards, *Ferromagnetism and electron-phonon coupling in the manganites*, 2002, cond-mat/0201558. 17, 18, 75, 99, 101
- [Elemans et al. 1971] Jacqueline B. A. A. Elemans, B. van Laar, K. R. van der Veen, and B. O. Loopstra, *The crystallographic and magnetic structures of  $\text{La}_{1-x}\text{Ba}_x\text{Mn}_{1-x}\text{Me}_x\text{O}_3$  ( $\text{Me} = \text{Mn}$  or  $\text{Ti}$ )*, J. Solid State Chem. **3**, 238 (1971). 81
- [Fäth et al. 1999] M. Fäth, S. Freisem, A. A. Menovsky, Y. Tomioka, J. Aarts, and J. A. Mydosh, *Spatially inhomogeneous metal-insulator transition in doped manganites*, Science **285**, 1540 (1999). 84
- [Ferrari et al. 2001] V. Ferrari, M. J. Rozenberg, and R. Weht, *The anomalous metallic ferromagnetic state of Sr doped manganites*, Mod. Phys. Lett. B **15**, 1031 (2001), cond-mat/9906131. 26
- [Foulkes et al. 2001] W. M. C. Foulkes, L. Mitas, R. J. Needs, and G. Rajagopal, *Quantum Monte Carlo simulations of solids*, Rev. Mod. Phys. **73**, 33 (2001). 36, 40
- [Furukawa 1994] N. Furukawa, *Transport properties of the Kondo lattice model in the limit  $S = \infty$  and  $D = \infty$* , J. Phys. Soc. Japan **63**, 3214 (1994). 17

- [Furukawa 1998] N. Furukawa, *Thermodynamics of the double exchange systems*, 1998, `cond-mat/9812066`. 17
- [de Gennes 1960] P.-G de Gennes, *Effects of double exchange in magnetic crystals*, Phys. Rev. **118**, 141 (1960). 11, 16
- [Georges & Kotliar 1992] A. Georges and G. Kotliar, *Hubbard model in infinite dimensions*, Phys. Rev. B **45**, 6479 (1992). 34
- [Georges & Krauth 1992] A. Georges and W. Krauth, *Numerical solution of the  $d = \infty$  Hubbard model: Evidence for a Mott transition*, Phys. Rev. Lett. **69**, 1240 (1992). 33, 34, 35
- [Georges & Krauth 1993] A. Georges and W. Krauth, *Numerical solution of the  $d = \infty$  Hubbard model: Evidence for a Mott transition*, Phys. Rev. Lett. **48**, 7167 (1993). 33
- [Georges et al. 1996] A. Georges, G. Kotliar, W. Krauth, and M. J. Rozenberg, *Dynamical mean-field theory of strongly correlated fermion systems and the limit of infinite dimensions*, Rev. Mod. Phys. **68**, 13 (1996). 12, 27, 33, 34, 35, 47, 130
- [Goodenough 1955] J. B. Goodenough, *Theory of the role of covalence in the perovskite-type manganites  $[La, M(II)]MnO_3$* , Phys. Rev. **100**, 564 (1955). 11
- [Green & Edwards 1999] A. C. M. Green and D. M. Edwards, *Electronic structure and resistivity of the double exchange model*, J. Phys.: Condens. Matter **11**, 2791 (1999), [erratum, **12**, 9107 (2000)]. 17, 18
- [Gros 1994] C. Gros, *Equation-of-motion approach to the Hubbard model in infinite dimensions*, Phys. Rev. B **50**, 7295 (1994). 35
- [Gull & Daniell 1978] S. F. Gull and G. J. Daniell, *Image reconstruction from incomplete and noisy data*, Nature **272**, 686 (1978). 47
- [Gull 1989] S. F. Gull, Maximum entropy and Bayesian methods (J. Skilling, ed.), Kluwer Academic, Dordrecht, 1989, p. 53. 47
- [Gunnarsson et al. 1989] O. Gunnarsson, O. K. Andersen, O. Jepsen, and J. Zaanen, *Density-functional calculation of the parameters in the Anderson model: Application to Mn in CdTe*, Phys. Rev. B **39**, 1708 (1989). 31
- [Held 1999] K. Held, *Untersuchung korrelierter Elektronensysteme im Rahmen der Dynamischen Molekularfeld-Theorie*, Shaker Verlag, Aachen, 1999. 43, 47

- [Held & Vollhardt 2000] K. Held and D. Vollhardt, *Electronic correlations in manganites*, Phys. Rev. Lett. **84**, 5168 (2000). 12, 17, 25, 26, 101, 130
- [Held et al. 2001a] K. Held, G. Keller, V. Eyert, D. Vollhardt, and V. I. Anisimov, *Mott-Hubbard metal-insulator transition in paramagnetic  $V_2O_3$ : An LDA+DMFT(QMC) study*, Phys. Rev. Lett. **86**, 5345 (2001). 57
- [Held et al. 2001b] K. Held, A. K. McMahan, and R. T. Scalettar, *Cerium volume collapse: Results from the merger of dynamical mean-field theory and local density approximation*, Phys. Rev. Lett. **87**, 276404 (2001). 57
- [Held2003] K. Held, *Realistic investigations of correlated electron systems with LDA+DMFT*, Psi-k. Newsletter **56**, 65 (2003). 12, 130
- [Held2005] K. Held, *Electronic structure calculations with dynamical mean field theory*, 2005, cond-mat/0511293. 12
- [von Helmolt et al. 1993] R. von Helmolt, J. Wecker, B. Holzapfel, L. Schultz, and K. Samwer, *Giant negative magnetoresistance in perovskitelike  $La_{2/3}Ba_{1/3}MnO_x$  ferromagnetic films*, Phys. Rev. Lett. **71**, 2331 (1993). 10, 81, 128
- [Hettler et al. 1998] M. H. Hettler, A. N. Tahvildar-Zadeh, M. Jarrell, T. Pruschke, and H. R. Krishnamurthy, *Nonlocal dynamical correlations of strongly interacting electron systems*, Phys. Rev. B **58**, R7475 (1998). 74
- [Hewson 1993] A. C. Hewson, *The Kondo problem to heavy fermions*, Cambridge University Press, 1993. 35
- [Hibble et al. 1999] S. J. Hibble, S. P. Cooper, A. C. Hannon, I. D. Fawcett, and M. Greenblatt, *Local distortions in the colossal magnetoresistive manganates  $La_{0.70}Ca_{0.30}MnO_x$ ,  $La_{0.80}Ca_{0.20}MnO_x$  and  $La_{0.70}Sr_{0.30}MnO_x$  revealed by total neutron diffraction*, J. Phys.: Condens. Matter **11**, 9221 (1999). 81
- [Hirsch 1983] J. E. Hirsch, *Discrete Hubbard-Stratonovich transformation for fermion lattice models*, Phys. Rev. B **28**, 4059 (1983). 41
- [Hirsch & Fye 1986] J. E. Hirsch and R. M. Fye, *Monte Carlo method for magnetic impurities in metals*, Phys. Rev. Lett. **56**, 2521 (1986). 35, 39, 41
- [Hohenberg & Kohn 1964] P. Hohenberg and W. Kohn, *Inhomogeneous electron gas*, Phys. Rev. **136**, B864 (1964). 12, 55
- [Holstein 1959a] T. Holstein, *Studies of polaron motion: Part I. The molecular-crystal model*, Ann. Phys. (N.Y.) **8**, 325 (1959). 22

- [Holstein 1959b] T. Holstein, *Studies of polaron motion: Part II. The "small" polaron*, Ann. Phys. (N.Y.) **8**, 343 (1959). 22
- [Horsch et al. 1999] P. Horsch, J. Jaklič, and F. Mack, *Optical conductivity of colossal-magnetoresistance compounds: Role of orbital degeneracy in the ferromagnetic phase*, Phys. Rev. B **59**, 6217 (1999). 12, 81, 129
- [Hotta et al. 2001] T. Hotta, A. Feiguin, and E. Dagotto, *Stripes induced by orbital ordering in layered manganites*, Phys. Rev. Lett. **86**, 4922 (2001). 23
- [Iliev et al. 1998] M. N. Iliev, M. V. Abrashev, H.-G. Lee, V. N. Popov, Y. Y. Sun, C. Thomsen, R. L. Meng, and C. W. Chu, *Raman spectroscopy of orthorhombic perovskitelike  $YMnO_3$  and  $LaMnO_3$* , Phys. Rev. B **57**, 2872 (1998). 19, 20, 27, 28, 29, 30, 70, 72, 86, 105
- [Imada et al. 1998] M. Imada, A. Fujimori, and Y. Tokura, *Metal-insulator transitions*, Rev. Mod. Phys. **70**, 1039 (1998). 24, 25
- [Jahn & Teller 1937] H. A. Jahn and E. Teller, *Stability of polyatomic molecules in degenerate electronic states. I. Orbital degeneracy*, Proc. Roy. Soc. London A **161**, 220 (1937). 20
- [Janiš 1991] V. Janiš, *A new construction of thermodynamic mean-field theories of itinerant fermions: application to the Falicov-Kimball model*, Z. Phys. B **83**, 227 (1991). 34
- [Jarrell 1992] M. Jarrell, *Hubbard model in infinite dimensions: A quantum Monte Carlo study*, Phys. Rev. Lett. **69**, 168 (1992). 34, 35
- [Jarrell & Gubernatis 1996] M. Jarrell and J. E. Gubernatis, *Bayesian inference and the analytic continuation of imaginary-time quantum Monte Carlo data*, Phys. Rep. **269**, 133 (1996). 45, 47
- [Jin et al. 1994] S. Jin, T. H. Tiefel, M. McCormack, R. A. Fastnacht, R. Ramesh, and L. H. Chen, *Thousandfold change in resistivity in magnetoresistive  $La-Ca-Mn-O$  films*, Science **264**, 413 (1994). 10, 81, 128
- [Jones & Gunnarsson 1989] R. O. Jones and O. Gunnarsson, *The density functional formalism, its applications and prospects*, Rev. Mod. Phys. **61**, 689 (1989). 12, 54, 56
- [Jonker & Santen 1950] G. H. Jonker and J. H. Van Santen, *Ferromagnetic compounds of manganese with perovskite structure*, Physica **16**, 337 (1950). 10, 16, 128

- [Jung et al. 1998] J. H. Jung, K. H. Kim, T. W. Noh, E. J. Choi, and J. Yu, *Midgap states of  $La_{1-x}Ca_xMnO_3$ : Doping-dependent optical-conductivity studies*, Phys. Rev. B **57**, R11 043 (1998). 11, 30, 50, 61, 67, 75, 81, 82, 89, 94, 95, 96, 104, 106, 107, 108, 129
- [Kanamori 1960] J. Kanamori, *Crystal distortion in magnetic compounds*, J. Appl. Phys. **31**, 14S (1960). 20, 22, 73, 74
- [Katsnelson & Lichtenstein2000] M. I. Katsnelson and A. I. Lichtenstein, *First-principles calculations of magnetic interactions in correlated systems*, Phys. Rev. B **61**, 8906 (2000). 12
- [Kilian & Khaliullin 1998] R. Kilian and G. Khaliullin, *Orbital dynamics: The origin of the anomalous optical spectra in ferromagnetic manganites*, Phys. Rev. B **58**, R11 841 (1998). 12, 81, 129
- [Kohn & Sham 1964] W. Kohn and L. J. Sham, *Quantum density oscillations in an inhomogeneous electron gas*, Phys. Rev. **137**, A1697 (1964). 12, 56
- [Kohn & Sham 1965] W. Kohn and L. J. Sham, *Self-consistent equations including exchange and correlation effects*, Phys. Rev. **140**, A1133 (1965). 12, 56
- [Kotliar et al. 2001] G. Kotliar, S. Y. Savrasov, G. Pálsson, and G. Biroli, *Cellular dynamical mean field approach to strongly correlated systems*, Phys. Rev. Lett. **87**, 186401 (2001). 74, 108
- [Kotliar et al. 2006] G. Kotliar, S. Y. Savrasov, K. Haule, V. S. Oudovenko, O. Parcollet, and C.A. Marianetti, *Electronic structure calculations with dynamical mean-field theory*, Rev. Mod. Phys. **78**, 865 (2006), cond-mat/0511085. 74, 108
- [Kovaleva et al. 2004] N. N. Kovaleva, A. V. Boris, C. Bernhard, A. Kulakov, A. Pimenov, A. M. Balbashov, G. Khaliullin, and B. Keimer, *Spin-controlled Mott-Hubbard bands in  $LaMnO_3$  probed by optical ellipsometry*, Phys. Rev. Lett. **93**, 147204 (2004). 32, 108
- [Kubo & Ohata 1972] K. Kubo and N. Ohata, *A quantum theory of double exchange. I*, J. Phys. Soc. Japan **33**, 21 (1972). 11, 16, 129
- [Kuramoto & Watanabe 1987] Y. Kuramoto and T. Watanabe, *Theory of momentum-dependent magnetic response in heavy-fermion systems*, Physica B **148**, 80 (1987). 34
- [Kuwahara et al.1995] H. Kuwahara, Y. Tomioka, A. Asamitsu, Y. Moritomo, and Y. Tokura, *A first-order phase transition induced by a magnetic field*, Science **270**, 961 (1995). 11

- [Laad et al. 2003] M. S. Laad, L. Craco, and E. Müller-Hartmann, *Orbital switching and the first-order insulator-metal transition in paramagnetic  $V_2O_3$* , Phys. Rev. Lett. **91**, 156402 (2003). 57
- [Laloux et al. 1994] L. Laloux, A. Georges, and W. Krauth, *Effect of a magnetic field on Mott-Hubbard systems*, Phys. Rev. B **50**, 3092 (1994). 33
- [Levy 1982] Mel Levy, *Electron densities in search of Hamiltonians*, Phys. Rev. A **26**, 1200 (1982). 55
- [Lichtenstein & Katsnelson 1998] A. I. Lichtenstein and M. I. Katsnelson, *Ab initio calculations of quasiparticle band structure in correlated systems: LDA++ approach*, Phys. Rev. B **57**, 6884 (1998). 12
- [Lichtenstein & Katsnelson 2000] A. I. Lichtenstein and M. I. Katsnelson, *Antiferromagnetism and d-wave superconductivity in cuprates: A cluster dynamical mean-field theory*, Phys. Rev. B **62**, R9283 (2000). 74
- [Lichtenstein et al. 2001] A. I. Lichtenstein, M. I. Katsnelson, and G. Kotliar, *Finite-temperature magnetism of transition metals: An ab initio dynamical mean-field theory*, Phys. Rev. Lett. **87**, 067205 (2001). 57
- [Liebsch & Lichtenstein 2000] A. Liebsch and A. Lichtenstein, *Photoemission quasiparticle spectra of  $Sr_2RuO_4$* , Phys. Rev. Lett. **84**, 1591 (2000). 57
- [Loa et al. 2001] I. Loa, P. Adler, A. Grzechnik, K. Syassen, U. Schwarz, M. Hanfland, G. Kh. Rozenberg, P. Gorodetsky, and M. P. Pasternak, *Pressure-induced quenching of the Jahn-Teller distortion and insulator-to-metal transition in  $LaMnO_3$* , Phys. Rev. Lett. **87**, 125501 (2001). 11, 12, 25, 59, 60, 61, 62, 63, 64, 68, 69, 70, 80, 107, 129, 130, 131
- [Mahan 2000] G. D. Mahan, *Many-particle physics*, 3. ed., Kluwer Academic, Plenum Publisher, New York, 2000. 50
- [Majumdar et al. 1999] P. Majumdar, S. H. Simon, and A. M. Sengupta, *Hall effect in the perovskite manganites*, Phys. Rev. B **59**, 4746 (1999). 23
- [Mathieu et al. 2006] R. Mathieu, M. Uchida, Y. Kaneko, J. P. He, X. Z. Yu, R. Kumai, T. Arima, Y. Tomioka, A. Asamitsu, Y. Matsui, and Y. Tokura, *Bandwidth-disorder phase diagram of half doped layered manganites*, Phys. Rev. B **74**, 020404(R) (2006). 11, 129
- [Mayr et al. 2001] M. Mayr, A. Moreo, J. A. Vergés, J. Arispe, A. Feiguin, and E. Dagotto, *Resistivity of Mixed-Phase Manganites*, Phys. Rev. Lett. **86**, 135 (2001). 12, 18, 81, 129

- [McMahan et al. 2003] A. K. McMahan, K. Held, and R. T. Scalettar, *Thermodynamic and spectral properties of compressed Ce calculated using a combined local-density approximation and dynamical mean-field theory*, Phys. Rev. B **67**, 075108 (2003). 57
- [Meskine & Satpathy 1999] H. Meskine and S. Satpathy, *Jahn-Teller coupling and double exchange in the two-site Van Vleck-Kanamori model*, J. Appl. Phys. **85**, 4346 (1999). 72, 73
- [Metropolis et al. 1953] Nicholas Metropolis, Arianna W. Rosenbluth, Marshall N. Rosenbluth, Augusta H. Teller, and Edward Teller, *Equation of state calculations by fast computing machines*, J. Chem. Phys. **21**, 1087 (1953). 39
- [Metzner & Vollhardt 1989] W. Metzner and D. Vollhardt, *Correlated lattice fermions in  $d = \infty$  dimensions*, Phys. Rev. Lett. **62**, 324 (1989). 33
- [Millis et al. 1995] A. J. Millis, P. B. Littlewood, and B. I. Shraiman, *Double exchange alone does not explain the resistivity of  $La_{1-x}Sr_xMnO_3$* , Phys. Rev. Lett. **74**, 5144 (1995). 12, 17, 18, 23, 26, 63, 101, 129
- [Millis et al. 1996b] A. J. Millis, R. Mueller, and B. I. Shraiman, *Fermi-liquid-to-polaron crossover. I. General results*, Phys. Rev. B **54**, 5389 (1996). 12, 23
- [Millis et al. 1996c] A. J. Millis, R. Mueller, and B. I. Shraiman, *Fermi-liquid-to-polaron crossover. II. Double exchange and the physics of colossal magnetoresistance*, Phys. Rev. B **54**, 5405 (1996). 12, 23, 27, 72, 73, 99
- [Millis et al. 1996a] A. J. Millis, B. I. Shraiman, and R. Mueller, *Dynamic Jahn-Teller effect and colossal magnetoresistance in  $La_{1-x}Sr_xMnO_3$* , Phys. Rev. Lett. **77**, 175 (1996). 12, 23, 81, 89, 101, 107, 129
- [Millis 1998] A. J. Millis, *Lattice effects in magnetoresistive manganese perovskites*, Nature **392**, 147 (1998). 9, 11, 128
- [Moeller et al. 1995] G. Moeller, Q. Si, G. Kotliar, M. Rozenberg, and D. S. Fisher, *Critical Behavior near the Mott Transition in the Hubbard Model*, Phys. Rev. Lett. **74**, 2082 (1995). 33
- [Moreno et al. 2003] J. J. Moreno, H. G. Katzgraber, and A. K. Hartmann, *Finding low-temperature states with parallel tempering, simulated annealing and simple Monte Carlo*, Int. J. Mod. Phys. C **14**, 285 (2003), cond-mat/0209248. 88

- [Moreo et al. 2000] A. Moreo, M. Mayr, A. Feiguin, S. Yunoki, and E. Dagotto, *Giant cluster coexistence in doped manganites and other compounds*, Phys. Rev. Lett. **84**, 5568 (2000). 81
- [Moritomo et al. 1997] Y. Moritomo, H. Kuwahara, Y. Tomioka, and Y. Tokura, *Pressure effects on charge-ordering transitions in perovskite manganites*, Phys. Rev. B **55**, 7549 (1997). 11
- [Motome & Imada 1999a] Y. Motome and M. Imada, *Effects of electron correlation, orbital degeneracy and Jahn-Teller coupling in perovskite manganites*, J. Phys. Soc. Japan **68**, 16 (1999). 26
- [Motome & Imada 1999b] Y. Motome and M. Imada, *Ordering and fluctuation of orbital and lattice distortion in perovskite manganese oxides*, Phys. Rev. B **60**, 7921 (1999). 26
- [Mukhin et al. 1998] A. A. Mukhin, V. Yu. Ivanov, V. D. Travkin, S. P. Lebedev, A. Pimenov, A. Loidl, and A. M. Balbashov, *Magnetic and structural transitions in  $La_{1-x}Sr_xMnO_3$ :  $T$ - $x$  phase diagram*, Pis'ma Zh. Éksp. Teor. Fiz. **68**, 331 (1998), [JETP Lett. 68, 356 (1998)]. 11, 60
- [Müller-Hartmann 1989a] E. Müller-Hartmann, *Correlated fermions on a lattice in high dimensions*, Z. Phys. B **74**, 507 (1989). 34
- [Müller-Hartmann 1989b] E. Müller-Hartmann, *Fermions on a lattice in high dimensions*, Int. J. Mod. Phys. B **3**, 2169 (1989). 34
- [Müller-Hartmann 1989c] E. Müller-Hartmann, *The Hubbard model at high dimensions: some exact results and weak coupling theory*, Z. Phys. B **76**, 211 (1989). 34
- [Nekrasov et al. 2000] I. A. Nekrasov, K. Held, N. Blümer, A. I. Poteryaev, V. I. Anisimov, and D. Vollhardt, *Calculation of photoemission spectra of the doped Mott insulator  $La_{1-x}Sr_xTiO_3$  using LDA+DMFT(QMC)*, Eur. Phys. J. B **18**, 55 (2000). 57
- [Nekrasov et al. 2002] I. A. Nekrasov, G. Keller, D. E. Kondakov, A. V. Kozhevnikov, Th. Pruschke, K. Held, D. Vollhardt, and V. I. Anisimov, *Explanation of the similarity of the experimental photoemission spectra of  $SrVO_3$  and  $CaVO_3$* , 2002, cond-mat/0211508. 57
- [Nekrasov et al. 2005] I. A. Nekrasov, G. Keller, D. E. Kondakov, A. V. Kozhevnikov, Th. Pruschke, K. Held, D. Vollhardt, and V. I. Anisimov, *Comparative study of correlation effects in  $CaVO_3$  and  $SrVO_3$* , Phys. Rev. B **72**, 155106 (2005). 57



- [Obradors et al. 1993] X. Obradors, L. M. Paulius, M. B. Maple, J. B. Torrance, A. I. Nazzal, J. Fontcuberta, and X. Granados, *Pressure dependence of the metal-insulator transition in the charge-transfer oxides  $RNiO_3$  ( $R=Pr, Nd, Nd_{0.7}La_{0.3}$ )*, Phys. Rev. B **47**, 12353 (1993). 25
- [Ohkawa 1991a] F. J. Ohkawa, *Electron correlation in the Hubbard-model in  $d = \infty$  dimension*, J. Phys. Soc. Japan **60**, 3218 (1991). 34
- [Ohkawa 1991b] F. J. Ohkawa, *Heavy electrons in the Mott-transition region*, Prog. Theor. Phys. Suppl. **106**, 95 (1991). 34
- [Ohsawa & Inoue 2002] T. Ohsawa and J.-I. Inoue, *Magnetic structure of low electron density manganites*, Phys. Rev. B **65**, 134442 (2002). 23
- [Okimoto et al. 1995] Y. Okimoto, T. Katsufuji, T. Ishikawa, A. Urushibara, T. Arima, and Y. Tokura, *Anomalous variation of optical spectra with spin polarization in double-exchange ferromagnet:  $La_{1-x}Sr_xMnO_3$* , Phys. Rev. Lett. **75**, 109 (1995). 11, 30, 50, 81, 82, 84, 94, 104, 108, 129
- [Okimoto et al. 1997] Y. Okimoto, T. Katsufuji, T. Arima, and Y. Tokura, *Variation of electronic structure in  $La_{1-x}Sr_xMnO_3$  ( $x \leq x \leq 0.3$ ) as investigated by optical conductivity spectra*, Phys. Rev. B **55**, 4206 (1997). 81, 82, 84, 85, 95
- [Park et al. 1996] J.-H. Park, C. T. Chen, S-W. Cheong, W. Bao, G. Meigs, V. Chakarian, and Y. U. Idzerda, *Electronic aspects of the ferromagnetic transition in manganese perovskites*, Phys. Rev. Lett. **76**, 4215 (1996). 11, 27, 31, 32, 66, 86, 108, 129
- [Pavarini et al. 2004] E. Pavarini, S. Biermann, A. Poteryaev, A. I. Lichtenstein, A. Georges, and O. K. Andersen, *Mott transition and suppression of orbital fluctuations in orthorhombic  $3d^1$  perovskites*, Phys. Rev. Lett. **92**, 176403 (2004). 57, 64
- [Pavarini et al. 2005] E. Pavarini, A. Yamasaki, J. Nuss, and O. K. Andersen, *How chemistry controls electron localization in  $3d^1$  perovskites: a Wannier-function study*, New J. Phys. **7**, 188 (2005). 57, 64
- [Perebeinos & Allen 2000] V. Perebeinos and P. B. Allen, *Franck-Condon-broadened angle-resolved photoemission spectra predicted in  $LaMnO_3$* , Phys. Rev. Lett. **85**, 5178 (2000). 27, 81
- [Perring et al. 1997] T. G. Perring, G. Aeppli, Y. Moritomo, and Y. Tokura, *Antiferromagnetic short range order in a two-dimensional manganite exhibiting giant magnetoresistance*, Phys. Rev. Lett. **78**, 3197 (1997). 101

- [Pickett&Singh 1996] W. E. Pickett and D. J. Singh, *Electronic structure and half-metallic transport in the  $La_{1-x}Ca_xMnO_3$  system*, Phys. Rev. B **53**, 1146 (1996). 72, 81
- [Popovic & Satpathy 2000] Z. Popovic and S. Satpathy, *Cooperative Jahn-Teller coupling in the manganites*, Phys. Rev. Lett. **84**, 1603 (2000). 22, 27, 72, 73, 74, 81
- [Popović & Satpathy 2002] Z. Popović and S. Satpathy, *Origin of charge-orbital order in the half-doped manganites*, Phys. Rev. Lett. **88**, 197201 (2002). 11
- [Potthoff et al. 2003] M. Potthoff, M. Aichhorn, and C. Dahnken, *Variational cluster approach to correlated electron systems in low dimensions*, Phys. Rev. Lett. **91**, 206402 (2003). 74, 108
- [Pruschke et al. 1993a] Th. Pruschke, D. L. Cox, and M. Jarrell, *Hubbard model at infinite dimensions: Thermodynamic and transport properties*, Phys. Rev. B **47**, 3553 (1993). 33, 35, 51
- [Pruschke et al. 1993b] Th. Pruschke, D. L. Cox, and M. Jarrell, *Transport-properties of the infinite-dimensional Hubbard-model*, Europhys. Lett. **21**, 593 (1993). 33
- [Quijada et al. 1998] M. Quijada, J. Černe, J. R. Simpson, H. D. Drew, K. H. Ahn, A. J. Millis, R. Shreekala, R. Rarnesh, M. Rajeswari, and T. Venkatesan, *Optical conductivity of manganites: Crossover from Jahn-Teller small polaron to coherent transport in the ferromagnetic state*, Phys. Rev. B **58**, 16 093 (1998). 11, 81, 82, 95, 104, 106, 108, 129
- [Ramakrishnan et al. 2004] T. V. Ramakrishnan, H. R. Krishnamurthy, S. R. Hassan, and G. V. Pai, *Theory of insulator metal transition and colossal magnetoresistance in doped manganites*, Phys. Rev. Lett. **92**, 157203 (2004). 89, 129
- [Röder et al. 1996] H. Röder, J. Zang, and A. R. Bishop, *Lattice effects in the colossal-magnetoresistance manganites*, Phys. Rev. Lett. **76**, 1356 (1996). 12, 23, 81, 101, 129
- [Rozenberg et al. 1992] M. J. Rozenberg, X. Y. Zhang, and G. Kotliar, *Mott-Hubbard transition in infinite dimensions*, Phys. Rev. Lett. **69**, 1236 (1992). 33, 35
- [Rozenberg et al. 1994a] M. J. Rozenberg, G. Kotliar, and X. Y. Zhang, *Mott-Hubbard transition in infinite dimensions. II*, Phys. Rev. B **49**, 10181 (1994). 33

- [Rozenberg et al. 1994b] M. J. Rozenberg, G. Moeller, and G. Kotliar, *The metal-insulator transition in the Hubbard model at zero temperature II*, Mod. Phys. Lett. B **8**, 535 (1994). 33
- [Rozenberg 1998] M. J. Rozenberg, *A scenario for the electronic state in the manganese perovskites: the orbital correlated metal*, Eur. Phys. J. B **2**, 457 (1998). 26
- [Saitoh et al. 1997] T. Saitoh, A. Sekiyama, K. Kobayashi, T. Mizokawa, A. Fujimori, D. D. Sarma, Y. Takeda, and M. Takano, *Temperature-dependent valence-band photoemission spectra of  $La_{1-x}Sr_xMnO_3$* , Phys. Rev. B **56**, 8836 (1997). 11, 129
- [Sakai & Kuramoto 1994] O. Sakai and Y. Kuramoto, *Application of the numerical renormalization group method to the hubbard model in infinite dimensions*, Solid State Commun. **89**, 207 (1994). 35
- [Salamon & Jaime 2001] M. B. Salamon and M. Jaime, *The physics of manganites: Structure and transport*, Rev. Mod. Phys. **73**, 583 (2001). 9, 11, 82, 128
- [Santen & Jonker 1950] J. H. Van Santen and G. H. Jonker, *Electrical conductivity of ferromagnetic compounds of manganese with perovskite structure*, Physica **16**, 599 (1950). 10, 16, 128
- [Satpathy et al. 1996a] S. Satpathy, Z. S. Popović, and F. R. Vukajlović, *Density-functional studies of the electronic structure of the perovskite oxides:  $La_{1-x}Ca_xMnO_3$* , J. Appl. Phys. **79**, 4555 (1996). 27, 31, 72, 73, 81
- [Satpathy et al. 1996b] S. Satpathy, Z. S. Popović, and F. R. Vukajlović, *Electronic structure of the perovskite oxides:  $La_{1-x}Ca_xMnO_3$* , Phys. Rev. Lett. **76**, 960 (1996). 27, 81
- [Savrasov & Kotliar 2004] S. Y. Savrasov and G. Kotliar, *Spectral density functionals for electronic structure calculations*, Phys. Rev. B **69**, 245101 (2004). 57
- [Sham & Kohn 1966] L. J. Sham and W. Kohn, *One-particle properties of an inhomogeneous interacting electron gas*, Phys. Rev. **145**, 561 (1966). 12, 56
- [Si et al. 1994] Q. Si, M. J. Rozenberg, G. Kotliar, and A. E. Ruckenstein, *Correlation induced insulator to metal transitions*, Phys. Rev. Lett. **72**, 2761 (1994). 35
- [Skilling & Bryan 1984] J. Skilling and R. K. Bryan, *Maximum entropy image reconstruction - general algorithm*, Mon. Not. R. astr. Soc. **211**, 111 (1984). 47

- [Skilling 1989] J. Skilling, Maximum entropy and Bayesian methods (J. Skilling, ed.), Kluwer Academic, Dordrecht, 1989, p. 45. 46
- [Slater & Koster 1954] J. C. Slater and G. F. Koster, *Simplified LCAO method for the periodic potential problem*, Phys. Rev. **94**, 1498 (1954). 27, 28
- [Solovyev & Dederichs 1994] I. V. Solovyev and P. H. Dederichs, *Ab initio calculations of Coulomb  $U$  parameters for transition-metal impurities*, Phys. Rev. B **49**, 6736 (1994). 31
- [Sumi 1972] H. Sumi, *Polaron conduction from band to hopping types*, J. Phys. Soc. Japan **33**, 327 (1972). 23
- [Sumi 1974] H. Sumi, *Exciton polarons of molecular crystal model. I. — Dynamical CPA* —, J. Phys. Soc. Japan **36**, 770 (1974). 23
- [Swendsen & Wang 1986] R. H. Swendsen and Jian-Sheng Wang, *Replica Monte Carlo simulation of spin-glasses*, Phys. Rev. Lett. **57**, 2607 (1986). 88
- [Takenaka et al. 1999] K. Takenaka, K. Iida, Y. Sawaki, S. Sugai, Y. Moritomo, and A. Nakamura, *Optical reflectivity spectra measured on cleaved surface of  $La_{1-x}Sr_xMnO_3$ : Evidence against extremely small Drude weight*, J. Phys. Soc. Japan **68**, 1828 (1999). 11, 30, 50, 61, 67, 75, 81, 82, 83, 84, 94, 104, 108, 129
- [Tobe et al. 2004] K. Tobe, T. Kimura, and Y. Tokura, *Anisotropic optical spectra of doped manganites with pseudocubic perovskite structure*, Phys. Rev. B **69**, 014407 (2004). 30, 50, 94
- [Tokura et al. 1994] Y. Tokura, A. Urushibara, Y. Moritomo, T. Arima, A. Asamitsu, G. Kido, and N. Furukawa, *Giant magnetotransport phenomena in filling-controlled Kondo lattice system:  $La_{1-x}Sr_xMnO_3$* , J. Phys. Soc. Japan **63**, 3931 (1994). 11, 81, 82, 83, 104, 108
- [Tokura et al. 1996] Y. Tokura, Y. Tomioka, H. Kuwahara, A. Asamitsu, Y. Moritomo, and M. Kasai, *Origins of colossal magnetoresistance in perovskite-type manganese oxides (invited)*, J. Appl. Phys. **79**, 5288 (1996). 11, 82, 128
- [Tokura & Tomioka 1999] Y. Tokura and Y. Tomioka, *Colossal magnetoresistive manganites*, J. Magn. Magn. Mater. **200**, 1 (1999). 11, 82
- [Tokura 2003] Y. Tokura, *Correlated-electron physics in transition-metal oxides*, Physics Today **56(7)**, 50 (2003). 11

- [Tomioka et al.1995a] Y. Tomioka, A. Asamitsu, Y. Moritomo, H. Kuwahara, and Y. Tokura, *Collapse of a charge-ordered state under a magnetic field in  $Pr_{1/2}Sr_{1/2}MnO_3$* , Phys. Rev. Lett. **74**, 5108 (1995). 11
- [Tomioka et al.1995b] Y. Tomioka, A. Asamitsu, Y. Moritomo, and Y. Tokura, *Anomalous magnetotransport properties of  $Pr_{1-x}Ca_xMnO_3$* , J. Phys. Soc. Japan **64**, 3626 (1995). 11
- [Tomioka et al. 1996] Y. Tomioka, A. Asamitsu, H. Kuwahara, Y. Moritomo, and Y. Tokura, *Magnetic-field-induced metal-insulator phenomena in  $Pr_{1-x}Ca_xMnO_3$  with controlled charge-ordering instability*, Phys. Rev. B **53**, R1689 (1996). 11
- [Tomioka et al. 1997] Y. Tomioka, A. Asamitsu, H. Kuwahara, and Y. Tokura, *Reentrant transition of the charge-ordered state in perovskite manganites*, J. Phys. Soc. Japan **66**, 302 (1997). 11
- [Tomioka & Tokura 2004] Y. Tomioka and Y. Tokura, *Global phase diagram of perovskite manganites in the plane of quenched disorder versus one-electron bandwidth*, Phys. Rev. B **70**, 014432 (2004). 11, 129
- [Urushibara et al.1995] A. Urushibara, Y. Moritomo, T. Arima, A. Asamitsu, G. Kido, and Y. Tokura, *Insulator-metal transition and giant magnetoresistance in  $La_{1-x}Sr_xMnO_3$* , Phys. Rev. B **51**, 14 103 (1995). 11, 82, 83, 104, 108
- [Varma 1996] C. M. Varma, *Electronic and magnetic states in the giant magnetoresistive compounds*, Phys. Rev. B **54**, 7328 (1996). 12, 81, 129
- [Wollan & Koehler 1955] E. O. Wollan and W. C. Koehler, *Neutron diffraction study of the magnetic properties of the series of perovskite-type compounds  $[(1-x)La, xCa]MnO_3$* , Phys. Rev. **100**, 545 (1955). 10, 128
- [Xiong et al. 1995] G. C. Xiong, Q. Li, H. L. Ju, S. N. Mao, L. Senapati, X. X. Xi, R. L. Greene, and T. Venkatesan, *Giant magnetoresistance in epitaxial  $Nd_{0.7}Sr_{0.3}MnO_{3-\delta}$  thin films*, Appl. Phys. Lett. **66**, 1427 (1995). 11, 128
- [Yamada 1975] K. Yamada, *Perturbation expansion for the Anderson Hamiltonian. II*, Prog. Theor. Phys. **53**, 970 (1975). 35
- [Yamasaki et al. 2006] A. Yamasaki, M. Feldbacher, Y.-F. Yang, O. K. Andersen, and K. Held, *Pressure-induced metal-insulator transition in  $LaMnO_3$  is not of Mott-Hubbard type*, Phys. Rev. Lett. **96**, 166401 (2006). 12, 17, 28, 31, 32, 63, 105

- [Yang & Held 2006] Y.-F. Yang and K. Held, *Localization of strongly correlated electrons as Jahn-Teller polarons in manganites*, 2006, cond-mat/0603553. 86, 107
- [Yin et al. 2006] W. Yin, D. Volja, and W. Ku, *Orbital ordering in  $\text{LaMnO}_3$ : Electron-electron versus electron-lattice interactions*, Phys. Rev. Lett. **96**, 1166405 (2006). 11, 72, 74
- [Yosida & Yamada 1975] K. Yosida and K. Yamada, *Perturbation expansion for the Anderson Hamiltonian. III*, Prog. Theor. Phys. **53**, 1286 (1975). 35
- [Yunoki et al. 1998] S. Yunoki, J. Hu, A. L. Malvezzi, A. Moreo, N. Furukawa, and E. Dagotto, *Phase separation in electronic models for manganites*, Phys. Rev. Lett. **80**, 845 (1998). 12, 18, 81, 101, 129
- [Zaanen et al. 1985] J. Zaanen, G. A. Sawatzky, and J. W. Allen, *Band gaps and electronic structure of transition-metal compounds*, Phys. Rev. Lett. **55**, 418 (1985). 31
- [Zampieri et al. 1998] G. Zampieri, F. Prado, A. Caneiro, J. Briático, M. T. Causa, M. Tovar, B. Alascio, M. Abbate, and E. Morikawa, *Electronic structure of  $\text{CaMnO}_x$  with  $2.66 \leq x \leq 3.00$  studied with photoemission and x-ray-absorption spectroscopy*, Phys. Rev. B **58**, 3755 (1998). 27, 81
- [Zang et al. 1996] J. Zang, A. R. Bishop, and H. Röder, *Double degeneracy and Jahn-Teller effects in colossal-magnetoresistance perovskites*, Phys. Rev. B **53**, R8840 (1996). 23
- [Zener 1951a] C. Zener, *Interaction between the d shells in the transition metals*, Phys. Rev. **81**, 440 (1951). 11, 15, 81, 129
- [Zener 1951b] C. Zener, *Interaction between the d-shells in the transition metals. II. Ferromagnetic compounds of manganese with perovskite structure*, Phys. Rev. **82**, 403 (1951). 11, 15, 25, 81, 129
- [Zenia et al. 2005] H. Zenia, G. A. Gehring, and W. M. Temmerman, *Orbital ordering in cubic  $\text{LaMnO}_3$  from first principles calculations*, New J. Phys. **7**, 257 (2005). 12, 59, 70, 107
- [Zhang et al. 1993] X. Y. Zhang, M. J. Rozenberg, and G. Kotliar, *Mott transition in the  $d = \infty$  Hubbard model at zero temperature*, Phys. Rev. Lett. **70**, 1666 (1993). 33
- [Zöfl et al. 2000] M. B. Zöfl, Th. Pruschke, J. Keller, A. I. Poteryaev, I. A. Nekrasov, and V. I. Anisimov, *Combining density-functional and*

- dynamical-mean-field theory for  $La_{1-x}Sr_xTiO_3$ ,*  
Phys. Rev. B **61**, 12810 (2000). 57
- [Zölf et al. 2001] M. B. Zölf, I. A. Nekrasov, Th. Pruschke, V. I. Anisimov, and J. Keller, *Spectral and magnetic properties of  $\alpha$ - and  $\gamma$ -Ce from dynamical mean-field theory and local density approximation,*  
Phys. Rev. Lett. **87**, 276403 (2001). 57
- [Zurek et al. 2005] E. Zurek, O. Jepsen, and O. K. Andersen, *Muffin-tin orbital Wannier-like functions for insulators and metals,*  
ChemPhysChem **6**, 1934 (2005), cond-mat/0504374. 57, 64

## Publications

- Y.-F. Yang and K. Held, *Nonequilibrium transport through parallel double quantum dots in the Kondo regime*, Phys. Rev. B **72**, 235308 (2005).
- A. Yamasaki, M. Feldbacher, Y.-F. Yang, O. K. Andersen, and K. Held, *Pressure-induced metal-insulator transition in  $\text{LaMnO}_3$  is not of Mott-Hubbard type*, Phys. Rev. Lett. **96**, 166401 (2006).
- Y.-F. Yang and K. Held, *Localization of strongly correlated electrons as Jahn-Teller polarons in manganites*, cond-mat/0603553.
- K. Byczuk, M. Kollar, K. Held, Y.-F. Yang, I. A. Nekrasov, Th. Pruschke, and D. Vollhardt, *Kinks in the dispersion of strongly correlated electrons*, cond-mat/0609594.



## Acknowledgments

First of all I would like to thank Prof. Walter Metzner for giving me the opportunity to finish my Ph.D. work at the Max-Planck-Institut in Stuttgart. I wish to thank Dr. Karsten Held for proposing this interesting subject and for many discussions during the work. The collaboration with Dr. Atsushi Yamasaki, Prof. Ole Krogh Andersen, and Dr. Martin Feldbacher is a great pleasure for me. I am grateful to Dr. Jong E Han and Dr. Oliver Rösch for the very helpful discussions. I would like to thank Prof. Alejandro Muramatsu for co-examining the thesis.

I wish to thank Dr. Alessandro Toschi and Dr. Andrey Katanin for a careful reading of the manuscript. I extend my thanks to all the people in the theory group for their help and the friendly atmosphere. I have learned a lot from them. I would also like to thank our secretary Mrs. Ingrid Knapp for her help in all organizational matters, and the computer service group for their support. My thank also goes to the secretary Dr. Hans-Georg Libuda of the International Max Planck Research School for Advanced Materials.

Last but not least I am indebted to my parents for their continuous understanding and encouragement during these years.

## Deutsche Zusammenfassung

Wegen des kolossalen Magnetowiderstandes (CMR) wurden Manganate  $T_{1-x}D_x\text{MnO}_3$  (T: La, Pr, Nd, . . . ; D: Ca, Sr, . . .) in den letzten Jahren intensiv studiert [Millis 1998, Salamon & Jaime 2001, Dagotto et al. 2001]. Diese Materialien haben eine Perowskit-Struktur, wobei jedes Mn-Ion oktaedrisch von sechs Sauerstoff-Ionen umgeben ist. Von den Orbitalen tragen nur die 3d-Orbitale des Mangans zum thermischen und elektrischen Transport bei, da alle anderen Orbitale bei höheren Energien d.h. weiter weg von der Fermi-Energie liegen. Durch den Einfluss des kubischen Kristallfelds werden die fünf 3d-Orbitale in zwei  $e_g$ -Orbitale ( $d_{3z^2-r^2}$  und  $d_{x^2-y^2}$ ) und drei  $t_{2g}$ -Orbitale ( $d_{xy}$ ,  $d_{yz}$ , und  $d_{zx}$ ) aufgespalten. Nach der Hund'schen Regel werden die drei  $t_{2g}$ -Orbitale von drei Elektronen mit parallelem Spin (ein lokalisierter Spin  $|\mathbf{S}| = 3/2$ ) besetzt, und die restliche  $1 - x$  Elektronen besetzen die zwei  $e_g$ -Orbitale.

Perowskit-Manganate haben ein komplexes Phasendiagramm. Entdeckt wurde zuerst die Existenz des Ferromagnetismus in Mischkristallen  $\text{LaMnO}_3\text{-CaMnO}_3$ ,  $\text{LaMnO}_3\text{-SrMnO}_3$  und  $\text{LaMnO}_3\text{-BaMnO}_3$  [Jonker & Santen 1950, Santen & Jonker 1950]. Später wurde auch eine antiferromagnetische Phase in  $\text{La}_{1-x}\text{Ca}_x\text{MnO}_3$  mit Ladungs- und Orbital-Ordnungen charakterisiert [Wollan & Koehler 1955].

Der CMR-Effekt kann durch das Magnetowiderstandsverhältnis  $\eta = \delta R/R(H) = (R(0) - R(H))/R(H)$  oder  $\eta' = \delta R/R(0) = (R(0) - R(H))/R(0)$  beschrieben werden. Hierbei ist  $R(0)$  der Nullfeld-Widerstand und  $R(H)$  der Widerstand im Magnetfeld  $H$ . Ein großer Magnetowiderstand ( $\eta' = 50\%$ ), der 1993 in dünnen Filmen im externen Magnetfeld beobachtet wurde [Chahara et al. 1993, von Helmlolt et al. 1993], hat in den letzten Jahren großes Interesse geweckt. In einem  $\text{La}_{0.67}\text{Ca}_{0.33}\text{MnO}_x$  Film wurde für  $\eta$  ein Wert von 127,000% gefunden [Jin et al. 1994]. Daher wurde die Bezeichnung kolossaler Magnetowiderstand eingeführt. Auch in  $\text{Nd}_{0.7}\text{Sr}_{0.3}\text{MnO}_\delta$  Dünnschichten wurde von einem Magnetowiderstandsverhältnis bis zu  $\eta = 10^6\%$  berichtet [Xiong et al. 1995].

Bald nachdem der CMR entdeckt wurde, wurden auch verschiedene Phasendiagramme in Abhängigkeit von Temperatur und Magnetfeld oder Dotierung erstellt (s. z.B. [Tokura et al. 1996, Salamon & Jaime 2001, Dagotto et al. 2001]). Außerdem wurde der Metall-Isolator-Übergang unter Druck auch für  $\text{LaMnO}_3$  studiert

---

[Loa et al. 2001]. Eine Ladungs- und Orbital-Ordnungs-Phase wurde in vielen Perowskit-Manganaten gefunden, und seine Abhängigkeit von der Bandbreite und der Unordnung wurde analysiert [Tomioka & Tokura 2004, Mathieu et al. 2006]. In der paramagnetischen, isolierenden Hochtemperaturphase der dotierten Manganate zeigen optische Experimente ungewöhnliche dynamische Eigenschaften mit einem sehr geringen spektralen Gewicht in der Nähe der Fermi-Energie [Bocquet et al. 1992, Chainani et al. 1993, Saitoh et al. 1997, Park et al. 1996]. Ähnlich ist die optische Leitfähigkeit  $\sigma(\omega)$  sehr niedrig bis zu einer Energie von ca. 1 eV [Okimoto et al. 1995, Quijada et al. 1998, Jung et al. 1998, Takenaka et al. 1999]. Auf der anderen Seite ist die ferromagnetische, metallische Tieftemperaturphase ein schlechtes Metall wie z.B. die optische Leitfähigkeit zeigt [Okimoto et al. 1995].

Das physikalische Verständnis dieser Eigenschaften ist schwierig, wegen der Komplexität aufgrund des Zusammenspiels von Ladungs-, Spin-, Orbital- und Gitterfreiheitsgraden, die sich im Phasendiagramm widerspiegelt.

Der Ferromagnetismus der dotierten Manganate wurde erstmals von Zener mit dem "Doppelaustausch-Mechanismus" (DE) erklärt [Zener 1951a, Zener 1951b]. Ein quantenmechanisches Modell (Kondo-Gitter-Modell) für diesen Mechanismus auf einem Gitter [Kubo & Ohata 1972] wurde danach hergeleitet. Das Modell beschreibt die Hundsche Austauschwechselwirkung zwischen  $t_{2g}$ -Spins als klassische Vektoren und den  $e_g$ -Elektronen. Um die kinetische Energie der itineranten Elektronen zu optimieren, führt dieses Modell zu einem polarisierten Spinzustand.

Damit erklärt der Doppelaustausch-Mechanismus die höhere elektrische Leitfähigkeit in der ferromagnetischen Phase, aber es gibt wichtige Unterschiede zu den Experimenten, wie z.B. der temperaturabhängige Verlauf des Widerstands, der ein isolierendes Verhalten in der paramagnetischen Phase zeigt. Daher wurde die Wichtigkeit der Jahn-Teller-Kopplung zur Beschreibung dotierter Manganate vorgeschlagen [Millis et al. 1995] und zusammen mit den Doppelaustausch-Mechanismus studiert [Millis et al. 1996a, Röder et al. 1996]. Obgleich das neue Modell den CMR-Effekt nicht erklären kann, führt es für eine starke Jahn-Teller-Kopplung zu einer isolierende Phase mit Gitter-Polaronen.

Um den CMR und die paramagnetische, isolierende Phase zu erklären, wurden verschiedene Theorien entwickelt, insbesondere die Theorie der orbitale Polaronen [Kilian & Khaliullin 1998, Horsch et al. 1999], die Anderson-Lokalisation der  $e_g$ -Ladungsträger [Varma 1996], die Phasenseparation [Yunoki et al. 1998, Mayr et al. 2001], und ein phänomenologisches Zweiband-Modell [Ramakrishnan et al. 2004]. Der Einfluss der Coulomb-Wechselwirkung wurde auch im Rahmen des Kondo-Gitter-Modell

diskutiert [Held & Vollhardt 2000]. Durch die Coulomb-Wechselwirkung wird die Lokalisation der  $e_g$ -Elektronen erhöhen.

Trotz all dieser Bemühungen erklärt keine quantitative, mikroskopische Berechnung bislang zufriedenstellend alle experimentellen Ergebnisse, insbesondere nicht die paramagnetische, isolierende Phase. Noch steht es zur Debatte, ob die Jahn-Teller-Verzerrung oder die Coulomb-Wechselwirkung für die isolierenden Eigenschaften von  $\text{LaMnO}_3$  verantwortlich ist [Loa et al. 2001].

Die sehr aufwendigen numerischen Berechnungen sind ein weiteres Hindernis zu einem besseren Verständnis der Manganate. Sowohl die Coulomb-Wechselwirkung als auch die Jahn-Teller-Kopplung sowie die Hund'sche Kopplung zwischen den  $e_g$ -Elektronen und den lokalisierten  $t_{2g}$ -Spins müssen in Betracht gezogen werden. Dafür ist die dynamische Molekularfeld-Theorie (DMFT) (mit Quanten-Monte-Carlo-Simulation zur Lösung des Störstellenproblems) zur Zeit eine der zuverlässigsten Methode [Georges et al. 1996]. Die lokale Dichteanäherung (LDA) der Dichtefunktionaltheorie (DFT) kann dabei für eine systematische Untersuchung der elektronischen Strukturen mit der DMFT kombiniert werden (s. z.B. [Held2003]).

In dieser Arbeit studieren wir zuerst den druckinduzierten Isolator-Metall-Übergang mit der LDA+DMFT Methode, um die Rolle der Coulomb-Wechselwirkung und der Jahn-Teller-Kopplung in  $\text{LaMnO}_3$  zu verstehen. Dann wird ein realistischer, mikroskopischer Hamilton-Operator vorgeschlagen, um die paramagnetische, isolierende Hochtemperaturphase und den Übergang zur ferromagnetischen, metallischen Tieftemperaturphase in dotierten Manganaten zu erklären.

Die Arbeit gliedert sich dabei wie folgt: In Kapitel 2 rekapitulierten wir zuerst einige bekannte Modelle mit Doppelaustausch, Jahn-Teller-Kopplung, bzw. Coulomb-Wechselwirkung. Darauf aufbauend können wir das realistische, mikroskopische Modell konstruieren, das in unserer Arbeit benutzt wird. Wir diskutieren auch, wie die Parameter (z.B. die Hüpfermatrixelemente und die Coulomb-Wechselwirkung sowie die Phononfrequenz) abgeschätzt werden.

In Kapitel 3 stellen wir die DMFT (QMC) Methode vor und zeigen durch Beispiele, wie diese für fermionische und bosonische Systeme eingeführt werden kann. Wir präsentieren auch die LDA und LDA+DMFT Methoden. Die Formeln für die Suszeptibilität und die optische Leitfähigkeit werden abgeleitet.

In Kapitel 4 beschreiben wir im Detail das Hochdruckexperiment und diskutieren die LDA+DMFT Ergebnisse für den druckinduzierten Isolator-Metall-Übergang in  $\text{LaMnO}_3$ . Eine DMFT Berechnung für den realistischen, mikroskopischen Hamilton-

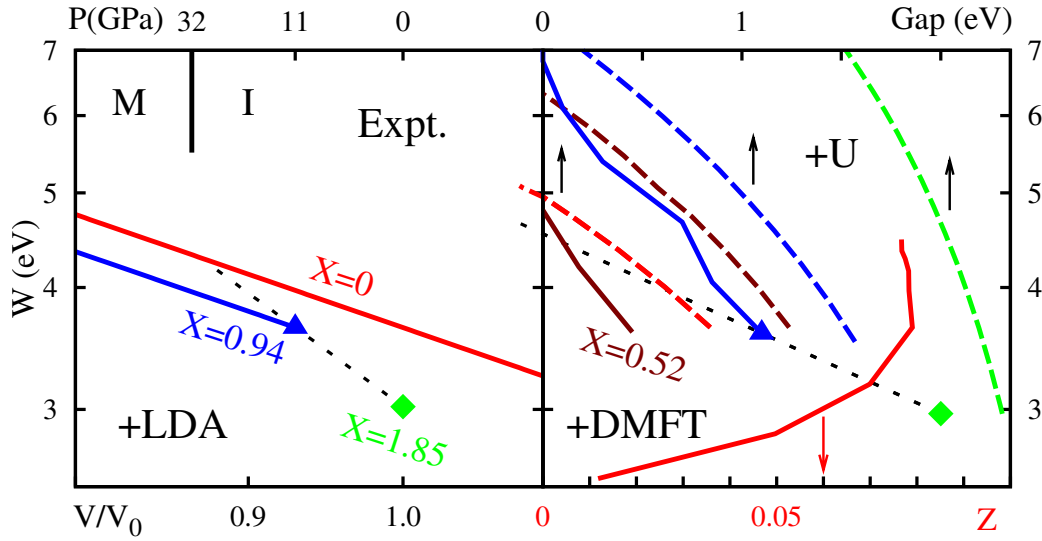


Figure D.1: **Links:** LDA  $e_g$ -Bandbreite,  $W \sim 6t$ , als Funktionen der Kompression,  $V/V_0$ . Die obere Abszisse zeigt den experimentellen Druck. Bei 32 GPa liegt der druckinduzierte Isolator-Metall-Übergang im Experiment [Loa et al. 2001]. Der dimensionslose Parameter  $X$  ist die LDA Kristallfeldaufspaltung in den Maßeinheiten von  $t$ . **Rechts:** LDA+DMFT (durchgezogene Linien) und LDA+U (gestrichelte Linien) Ergebnisse als Funktionen der Bandbreite  $W$ . Für den Isolator zeigen wir die Energie-Lücke (obere Skala) und für das Metall das Quasiteilchen-Gewicht (untere Skala). Volle Symbole sind Rechnungen für die experimentellen Gitter-Strukturen und schwarz-punktierte Linien sind Extrapolationen. Jede Kurve wurde mit festgelegter Struktur (Bandform) berechnet: orthorhombische 0 GPa (grün,  $X=1.85$ ), orthorhombische 11 GPa (blau,  $X=0.94$ ), kubische mit artifizieller Kristallfeldaufspaltung (dunkelrot,  $X=0.52$ ) und kubisch (rot,  $X=0$ ).

operator wird ebenfalls durchgeführt, um die elektronischen Eigenschaften und den strukturellen Übergang von einer dynamischen zu einer statischen Jahn-Teller-Verzerrung in  $\text{LaMnO}_3$  zu erforschen.

Wir finden, dass die LDA+DMFT Berechnungen ohne die Jahn-Teller-Verzerrung oder die Coulomb-Wechselwirkung keine metallische Phase unter normalen Bedingungen zeigen (s. Abbildung D.1). Wir stellen folglich fest, dass beide Wechselwirkungen notwendig sind, um Manganate zu beschreiben. Die lokalen  $e_g$ -Orbitale werden infolge des Jahn-Teller-Effektes aufgespalten. Die Aufspaltung wird durch die Coulomb-Wechselwirkung erhöht. Nur die Kombination von beiden führt zu einem isolierenden Grundzustand in  $\text{LaMnO}_3$  (s. Abbildung D.2). Durch den äußeren Druck wird die Gitterverzerrung reduziert und die Bandbreite der  $e_g$ -Elektronen immer größer. Schließlich ist die Aufspaltung so klein, dass es kein Gap mehr gibt und der Isolator-Metall-Übergang tritt auf. Aber am Übergang ist die

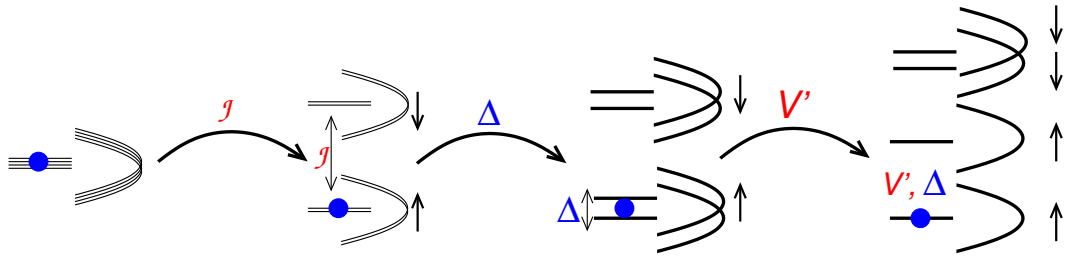


Figure D.2: Grafische Darstellung für die isolierende Natur von  $\text{LaMnO}_3$  aufgrund der Hundschen Kopplung  $\mathcal{J}$ , der Coulomb-Abstoßung  $V'$  und der Jahn-Teller-Verzerrung mit Kristallfeldaufspaltung  $\Delta$ .

Gitterverzerrung noch da. Daher ist der druckinduzierte Isolator-Metall-Übergang nicht vom Mott-Hubbard-Typ.

In Kapitel 5 werden für dotierte Manganate die DMFT Berechnungen für das realistische, mikroskopische Modell durchgeführt. Zuerst analysieren wir im Detail die verschiedenen optischen Experimente. Dann werden die numerischen Resultate dargestellt und die grundlegende Physik der Manganate diskutiert. Die spektrale Dichte der  $e_g$ -Elektronen in der Nähe der Fermi-Energie ist eine Kombination der verzerrten, besetzten Zustände und der unverzerrten, unbesetzten Zustände (s. Abbildung D.3). Diese beide Zustände entsprechen den Polaron-Zuständen und den sogenannten Midgap-Zuständen. Bei mittlerer Jahn-Teller-Kopplung finden wir eine Pseudolücke in der paramagnetischen Phase. Dies erklärt das anomale Verhalten der optischen Leitfähigkeit bei niedrigen Energien. Unterhalb der Curie-Temperatur ist das System aufgrund der ferromagnetischen Ordnung der Mangan-Spins metallisch. Aber es ist noch ein "schlechtes" Metall wegen der starken Orbital- und Gitterstörung. Bei einigen Dotierungen zeigt das System einen Isolator-Metall-Übergang am magnetischen Übergang. Wird dieser Übergang durch Erhöhung des Magnetfeldes induziert, so führt dies zum CMR.

Eine kurze Zusammenfassung unserer Arbeit wird in Kapitel 6 gegeben. Einige Unterschiede zu den Experimenten werden auch für weitere Untersuchungen diskutiert.

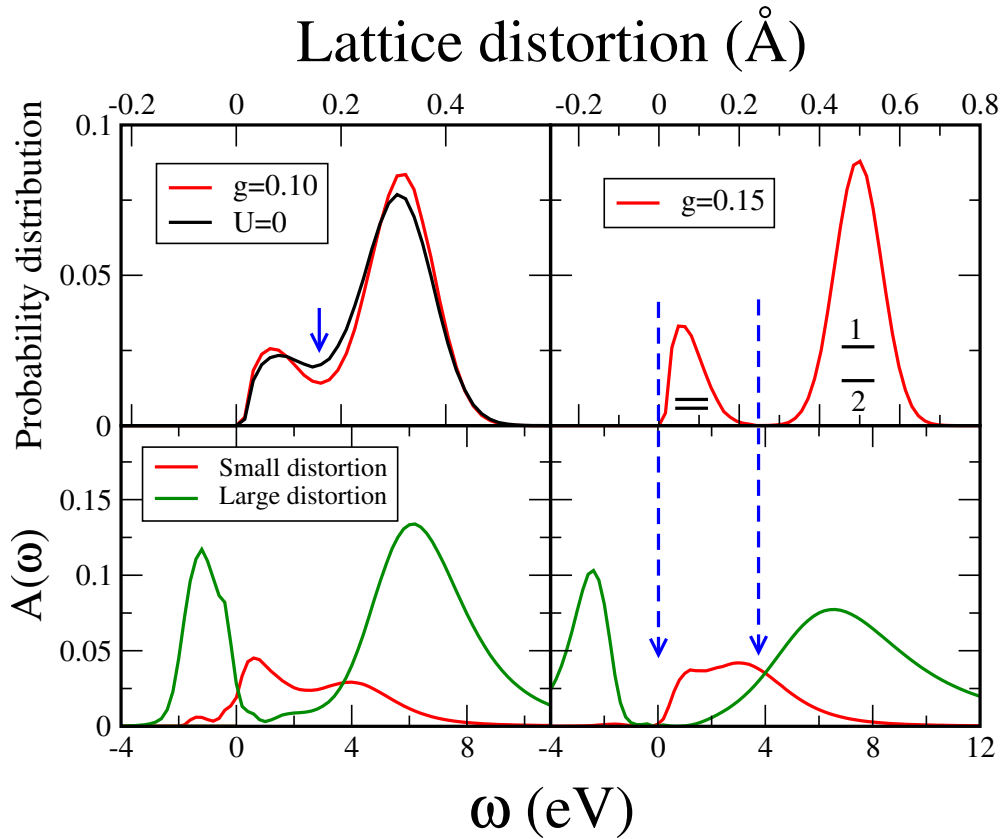


Figure D.3: Wahrscheinlichkeitsverteilung der Jahn-Teller-Verzerrungen und der entsprechenden Spektraldichten der  $e_g$ -Elektronen für die Jahn-Teller-Kopplung  $g = 0.10$  (linkes) und  $0.15$  (rechtes) bei  $\beta = 16$ . Die Spektraldichten der  $e_g$ -Elektronen werden in zwei Teile mit großer bzw. kleiner Gitterverzerrung getrennt. Zum Vergleich wird die Wahrscheinlichkeitsverteilung ohne die Coulomb-Wechselwirkung auch für  $g = 0.10$  gezeigt (schwarze gestrichelte Linien). Die Coulomb-Wechselwirkung erhöht den Polaron-Effekt.

## Curriculum Vitae

Name	Yi-feng Yang
Nationality	Chinese
Date of birth	5 February 1981
Place of birth	Henan, China

### Education

since 09/2003	Ph.D. studies Max-Planck-Institut für Festkörperforschung, Stuttgart <i>Dynamical mean field theory for manganites &amp; Kondo effect in quantum dots</i> with Prof. Dr. Walter Metzner and Dr. Karsten Held
06/2003	M.S. in Theoretical Physics Peking University, China
09/2001 – 06/2003	Postgraduate studies of Theoretical Physics Peking University, China <i>Electron transport through quantum dot coupled to Luttinger liquid leads</i> with Prof. Tsung-han Lin
07/2001	B.S. in Physics Peking University, China
09/1997 – 07/2001	Studies of Physics Peking University, China